A Measurement of the Λ_b Lifetime using Semileptonic Decays and Observation of the New State X(3872)

Kai Yi

A dissertation submitted to the Johns Hopkins University in conformity with the requirements for the degree of Doctor of Philosophy.

Baltimore, Maryland

2003

© Kai Yi, 2003

All rights reserved.

Abstract

A preliminary study is presented of the semileptonic decay $\Lambda_b \to \Lambda_c \ell \nu$ by searching for Λ_c–lepton pairs using the Run II ℓ+SVT(displaced track) sample collected by the CDF detector from Jan. 2002 to Jan. 2003. A total of 586 ± 46 Λ_c–lepton pairs are found. A parameterization method is used to correct for the SVT trigger bias and to understand the systematic uncertainty introduced by SVT in the lifetime measurement. Using an unbinned maximum-likelihood fit to the proper decay length distribution of 345 $\mu + \Lambda_c$ pairs , a preliminary Λ_b lifetime of $399 \pm 38(stat) \pm 21(sys)$ μm was obtained. The result is consistent with the Run I measurement of $c\tau_{\Lambda_b} = 396 \pm 46(stat) \pm 21(sys)$ μm.

Recently, the Belle Collaboration announced the observation of a new narrow state in exclusive B decays. They reported that the new state has a mass of 3872.0 ± 0.6(stat) $\pm$ 0.5(syst) MeV/c^2 and was observed via its decay to $\psi\pi^+\pi^-$. This state was immediately searched for and observed in the existing CDF data sample. CDF result uses inclusive production in $p\bar{p}$ collision of this state instead of any exclusive channel. The CDF mass measurement of this new state has comparable errors to Belle. The mass is measured as $3871.3 \pm 0.7 \pm 0.4 MeV/c^2$ at CDF.

Advisor: Professor Barry Blumenfeld

To all my advisors

Acknowledgements

First of all, I would like to thank my advisors at Hopkins–Prof. Barry Blumenfeld and Prof. Bruce Barnett. It is Barry who got me interested in fundamental physics research - Higgs particle search and neutrino oscillations. My curiosity about the Higgs and neutrinos has not yet been satisfied and keeps me motivated. I can not forget those days when you faced and answered my naive and "profound" questions both at Hopkins and Fermilab. I hope you enjoyed those moments. I also want to thank Barry for your letting me to do various adventures here and gave me a lot of flexible opportunities for the researches. Especially, you helped me to make the right decision at the right time. I want to thank Bruce for his first two year's advice to me. Especially, I want to thank you for giving me that chance to satisfy my wild interests in computer science. I still have a wonderful memory for the experiences in networks, graphics, algorithms,... I also want to thank you for your precious and wise advice on life. I want to thank Prof. Petar Maksimovic who got me interested in B physics. We had a lot of fun with the z vertex performance studies and topological vertex adventures and those experiences definitely helped my later researches. I want to thank Prof. Morris Swartz, Prof. Chih-Yung Chien and other faculties in the physics and astronomy department for being part of my education at Hopkins. Prof. Leon Madansky was so kind and was so eager to teach the HEP students all his knowledge and experience, I really appreciate that. I want to thank my Hopkins colleagues at Fermilab–Chadd Smith, Stephan Van Den Brink, Matt Herndon, Satyajit Behari, Yi Le, Robert Napora, Mat Martin and Reid Mumford.

A Chinese philosopher said: "You can find a advisor from three people accompany you". This is true at Fermilab, and I actually found many advisors here. Among those advisors at Fermilab, most of all, I want to thank MIT scientist Gerry Bauer and Fermilab scientist Ting Miao. Not only did Gerry give me a lot of advice and help in my research at CDF, but he also spent a lot of time in helping me improve my presentation skills and discussing "profound" physics questions. I appreciate all that help from Gerry. It is Ting Miao that helped me to choose Λ_b as my thesis topic. As a Λ_b expert, he gave me a lot of advice in that analysis and taught me

many experimental skills. I want to thank LBNL Professor Marjorie Shapiro for her guidance for the analysises as B-group convenor and encouragement to me as a senior scientist. I want to thank ANL scientist Barry Wicklund for his advice and help. I thank Mary Bishai for her advices and help for Λ_b analysis. I thank Jeff Tseng for sharing his Run I experience and useful discussion. I thank Ray Culbertson for his work on silicon alignment and many useful discussion. I want to thank Rick Snider, Joe Boudreau, Matthew Herndon for their help on track code in my initial adventure at CDF. As a CDF graduate student, I collaborated and learned many from other CDF colleagues–like Weiming Yao, Matthew Jones, Steve Worm, Jason Nielsen..., I can not mention all the names, but I do appreciate all those helps. I also thank the CDF B group convenors–Marjorie Shapiro, Kevin Pitts, Christoph Paus for their guidance and encouragement to me for the Λ_b lifetime measurement and the trust to me to ask me to check the observation of X(3872) at CDF.

I want to thank all those people who made the Tevetron and CDF detector available. I still remember those wonderful and exciting moments when I first found the Λ_b signal from about 10 pb^{-1} initial Run II data, when I first saw the significantly improved Λ_b signal by using Time-of-Flight for particle identification, when I first saw the X(3872) signal at CDF,... Without the effort of the accelerator division and CDF collaboration to make the Tevatron and CDF available, how can I experience those beautiful moments! I appreciate all your effort!

Finally, I want to thank my wife-Liqun for her patience to me as a physics graduate student, for those weekend days when you accompanied me to sit in front of a computer terminal!

Contents

List of Figures **viii**

List of Tables **xiv**

1 Introduction **1**
1.1 Standard Model Introduction 1
1.1.1 Fundamental Particles 2
1.1.2 Fundamental Interactions 4
1.2 $b\,\bar{b}$ Production at the Tevatron 6
1.3 b Quark Fragmentation and b Fractions 8
1.4 b Hadron Decay 13
1.4.1 The Spectator Model of b Hadron Decay 15
1.4.2 The Heavy Quark Effective Theory 17
1.4.3 Λ_b lifetime status and motivation for the measurement 18

Bibliography **20**

2 The CDF Detector at the Tevatron **23**
2.1 The Fermilab Tevatron 23
2.2 The Collider Detector at Fermilab 25
2.2.1 Cherenkov Luminosity Counter 27
2.2.2 Tracking System 27
2.2.3 Calorimetry 33
2.2.4 Muon Chambers 35
2.2.5 TOF Detector 39
2.3 Trigger 40

Bibliography **44**

3 Particle Identification **45**
3.1 Electron Identification 45
3.1.1 Longitudinal and Transverse Shower Sharing 45

3.1.2 Shower Shape 47
3.1.3 Track-cluster Matching 49
3.1.4 Electron removal of γ conversions 50
3.1.5 Fiducial Requirement and Trigger Confirmation 52
3.2 Muon Identification 53
3.2.1 Track-Muon chamber matching 53
3.3 Proton Identification 54
3.3.1 dE/dx 54
3.3.2 TOF 57
3.3.3 Combined dE/dx and TOF Performance 65

Bibliography **71**

4 Event Reconstruction for Λ_b **72**
4.1 Data Sample and code version 73
4.2 Track Reconstruction 73
4.3 Beam Position and Alignment 75
4.4 Vertexing 76
4.5 Background for $\Lambda_b \to \ell^+\Lambda_c^-\nu$ 77
4.6 $\Lambda_b \to \Lambda_c^+\ell^-\nu$ Signal 79
4.7 Λ_b Signal from 8 GeV sample 86

Bibliography **91**

5 Measurement of Λ_b Lifetime **93**
5.1 Λ_b Vertex and Decay length 93
5.2 Lifetime bias from displaced track(SVT) 94
5.3 Lifetime Fitting 99
5.4 Systematic Uncertainties Check 109
5.5 Preliminary Results and Discussion 119

Bibliography **121**

6 Observation of the New State X(3872) at CDF **123**
6.1 Introduction 123
6.2 Event Reconstruction 124
6.3 Mass distribution 127
6.4 Conclusion 134

Bibliography **135**

List of Figures

1.1 Leading order b production Feynman diagrams. 6
1.2 Higher order b production Feynman diagrams. 7
1.3 Differential b production cross section versus p_T at CDF II 9
1.4 A schematic of the fragmentation process. 10
1.5 b hadronic decay (a) and b semileptonic decay (b) 13
1.6 Λ_b semileptonic decay. 14
1.7 An example of Λ_b hadronic decay. 14
1.8 A B meson decay in the spectator model, there is no effect from the accompanying antiquark, so all b hadrons have the same lifetime. . . 15

2.1 A schematic diagram of the Tevatron. 24
2.2 A view of the CDF II detector 26
2.3 The CDF II CLC detector 28
2.4 End view (top) and side view (bottom) of the CDF II silicon system 30
2.5 Side view of the central region of the CDF(quarter section) 32
2.6 A schematic view of the CDF II calorimeter system. 35
2.7 A 15° calorimeter wedge. 36
2.8 A schematic view of CES. 37
2.9 Muon system coverage in $\eta - \phi$ space. 37
2.10 A wedge of CMU. 38
2.11 The run-II trigger-system block diagram. 41

3.1 The Hadem distribution for electrons, the red (or gray in black-white) line is the distribution for default electron candidates, the blue curve is the distribution for electrons which passed the LeptonSvtSel model [2], and the black one is the distribution of sideband subtracted electron candidate for electron+D^0 sample. 46

3.2 The Lshr distribution for electrons, the red (or gray in black-white) line is the distribution for default electron candidates, the blue curve is the distribution foe electrons which passed the LeptonSvtSel model [2], and the black one is the distribution of sideband subtracted electron candidate for electron+D^0 sample. 48
3.3 CES matching χ^2 in x and z direction distribution. For electrons, the red (or gray in black-white) line is the distribution for default electron candidates, the blue curve is the distribution for electrons which passed the LeptonSvtSel model [2], and the black one is the distribution of sideband subtracted electron candidate for electron+D^0 sample. . . 49
3.4 CES position difference in x and z direction (Δ_x and Δ_z) distribution. For electrons, the red (or gray in black-white) line is the distribution for default electron candidates, the blue curve is the distribution for electrons which passed the LeptonSvtSel model [2], and the black one is the distribution of sideband subtracted electron candidate for electron+D^0 sample. 50
3.5 E/p distribution for electron in electron+SVT sample. 51
3.6 Sep_{xy} distribution of conversion electrons for the momentum range 1.0 to 2.0 GeV. The black histogram is for all default cuts; the blue (or gray in black-white) one is the same distribution after sideband subtraction in $\Delta cot\theta$. 52
3.7 $\Delta cot\theta$ distribution of the conversion electrons for the momentum range 1.0 to 2.0 GeV. 53
3.8 dE/dx separation power from PDG [7]. 56
3.9 Ideal dE/dx separation power at CDF. 56
3.10 The $p\pi$ and $\pi\pi$ mass distribution. 58
3.11 The $p\pi$ mass distribution and the average dE/dx for corresponding mass bin. 59
3.12 Top: the difference between proton dE/dx and predicted proton dE/dx in the Λ sample. Bottom: the difference between proton dE/dx and predicted proton dE/dx in the K_s sample. 60
3.13 The dE/dx pull distribution after the modification for proton(top) and pion(bottom). 61
3.14 TOF separation power 62
3.15 TOF pull distribution for proton(top) and pion(bottom). 63

3.16 $p\pi$ invariant mass and likelihood ratio distribution. The left top is the $p\pi$ invariant mass distribution of candidates used to demonstrate the proton likelihood ratio distribution. From the right top to the right bottom are the real proton(in the Λ mass window of [1.112,1.12], sideband subtracted) and fake proton(sideband in the Λ mass window of [x,y]) likelihood ratio distribution in the cases of TOF/dE/dx both being used,only TOF being used,only dE/dx being used to calculate the probability, respectively. 64
3.17 Top left: Λ mass distribution without proton identification. Top right: K_s reflection by assign pion mass to the proton inside the Λ mass window without proton identification. Bottom left: Λ mass distribution with proton identification (TOF only). Bottom right: K_s reflection by assigning pion mass to the proton inside the Λ mass window with proton identification. 66
3.18 Top left: Λ mass distribution without proton identification. Top right: K_s reflection by assign pion mass to the proton inside the Λ mass window without proton identification. Bottom left: Λ mass distribution with proton identification (dE/dx only). Bottom right: K_s reflection by assign pion mass to the proton inside the Λ mass window with proton identification. 67
3.19 Top left: Λ mass distribution without proton identification. Top right: K_s reflection by assign pion mass to the proton mass inside Λ mass window without proton identification. Bottom left: Λ mass distribution with proton identification (TOF+dE/dx). Bottom right: K_s reflection by assign pion mass to the proton inside the Λ mass window with proton identification. 68
3.20 Proton identification efficiency as a function of proton p_T. Top: TOF and dE/dx are both used for proton identification, bottom: only dE/dx is used for proton identification. 69
3.21 $pK\pi$ invariant mass from Λ_b without(top) proton identification and with(bottom) proton identification. 70

4.1 The five helix parameters describe a track. 76
4.2 A $pK\pi$ mass distribution in μ+SVT sample, where we keep other cuts unchanged and require $\chi^2_{r\phi}$ be great than 9. No signal can be seen. . 81
4.3 Λ_b Lxy resolution distribution. 82
4.4 Λ_c Lxy with respect to primary vertex resolution distribution. 83
4.5 $pK\pi$ invariant mass for right sign events in lepton+SVT sample. The fit returns a yield of 586 ± 46 events. 84
4.6 $pK\pi$ invariant mass for right sign(solid line) and wrong sign(dashed line) events in lepton+SVT sample. No signal can be attributed to the wrong sign sample. 85

4.7 $pK\pi$ invariant mass in e+SVT sample where TOF and dE/dx are both required to identify the proton, proton likelihood ratio > 0.5. 86
4.8 $pK\pi$ invariant mass in e+SVT sample where only dE/dx is used to identify the proton, proton likelihood ratio > 0.5. 87
4.9 $pK\pi$ invariant mass in μ+SVT sample where TOF and dE/dx are both required to identify the proton, proton likelihood ratio > 0.5. 88
4.10 $pK\pi$ invariant mass in μ+SVT sample where only dE/dx is used to identify the proton, proton likelihood ratio > 0.5. 89
4.11 $pK\pi$ invariant mass for right sign(solid line) and wrong sign(dashed line) in inclusive 8 GeV muon sample.No signal can be attributed to the wrong sign sample. Proton likelihood ratio > 0.5 cut was applied and proton was required to have both TOF and dE/dx information. Yield returned was 68 ± 15. 90

5.1 Topological sketch of semileptonic decay $\Lambda_b \to \Lambda_c^+ \ell\nu$ where $\Lambda_c \to pK^-\pi^+$. 94
5.2 Correlation between Λ_b $c\tau$ and proton d_0. $c\tau$ is not uniform along proton d_0, therefore introducing a bias to the lifetime measurement. 95
5.3 SVT efficiency obtained from parameterization method, where the parameters are measured from a inclusive J/ψ sample. 96
5.4 Effect of lifetime resolution and SVT acceptance on $c\tau$ measurements. The function $f1(x)$ is the pure exponential $c\tau$ distribution, $f2(x)$ is the $c\tau$ distribution after SVT acceptance, and $f3(x)$ is the $c\tau$ distribution after SVT acceptance convoluted with a Gaussian detector resolution function. 97
5.5 Distribution of the K factor in μ+SVT sample, where $K = P_t(\Lambda_c\ell)/P_t(\Lambda_b)$, obtained from parameterization MC. 98
5.6 Comparison of proton transverse momentum distribution between data and full Monte Carlo for μ+SVT sample. The solid line is obtained from MC and the red (or gray for black and white) circles are obtained from data. 99
5.7 The μ transverse momentum comparison between data and full Monte Carlo for μ+SVT sample. The solid line is obtained from MC and the red (or gray for black and white) circles are obtained from data. . . 100
5.8 $\mu + \Lambda_c$ transverse momentum comparison between data and realistic Monte Carlo for μ+SVT sample. The solid line is obtained from MC and the red (or gray for black and white) circles are obtained from data. 101
5.9 Sideband $c\tau$ fitting result in μ+SVT sample. The solid line is the fitting result, the squares with uncertainty bars are data in sideband region. 102
5.10 Same as Fig 5.9, but on a log scale. 103

5.11 Signal region $c\tau$ fitting result in μ+SVT sample. The red (gray in black white) circles with uncertainty bars are data in signal region, the solid line is fit result in the signal region, the dashed line is the background contribution. 103
5.12 Same as Fig 5.11, log scale. 104
5.13 The $c\tau$ fit result in the μ+SVT sample. The red (gray in black white) circles with uncertainty bars are data in signal region, the solid line is fit result in the signal region. The blue dot line is the fitting result for sideband data. The black dash dot line is the extracted signal distribution. 104
5.14 The $c\tau$ fit result in the μ+SVT sample, same as Fig 5.13 but on a log scale. 105
5.15 The $c\tau$ sideband fit result in μ+SVT sample for the case of TOF and dE/dx both being required to identify proton. The blue squares with uncertainty bars are data in sideband region, the blue dot-dash line is the fitting result for sideband data. 106
5.16 Same as Fig 5.15 but on a log scale. 106
5.17 The $c\tau$ sideband fit result in the μ+SVT sample for the case of only dE/dx being required to identify proton. The blue squares with uncertainty bars are data in sideband region, the blue (gray in black white) line is the fit result for sideband data. 107
5.18 Same as Fig 5.17 but on a log scale. 107
5.19 The K factor distribution for inclusive 8 GeV lepton sample obtained from validated Monte Carlo, $K = P_t(\Lambda_c\ell)/P_t(\Lambda_b)$. 108
5.20 Signal region $c\tau$ fitting result in inclusive 8 GeV muon sample, both TOF and dE/dx are required to identify proton. The red (gray for black and white) circles with uncertainty bars are data in signal region, the solid line is fitting result in the signal region. 110
5.21 Same as Fig 5.20, log scale. 111
5.22 Sideband region $c\tau$ fit result in inclusive 8 GeV muon sample, both TOF and dE/dx are required to identify proton. The red (gray for black and white) circles with uncertainty bars are data in signal region, the solid line is fit result in the signal region. 111
5.23 Same as Fig 5.22, log scale. 112
5.24 $c\tau$ fit result in inclusive 8 GeV muon sample, both TOF and dE/dx are required to identify proton. The red circles with uncertainty bars are data in signal region, the solid line is fit result in the signal region. The blue squares with uncertainty bars are data in sideband region, the blue dot-dash line is the fit result for sideband data. The black dash line is the extracted signal distribution. 113
5.25 $c\tau$ fit result in inclusive 8 GeV muon sample, same as Fig 5.24 but in log scale. 114

5.26 Lifetime fit result vs input lifetime from full Monte Carlo check. There is a maxmimum 9 μm shift. 114
5.27 A fit to the full Monte Carlo lifetime, input lifetime 430um, fitting result: 426+/-3 115
5.28 A fit to the full Monte Carlo lifetime, log scale 115
5.29 A 2d correlation display between proton transverse momentum and $\ell + \Lambda_c$ transverse momentum. 117
5.30 The K factor, $K = P_t(\Lambda_c \ell)/P_t(\Lambda_b)$, distributions for different proton momentum regions, the mean value for the six different cases are 0.8666, 0.8681, 0.8662, 0.8668, 0.869, 0.8709 (from left top to right bottom) 117
5.31 Distribution of the K factor in μ+SVT sample, where $K = P_t(\Lambda_c \ell)/P_t(\Lambda_b)$, obtained from full MC sample, where K is weighted by proton identification efficiency. Red (gray in black white) point is weighted by proton identification efficiency which both TOF and dE/dx are used, and blue ball is weighted by proton identification efficiency which only dE/dx is used. 118
5.32 K factor for μ+SVT sample obtained in generator level mixing 30 % of Λ_c^* 120

6.1 The PDG table of the quark model. 125
6.2 Reconstructed $J/\psi \to \mu\mu$ mass distribution. 128
6.3 $J/\psi\pi\pi$ mass distribution without $\pi\pi$ mass cut. 129
6.4 $J/\psi\pi\pi$ mass distribution with $\pi\pi$ mass cut. 130
6.5 $J/\psi\pi\pi$ mass distribution for the tight independent check. 131
6.6 $J/\psi\pi\pi$ mass distribution for the loose independent check. 131
6.7 The $\pi\pi$ mass distribution from new X(3872) state after preliminary side band subtraction. 132
6.8 The $\pi\pi$ mass distribution from $\psi(2s)$ after preliminary side band subtraction. 133

List of Tables

1.1 lepton properties 2
1.2 quarks properties 3
1.3 bosons properties 5
1.4 Fractions of weakly decaying b hadron in $p\bar{p}$ collisions 12
1.5 bottom and charm hadrons lifetimes 16
1.6 bottom and charm hadrons lifetimes 18

5.1 Results of Λ_b lifetime fit from 345 $\mu + \Lambda_c$ events, where subscript 1 on background parameters represents only dE/dx was used for proton identification, the subscript 2 on background parameters represents both TOF and dE/dx were used for proton identification. The s factor is fixed to 1.42 which we extracted from inclusive μ sample. 105
5.2 Lifetime fit result in inclusive 8 GeV lepton sample 109
5.3 Λ_b background fit results of sideband events, where the subscript 1 on background parameters represents only dE/dx was used for proton identification,the subscript 2 on background parameters represents both TOF and dE/dx were used for proton identification. 113
5.4 Summary of systematic uncertainties 119
5.5 Comparison with LEP results obtained using Λ_c-lepton sample and CDF I result. 120

Chapter 1

Introduction

1.1 Standard Model Introduction

There has been a fundamental question from the beginning of human civilization: What is the world made of? Our ancestors tried various explanations, from fire, water, earth, and air proposed by Empedocles of Sicily [1] to the periodic table proposed by Mendeleev, and understanding matter more and more deeply. Today, to the best of our knowledge, two classes of fundamental particles–quarks and leptons make up our world. They are both fermions carrying spins of $\frac{1}{2}$. Details of the fundamental particles will be discussed in next section. Among these fermions, the bottom quark was discovered at Fermilab through the decay of its quark-antiquark bound state–$\Upsilon(1S)$ in 1977 [2]. The top quark was discovered at Fermilab in 1994 [3], and finally the tau neutrino was observed by DONUT group at Fermilab in 2000 [4].

Another fundamental question is how fermions interact. This is described by another family of particles—bosons carrying integer spins. Several fundamental bosons mediate the fundamental interactions we know so far — electromagnetism,weak, strong and gravity, and a special particle called Higgs which is believed to give mass to particles, this will be discussed later. Among these fundamental bosons, $W^{\pm}$ and Z were discovered at CERN in 1980's. [5], but the Higgs boson has not yet been observed.

In the 1970's, a model describing all the fundamental particles and interactions

except gravity was established and accepted by particle physicists, this model is called the standard model. This is a quantum field theory and derives all the fundamental interactions from local gauge invariance. In the standard model framework, electrodynamics and the Glashow-Weinberg-Salam theory describes the electromagnetic interaction as well as the electroweak interaction, and quantum chromodynamics describes the strong interactions. [6]

1.1.1 Fundamental Particles

By the standard model of particle physics, all matter is built from a small number of fundamental fermions —six leptons and six quarks.

The six leptons are classified into three generations as :

$$\begin{pmatrix} \boldsymbol{\nu_e} \\ \boldsymbol{e} \end{pmatrix}, \begin{pmatrix} \boldsymbol{\nu_\mu} \\ \boldsymbol{\mu} \end{pmatrix}, \begin{pmatrix} \boldsymbol{\nu_\tau} \\ \boldsymbol{\tau} \end{pmatrix}$$

The basic properties of the six leptons are summarized in Table 1.1 [7]. In the framework of the standard model, each particle has a partner, so we have a total of 12 leptons. Each lepton generation has a different *lepton flavor number* L_e, L_μ, L_τ, which equals +1 for each lepton and -1 for its antiparticle of the appropriate flavor. The lepton flavor number is conserved during decays. Recently there is some evidence to show that neutrinos have mass and that can lead to 'oscillations' of one type of neutrino flavor into another on long enough timescales [8].

Table 1.1: lepton properties

lepton	charge	mass(Mev/c^2)	lifetime(τ) or lifetime/mass(τ/m)
ν_e	0	< 3 eV	$\tau/m > 300\ s/eV$(90 % C.L.,reactor)
e	-1	0.511	$\tau > 4.6 \times 10^{26}$ yr (90 % C.L.)
ν_μ	0	< 0.19 MeV (90 % C.L.)	$\tau/m > 15.4\ s/eV$ (90 % C.L.)
μ	-1	105.66	2.197×10^{-6} s
ν_τ	0	< 18.2 MeV (95 % C.L.)	
τ	-1	$1776.99\ ^{+0.29}_{-0.26}$	$(290.6 \pm 1.1) \times 10^{-15}$ s

The six quarks are also classified into three generations as :

$$\begin{pmatrix} \boldsymbol{u} \\ \boldsymbol{d} \end{pmatrix}, \begin{pmatrix} \boldsymbol{c} \\ \boldsymbol{s} \end{pmatrix}, \begin{pmatrix} \boldsymbol{t} \\ \boldsymbol{b} \end{pmatrix}$$

where t(op), b(ottom), c(harm) quarks are referred to as heavy flavors, s(trange), d(own), u(p) quarks are referred to as light flavors.

Table 1.2: quarks properties

quarks	charge(e)	mass(Mev/c^2)
u	$\frac{2}{3}$	$1.5 \sim 4.5$
d	$-\frac{1}{3}$	$5 \sim 8.5$
c	$\frac{2}{3}$	$1000 \sim 1400$
s	$-\frac{1}{3}$	$80 \sim 155$
t	$\frac{2}{3}$	174300 ± 5100
b	$-\frac{1}{3}$	$4000 \sim 4500$

The basic properties of the six quarks are summarized in Table 1.2 [7]. Each quark also has a antiquark partner, so we have 12 quarks in total. u and d quarks are considered as doublet components $\pm\frac{1}{2}$ of an isospin vector of value $I = \frac{1}{2}$, while the other four quarks each has a quantum number — S for s quark, C for c quark, B for b quark, and T for t quark. These numbers are conserved in strong interactions, but they can change by 1 in weak decays. That quarks do not conserve generation number is due to the fact of the quark's mass eigenstates are not the same as its weak eigenstates. This property is characterized by a quark flavor mixing matrix— the CKM(Cabibbo-Kobayashi-Maskawa) matrix. By convention, the three charge -$\frac{1}{3}$ quarks are used to form the CKM matrix:

$$\begin{pmatrix} \boldsymbol{d'} \\ \boldsymbol{s'} \\ \boldsymbol{b'} \end{pmatrix} = \begin{pmatrix} \boldsymbol{V_{ud}} & \boldsymbol{V_{us}} & \boldsymbol{V_{ub}} \\ \boldsymbol{V_{cd}} & \boldsymbol{V_{cs}} & \boldsymbol{V_{cb}} \\ \boldsymbol{V_{td}} & \boldsymbol{V_{ts}} & \boldsymbol{V_{tb}} \end{pmatrix} \begin{pmatrix} \boldsymbol{d} \\ \boldsymbol{s} \\ \boldsymbol{b} \end{pmatrix}$$

where the q' and q represent the weak and mass eigenstates, respectively. This mixing allows heavier quarks to decay into lighter quarks of a different generation, *e.g.* $b \to cW^{*-}$, where W^{*-} is a virtual particle which subsequently decays to q$\bar{\text{q}}$' or $\ell^-\nu$. The $\ell^-\nu$ decay mode is specifically the channel this thesis is going to discuss. The CKM matrix is unitary and this means the matrix is completely described by

three parameters and one complex phase. Measuring these parameters, or the CKM matrix elements, is one of the most interesting topics in particle physics today.

In reality, leptons can exist as a free particle, but quarks can not. Quarks are confined inside "hadrons" which are bound states of quarks. Among hadrons, a bound state of a quark and an antiquark is called a meson and a bound state of three quarks is called a baryon. A proton (uud) and a neutron (udd) are combinations of the lightest u and d quarks. The basic materials of our universe are the electron and stable particles consisting of u and d quarks. The heavier quark combinations are not a part of normal life, but they can be observed in high energy collisions or cosmic rays. However, it would be very interesting both to theory and experiment if we can see a free quark. There are some experimental searches for free quarks, but no evidence has been found so far [9].

Besides the known mesons and baryons, there are some other possibilities for quark combinations—like four quark state, penta quark states, six quark states, quark-gluon hybrids, glue-ball [7]. The newly discovered X(3872) can be a four quark state, a quark-gluon hybrids candidate, or a $c\bar{c}$ charmonium [10]. This will be discussed more in chapter 6. Four experiments reported the evidence for a penta quark states recently [11]. There is some indication for a six quark state called double hypernucleus has been found, but this needs confirmation [12]. BES and CLEO have been searching for glue-ball and found some indications [13].

1.1.2 Fundamental Interactions

Currently we know that there are four fundamental interactions among the particles: electromagnetic, weak, strong and gravity. Gravity is the weakest and is not incorporated into the standard model. The standard model describes electromagnetism, weak, strong interaction by the "principle of gauge invariance", which stipulates that certain transformations of the fermi fields should not affect the physical predication of the theory. Mathematically, this requirement results in the appearance of gauge boson fields that corresponds to the carriers of electromagnetism, weak, strong interactions. The bosons introduced in this way are all necessarily massless.

The interaction carrier, or mediator, of electromagnetism is the photon, the interaction carriers of the weak interaction are the W and Z, and the interaction carrier of strong interaction are the gluons. Experimental evidence shows that the photon and the gluons are indeed massless, but W and Z are very massive— about one hundred times more massive than the proton. A fundamental aspect of the standard model is the way it solves this problem via the so-called "spontaneous symmetry breaking" or "Higgs" mechanism. It introduces another massive boson—the H(iggs) particle [14]. Properties of the four bosons are listed in Table 1.3 [7]. For completeness, gravitational interaction is supposedly carried by a spin 2 boson, the graviton. The Higgs predicted by the standard model has not yet been observed by experiment. The recent direct searches at LEP implies $m_H > 114.4 GeV$ at the 95% CL [15]. To search for evidence of the Higgs at the Tevatron and the LHC will be one of the most exciting topics in the coming years.

Table 1.3: bosons properties

bosons	charge(e)	mass(Gev/c^2)	spin
γ(EM)	0	0	1
$W^{\pm}$,Z^0(Weak)	$\pm$1,0	80,91	1
g(Strong)	0	0	1
H(Special)	0	>114.4, 95% CL	0

Among the four interactions, the relative strengths among strong, electromagnetism, weak, and gravity are 1:10^{-2}:10^{-7}:10^{-39}. The typical lifetimes for a decay through strong, electromagnetism and weak interaction are 10^{-23}:10^{-20}:10^{-10} seconds. The lifetime of a decay through the weak interaction can be easily measured experimentally, while the lifetime through the strong interaction can not be measured directly. However, it can be inferred from its measured width Γ by the Uncertainty Principle, $\Gamma\tau = \hbar$.

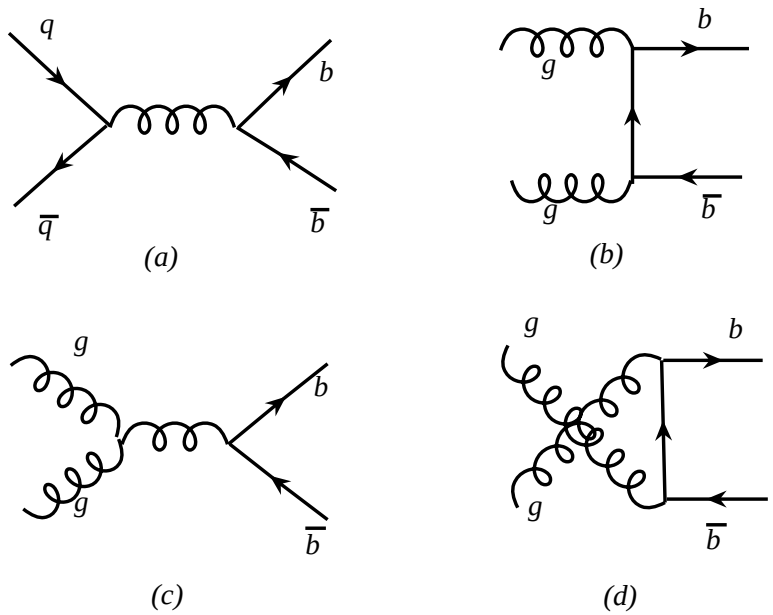

Figure 1.1: Leading order b production Feynman diagrams.

1.2 $b\ \bar{b}$ Production at the Tevatron

In $p\bar{p}$ collisions at $\sqrt{s}$=2.0 TeV at the Tevatron, there are plenty of partons—gluons and sea quarks around the valence quarks(u,u,d) of proton. The probability of finding a parton which carries a momentum fraction x of the proton defines the parton distribution function (PDF) $F_i(x, Q^2)$, where subscript "i" is the type of the parton and Q is the 4-momentum transferred in the collision or the invariant mass of the exchanged virtual boson. Deep inelastic scattering, Drell-Yan, jet and direct photon production measurements are used to construct the parton distribution functions. At CDF, the parton distribution function provided by the MRST group and the CTEQ group are commonly used [16].

At the Tevatron, b and $\bar{b}$ quarks are produced in the interactions of partons in

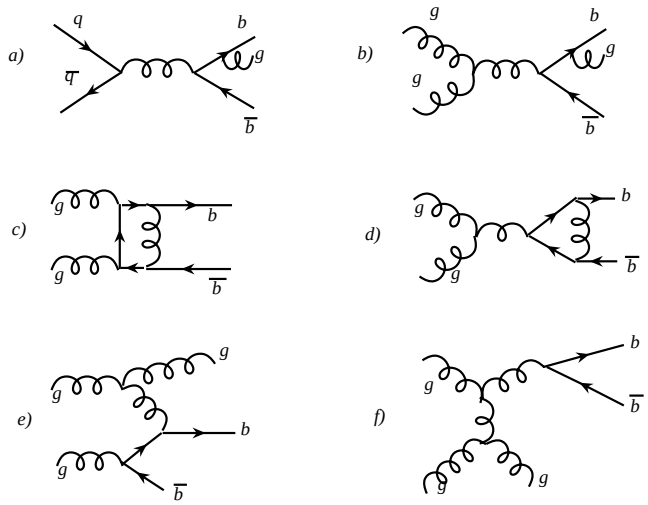

Figure 1.2: Higher order b production Feynman diagrams.

the initial proton and antiproton—this process is called b production. Later the produced b and $\bar{b}$ quarks combine with other quarks to form hadrons—this process is called b fragmentation. Generally, the production and fragmentation process are assumed to be independent and can be treated separately. Feynman diagrams of the leading order(LO) processes are shown in Figure 1.1, in which (a) is the quark-antiquark annihilation process, and the other three are gluon-gluon fusion processes. Valence quark-antiquark annihilation dominates when $2M_q/\sqrt{s} \geq 0.1$, however, this condition is satisfied only for top quark production at Tevatron. For b production, since $2M_q/\sqrt{s} \ll 1$(it is ~ 0.005 at Tevatron), the gluon-gluon fusion dominates, and higher order diagrams can give a larger contribution than the leading order diagrams. Several factors cause this effect: large gluon density, larger color factor at a 3-gluon vertex, and the cross section enhancement for diagrams containing t-channel vector exchange. Some of the higher order Feynman diagrams are shown in Figure 1.2, in which a) and b) are the gluon radiation process, c) and d) are the loop diagrams, e)

is the flavor excitation process, f) is the gluon splitting process. The flavor excitation process and the gluon splitting process are the dominant higher order diagrams [17]. The inclusive single quark cross section for the leading order and next-to-leading order have been calculated and the calculation leaves two free parameters which must be fixed: the renormalization mass scale—μ, which we take to be $\mu_0 = \sqrt{m_b^2 + p_T^2}$; and the b quark mass, which we take to be 4.75 GeV/c^2. The calculation of course also depends on the parton distribution function [18].

The b production cross section has been measured at CDF I through several B decay channels [19] and so far at CDF II through the inclusive J/ψ channel [20]. A preliminary result from Run II and a comparison to the theoretical prediction is shown in Figure 1.3.

The b and $\bar{b}$ produced via the leading order processes tend to be back-to-back in the transverse plane if the initial two partons are head-to-head and have roughly the same energy, while the b and $\bar{b}$ produced via the next leading order processes tend not to be back-to-back in the transverse plane because a third parton is involved. In the case of gluon splitting, they tend to be closer if the initial gluon momentum is high. In the semileptonic decay of b hadrons, the lepton from one b has a chance to be mistaken as coming from the other b and gives a background to signal. This will be discussed in chapter 4.

1.3 b Quark Fragmentation and b Fractions

A b quark carries some momentum when it is produced at the Tevatron and it releases its energy by the "fragmentation" or so-called "hadronization process". As discussed in previous section, the production and fragmentation process are assumed to be independent. The fragmentation is understood at a phenomenological level. The b quark carries color charge, and at production the color charge stretches the gluon field. It can create real quark-antiquark pairs when the energy density reaches a high enough level. During this process, some quarks can form a colorless hadron (mesons or baryons) and other quarks continue to stretch the gluon field and pull out quark-antiquark pairs until all the initial energy is consumed into producing colorless

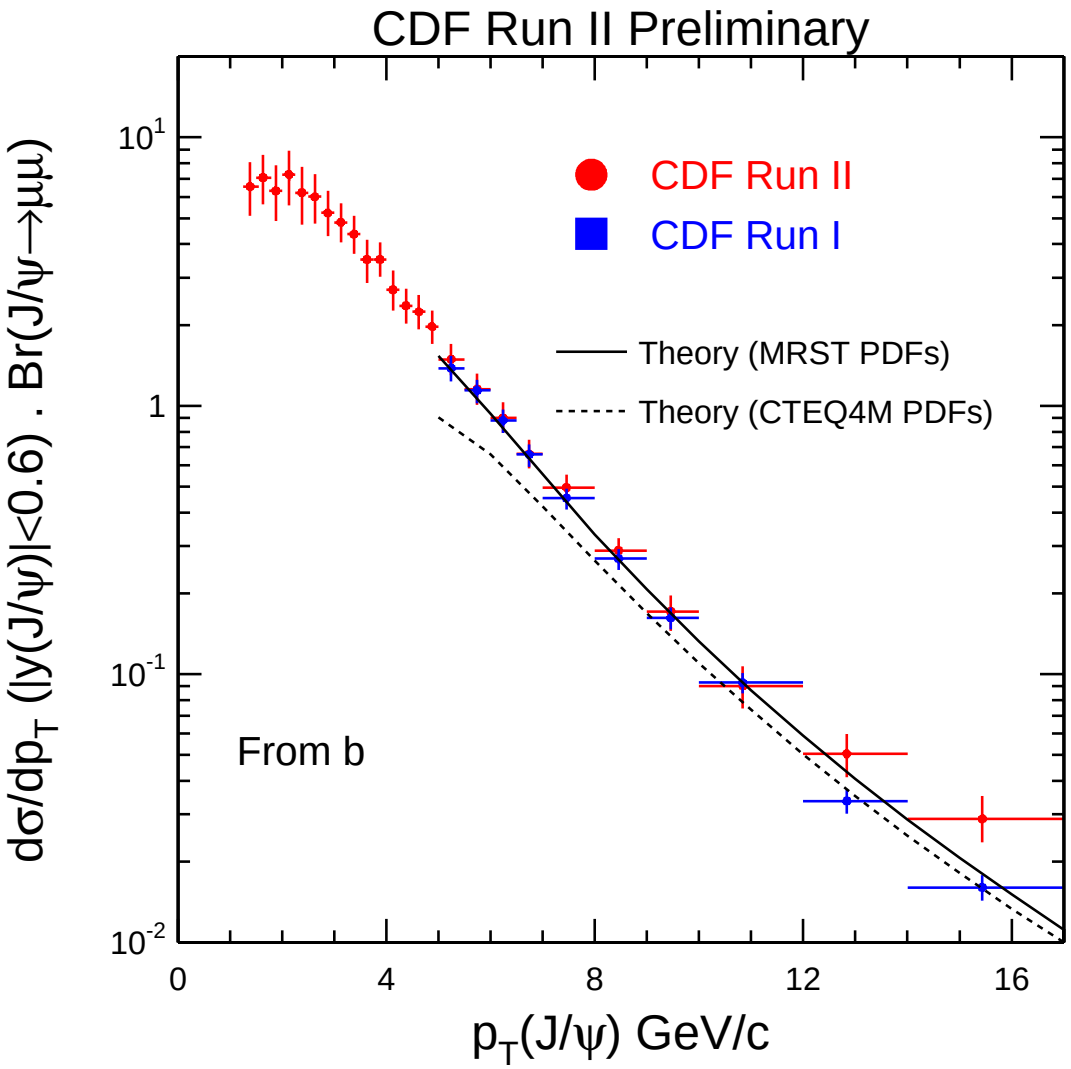

Figure 1.3: Differential b production cross section versus p_T at CDF II

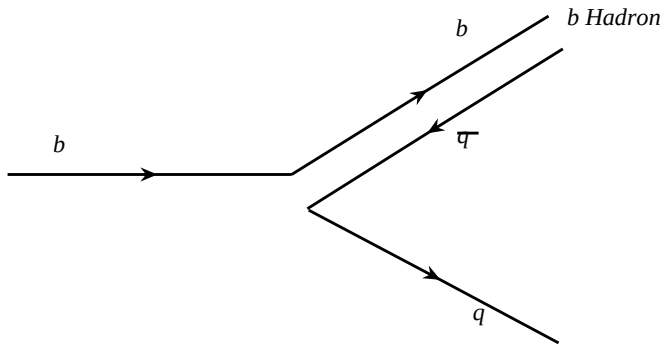

Figure 1.4: A schematic of the fragmentation process.

hadrons. A schematic picture of fragmentation is shown in Figure 1.4. Quantitatively, fragmentation is described in terms of functions $D_q^h(z)$ of a single variable z which is defined as the ratio of the energy and longitudinal momentum of the hadron $Q\bar{q}$ to the sum of the energy and momentum of the heavy quark Q:

$$z = \frac{(E + p_{||})_{Q\bar{q}}}{(E + p)_Q} \tag{1.1}$$

$D_q^h(z)$ is the probability of a heavy quark Q to form a hadron with an antiquark $\bar{q}$(or diquark qq) as a function of z, and z is relativistically invariant with respect to boosts along the initial quark direction.

For light quarks, the meson fragmentation function $D_q^h(z)$ is proportional to $z^{-1}(1-z)^2$, but this is different for heavy quarks because of their heavy mass. A heavy quark only loses a small amount of its energy when it combines with a antiquark or diquark. Peterson et al. proposed a simple parameterization for the fragmentation function [21]. In the Peterson model, the transition amplitude is inversely propor-

tional to the energy transfer :

$$\Delta E = E_H + E_q - E_Q \tag{1.2}$$

where E_H, E_q, E_Q are the energies of the new hadron, the new quark and the initial heavy quark, respectively. For simplicity, assume $m_H \simeq m_Q$ and expand the energy transfer about the transverse particle mass, and then ΔE has the following format:

$$\Delta E = \sqrt{m_Q^2 + z^2 p^2} + \sqrt{m_q^2 + (1-z)^2 p^2} - \sqrt{m_Q^2 + p^2} \tag{1.3}$$

$$\propto 1 - 1/z - \epsilon_Q/(1-z) \tag{1.4}$$

where ϵ_Q is $\propto m_q^2/m_Q^2$. The ratio of the effective light and heavy quark mass is a parameter for this model and has be measured by experiment. By taking a factor of z^{-1} for longitudinal phase space, the Peterson fragmentation function for a heavy quark has the following form:

$$D_q^h(z) = \frac{N}{z[1 - 1/z - \epsilon_Q/(1-z)]^2} \tag{1.5}$$

where N is a normalization factor and can be derived from the following summation over all hadrons which contains Q:

$$\Sigma \int dz D_q^h(z) = 1 \tag{1.6}$$

From e^+e^- experiment measurements, ϵ_Q for b and c quarks are determined to be the following [22] :

$$\epsilon_c = 0.06^{+0.02+0.02}_{-0.01-0.01} \tag{1.7}$$

$$\epsilon_b = 0.006^{+0.001+0.002}_{-0.001-0.002} \tag{1.8}$$

It does satisfy the relationship of $\epsilon_c/\epsilon_b \propto m_b^2/m_c^2 = 10$. The above model and experimental data are mostly taken from meson fragmentation, while at CDF we assume the b quark is heavy enough that the effective mass of the diquark is similar to that of the antiquark in meson case, and $\epsilon_b^{\Lambda_b} = 0.006$.

Considering the Λ_b^0 case, for b baryon fragmentation, the light quark u and d form a spin-0 system so that the b quark carries all the spin of the the b baryon. From

predictions of the Heavy Quark Effective Theory(HQET), which will be discussed later, the degrees of freedom of the b quark are decoupled from the spin-0 diquark so that the Λ_b^0 carries all the information about the initial b quark with a small reduction [23]. Experimentally, AELPH and OPAL measured the Λ_b^0 polarization to be $P_L^{\Lambda_b} = (-23^{+25}_{-21})\%$ and $P_L^{\Lambda_b} = -0.56^{+0.20}_{-0.13}$ [24].

During the process of fragmentation, a b quark can pick up a lighter antiquark or a lighter diquark to form a meson or a baryon. Considering the heaviness of the b and c quark and omitting the possibility of a baryon containing a b and a c quark, the possible hadrons (integer charge) which can be formed during the fragmentation process are :

$$B^- — b\bar{u}$$
$$B_d^0 — b\bar{d}$$
$$B_s^0 — b\bar{s}$$
$$B_c^- — b\bar{c}$$
$$\Lambda_b^0 — bud$$
$$\Xi_b^0 — bus$$
$$\Xi_b^- — bds$$
$$\Sigma_b — buu,\ bud,\ bdd$$
$$\Omega_b^0 — bss$$

Among these, all except Σ_b decay via weak interaction. The b hadron production fraction estimates at the Tevatron are listed in table 1.4 [7]. CDF discovered the B_c [25], and LEP had the first indications of Ξ_b production [26], but the Ω_b has not yet been observed.

Table 1.4: Fractions of weakly decaying b hadron in $p\bar{p}$ collisions

b hadron	fraction [%]
$B^-/\bar{B}^0$	38.8 ± 1.3
B_s^0	10.6 ± 1.3
b baryons	11.8 ± 2.0

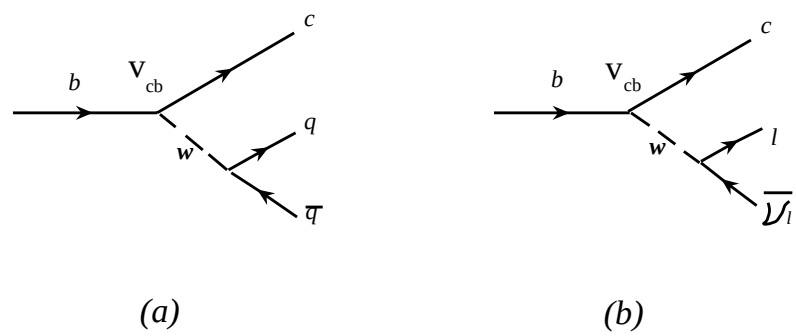

Figure 1.5: b hadronic decay (a) and b semileptonic decay (b)

1.4 b Hadron Decay

A b quark usually decays into a c quark emitting a W boson, and the W decays into quark-antiquark or lepton-antilepton pair since there is not enough energy to make a real W. The transitions of $b \to cq\bar{q}$ and $b \to c\ell\bar{\nu}_\ell$ are shown in Figure 1.5. One possible interesting measurement from Λ_b decays is the CKM matrix element V_{cb}, which determines the coupling strength of the b-c vertex. Since quarks only exist inside hadrons because of the quark color confinement, what we observe are actually hadron decays. Λ_b is considered as the ground state of b,u,d quarks, so it can not decay via strong or electromagnetic interaction, instead it decays weakly through the b-c quark transition. The Λ_b semileptonic decay and one example of its hadronic decays are shown in Figure 1.6 and Figure 1.7, respectively.

Compared with Λ_b hadronic decays, the semileptonic decays (e, μ channel) have the following advantages from both theoretical and experimental views. First, since leptons are not sensitive to the strong force, the decay diagram is simplified and the

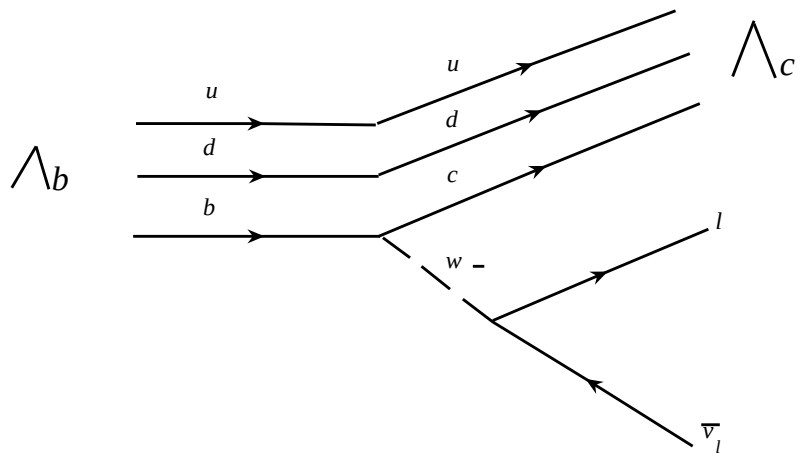

Figure 1.6: Λ_b semileptonic decay.

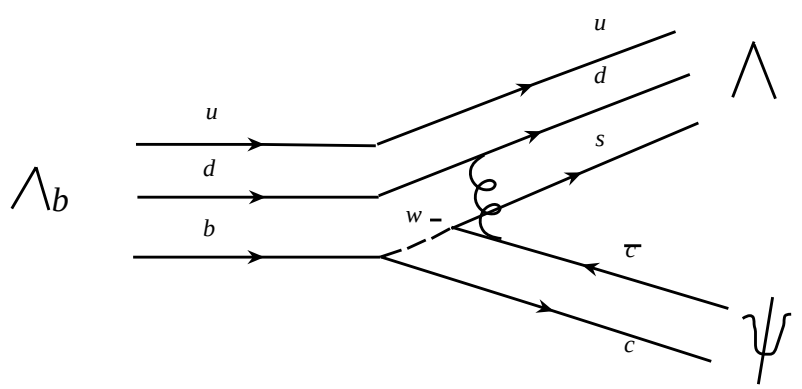

Figure 1.7: An example of Λ_b hadronic decay.

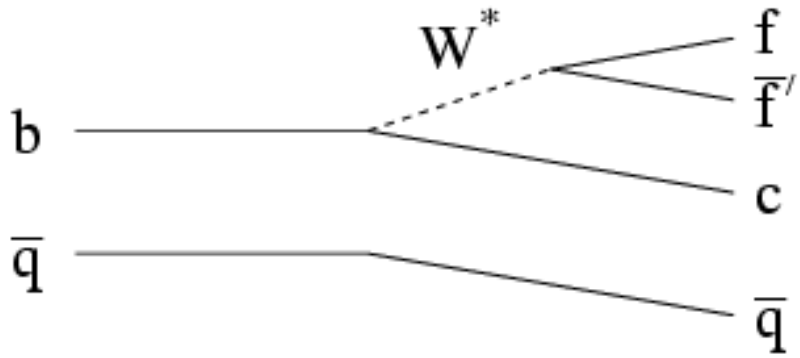

Figure 1.8: A B meson decay in the spectator model, there is no effect from the accompanying antiquark, so all b hadrons have the same lifetime.

gluon interactions between the final quarks are reduced (Figure 1.6). For hadronic decays, there are interactions between the final quarks (Figure 1.7), and this makes the decay more complicated. Second, the fact that the b quark is much more massive than u, d quarks simplifies the decay process. The momentum of the heavy quark is changed only slightly, below the QCD scale ($\Lambda_{QCD} \sim 200MeV$), by the low energy interactions within the hadron, and this makes the b quark largely decoupled from the ud diquark. This will be discussed in the spectator model and Heavy Quark Effective Theory later. Third, from the point view of experiment, the leptons (e, μ) are easier to identify. This is very important at a hadron collider because of the large hadronic background.

1.4.1 The Spectator Model of b Hadron Decay

The spectator model is the simplest decay model for heavy quarks like b and c and it is displayed in Fig. 1.8. In this model, the effect of the other quarks in the hadron are ignored, so they are spectators. This is because the large mass of the heavy quark. Any interaction between the heavy quark and the accompanying quark or diquark only have a small effect on the b quark. In addition, the lepton is not

sensitive to the strong interaction. Thus the b quark moves at the same speed as the whole hadron. In other words, the heavy quark is essentially at rest in the hadron rest frame and acts as a static gluon source, so the effect of the heavy quark's mass and spin can be neglected. By simplifying the b hadron semileptonic decay as the process of $b \to c\ell\nu$, the matrix element of this transition can be written as :

$$M_{sl} = -\frac{G_F}{\sqrt{2}} V_{qb}[\bar{q}\gamma^{\mu}(1-\gamma_5)b][\bar{\ell}\gamma_{\mu}(1-\gamma_5)\nu_{\ell}] \tag{1.9}$$

where G_F is the Fermi coupling constant. This matrix element is analogous to that of muon decay. By squaring the matrix element and integrating over the phase space, the decay rate becomes:

$$\Gamma_{sl}(b \to q) = \frac{G_F^2 m_b^5}{192\pi^3}|V_{qb}|^2 F(\epsilon) \tag{1.10}$$

where $\epsilon \equiv m_q/m_b$, the phase space factor—$F(\epsilon)$ is given by [27]:

$$F(\epsilon) = 1 - 8\epsilon^2 + \epsilon^6 - \epsilon^8 - 24\epsilon^4 ln\epsilon \tag{1.11}$$

Table 1.5: bottom and charm hadrons lifetimes

bottom hadrons	lifetime(ps)	charm hadrons	lifetime(ps)
B^0	1.542 ± 0.016	D^0	0.4117±0.0027
B^+	1.674 ± 0.018	D^+	1.051±0.013
B_s	1.461 ± 0.057	D_s	0.490±0.009
Λ_b	1.229 ± 0.080	Λ_c	0.200±0.006

Bottom hadrons have equal lifetimes and so do the charm hadrons in the spectator model. The experimentally measured charm and bottom hadrons are listed in Table 1.5. The prediction of the spectator model agrees better with the data for bottom hadrons than charm hadrons. This is because the bottom quark is much heavier than charm quark. However, the difference between the bottom hadron lifetimes is not negligible, so a more accurate model is needed to explain the differences. The HQET theory will be discussed in next section.

In the case of semileptonic decay, the exclusive decay $\Lambda_b \to \Lambda_c \ell \bar{\nu}_{\ell}$ dominates the Λ_b decays to Λ_c observed at CDF. In the lepton+SVT sample, the transverse momentum

of the lepton is required to be greater than 4 GeV, and furthermore the transverse momentum of Λ_c is required to be greater than at least 5 GeV, so there is not too much energy left for additional hardons. The three body decay, $\Lambda_b \to \Sigma_c \ell \bar{\nu}_\ell$ is suppressed by isospin symmetry, and $\Lambda_b \to \Lambda_c^* \ell \bar{\nu}_\ell$ needs a relative angular momentum change for the diquark and this is suppressed by the heavy quark limit. However, theoretical estimates of Λ_b decays to excited states can be 25% to 33% of the Λ_b semileptonic decays [37].

1.4.2 The Heavy Quark Effective Theory

The Heavy Quark Effective Theory (HQET) was introduced by N. Isgur and M. B. Wise. Then many authors developed the HQET theory and its applications(see the review by M. Neubert [29]). In the spectator model, the effect from the heavy quark is totally neglected, but in the HQET theory, the residual effect of strong interaction from heavy quarks is expanded as orders of Λ/m_Q—where Q is the heavy quark. This is based on the fact of that the QCD scale $\Lambda \sim 200MeV$ is much smaller than the heavy quark mass (for example, $m_b \sim 4.5$ GeV). The decay rate in the HQET framework can be described as:

$$\Gamma = \Gamma_0 + \frac{\Lambda^2}{m_b^2}\Gamma_2 + \frac{\Lambda^3}{m_b^3}\Gamma_3 + ... \tag{1.12}$$

where Γ_0 is the term which describes the spectator model. Γ_2 is called Fermi motion and chromomagnetic interaction. This $1/m_q^2$ term is typically around 5% in beauty decays. Γ_3 is called pauli interaction and weak annihilation (meson) or W-scattering (baryon) with weak annihilation being helicity suppressed. These are the main terms driving the differences in the lifetime of various hadrons [30]. However, currently typical theoretical prediction of the lifetime ratio between Λ_b and B_0 is bigger than 0.9. Two examples of the theoretical prediction are:
I.Bigi [17]:

$$\tau(B^-)/\tau(B^0) \simeq 1 + 0.005(f_B/200MeV)^2$$
$$\tau(B_s)/\tau(B^0) \simeq 1 + O(1\%)$$
$$\tau(B_c) \simeq \tau(D^0) < 10^{-12}s$$

$$\tau(\Lambda_b)/\tau(B^0) \simeq 0.9 - 0.95$$

where f_B is the B meson form factor, $\sim$ 200 to $250MeV$.
M. Neubert and T. Sachrajda [32]:

$$\tau(B^-)/\tau(B^0) = 1 + O(1/m_b^3)$$
$$\tau(B_s)/\tau(B^0) = 1.00 \pm 0.001 + O(1/m_b^3)$$
$$\tau(B_c) \simeq \tau(D^0) < 10^{-12}s$$
$$\tau(\Lambda_b)/\tau(B^0) = 0.98 + O(1/m_b^3)$$

While the prediction for B^- and B_s are consistent with the experimental results, and the prediction for Λ_b is far from the experimental result (see Table 1.5). For B_c, the experimental error is too big to have a real comparison with theory.

1.4.3 Λ_b lifetime status and motivation for the measurement

Table 1.6: bottom and charm hadrons lifetimes

Experiment	lifetime(ps)	reference
DELPHI	$1.11\ ^{+0.19}_{-0.18} \pm 0.05$	[33]
OPAL	$1.29\ ^{+0.24}_{-0.22} \pm 0.06$	[34]
ALEPH	1.21 ± 0.11	[35]
CDF	$1.32 \pm 0.15 \pm 0.007$	[36]

Currently the Λ_b lifetime measurements by four experiments are listed in Table 1.6 [7]. The results from LEP tend to be lower than CDF. LEP experiments include several channels such as $\ell + \nu_\ell + \Lambda_c$, $\Lambda_c \to pK\pi/pK_s/\Lambda\pi\pi\pi/\Lambda\pi/pK_s\pi\pi$, and $\ell + X + \Lambda$, where in this channel, vertex reconstruction and lepton impact parameter are both used to measure the lifetime. LEP experiments have the benefit of large boost ($\beta\gamma \simeq 6$ by assuming the b hardon takes away 70% of the beam energy and that the mass of b hadron to be 5.3 GeV, where $\beta\gamma = p/m$) with vertex resolution of about 200 μm, while CDF has smaller boost factor($\beta\gamma \simeq 2 \sim 3$ by assuming the interaction parton carries 10% $\sim$ 15% of the proton energy) but with better vertex resolution—about 50 μm in $\Lambda_b \to \ell\bar{\nu}_\ell\Lambda_c$ case. The Λ_b lifetime measurement is also a

direct observation of the weak $b \to c$ transition so it provides direct information of CKM matrix element V_{cb}.

In this analysis, the highest branching ratio of Λ_c decay channel $\Lambda_c \to pK\pi$ is selected to reconstruct Λ_c, and the combinatorial background is significantly reduced by applying particle identification to the proton by using TOF and dE/dx information.

Bibliography

[1] $http://www.encyclopedia.com/html/e/empedocl.asp$

[2] S.W.Herb et al, Observation of a Dimuon Resonance at 9.5 GeV in 400 GeV Proton-Nucleus Collisions, Phys. Rev. Lett. 39 (1977) 252.

W.R.Innes et al, Observation of Structure in the Upsilon Region, Phys.Rev.Lett. 39 (1977) 1240; Erratum,39 (1977) 1640.

[3] CDF Collaboration, Phys.Rev. D50 (1994) 2966;
CDF Collaboration, Phys.Rev.Lett 74 (1995) 2626;
D0 Collaboration, Phys.Rev.Lett 74 (1995) 2632.

[4] J. Sielaff, hep-ex/0105042;
The DONUT Collaboration, hep-ex/0012035;
$http://www-donut.fnal.gov/$.

[5] UA1 Collaboration, Phys. Lett. 122B (1983) 103;
UA2 Collaboration, Phys. Lett. 129B (1983) 130.

[6] Francis Halzen, Alan D. Martin, Quarks & Leptons, John Wiley & Sons, Inc.; Donald H. Perkins, Introduction to High Energy Physics, Cambridge University Press.

[7] Particle Data Group, Phys. Rev. **D50** part I, 1 (2002).

[8] A.W.P. Poon, hep-ex/0211013;
k2K Collaboration, hep-ex/0212007;
The SNO Collaboration, hep-ex/0205006;
The SNO Collaboration, hep-ex/0204086;
The SNO Collaboration, hep-ex/0204053;
The SNO Collaboration, Phys. Rev. Lett. 89 011301 and 011306 (2002);
The SNO Collaboration, Phys. Rev. Lett. 87 071301 (2001);
$http://www.sno.phy.queensu.ca/$.

[9] http://www.slac.stanford.edu/pubs/confproc/ssi81/ssi81-019.html.

[10] Belle Collaboration, hep-ex/030829, hep-ex/0309032;
CDF Collaboration, hep-ex/0312021, submitted to Phys. Rev. Lett.

[11] T. Nakano, et al, Phys. Rev. Lett. 91 (2003) 012002;
V. V. Barmin, et al, DIANA collaboration, hep-ex/0304040;
S. Stepanyan, et al., CLAS collaboration, hep-ex/0307018;
J. Barth,et al., SAPHIR collaboration, preprint.

[12] H. Takahashi, et al., Phys. Rev. Lett, 87 (2001) 212502.

[13] http://www.ihep.ac.cn;
http://www.lns.cornell.edu/public/CLEO/.

[14] Gordon Kane, Modern Elementary Particle Physics,Addison Wesley 1987.

[15] The LEP Working Group for Higgs Boson Searches, CERN-EP/2003-011.

[16] A.D.Martin, R.G.Roberts,W.J.Stirling, Phys. Lett. B306,145 (1993);
A.D.Martin, R.G.Roberts,W.J.Stirling, Phys. Rev. D47,867 (1993);
J.Botts et al. CTEQ Collaboration,Phys. Lett. B304,159 (1993).

[17] M. Shochet, FERMILAB-Conf-91/341-E.

[18] P. Nason, S. Dawson, R. K. Ellis,Nucl. Phys. B327,49 (1989).

[19] CDF collaboration, Phys. Rev. Lett, V75, 1451 (1995).

[20] M. Bishai et al, /CDF/PHYS/BOTTOM/CDFR/6285.

[21] C. Peterson, D. Schlatter, I. Schmitt, P. M. Zerwas, Phys. Rev. D27, 105 (1983).

[22] S. Bethke, Z. Phys. C29, 1175(1985);
J. Chrin, Z. Phys. C36, 165(1987);
W. Bartel, Z. Phys. C33, 339(1987).

[23] T. Mannel and G. Schuler, Phys. Lett. B279 (1992) 194;
J.G. Korner, A. Pilaftsis,and M. Tung, Z. Phys. C63 (1994) 575;
S. Groote, J.G. Korner, and M. Tung, Z. Phys. C74 (1997) 615.

[24] ALEPH Collaboration, Phys. Lett. B 365 (1996) 437;
OPAL Collaboration, hep-ex/9808006.

[25] CDF collaboratin, F. Abe et al, Phys. Rev. Lett. 81,2432 (1998);
CDF collaboratin, F. Abe et al, Phys. Rev. D58 81,112004 (1998).

[26] ALEPH Collaboration, D. Buskulic et al., Phys. Lett. B 384,449 (1996);
DELPHI Collaboration,P. Abreu et al, Z. Phys., C68,541 (1995).

[27] S. Stone, B Decays,"lifetimes", World Scientific, 1994;
J.L. Cortes, Phys. Rev. D25(1982) 188.

[28] E. Eichten, B. Hill , Phys. Lett. B 234(1990) 511;
H. Georgi, Phys. Lett. B240(1990) 447.

[29] M. Neubert,Phys. Rep. 245 (1994) 259.

[30] I. I. Bigi, hep-ph/0001003.

[31] I. I. Bigi, hep-ph/9508408.

[32] M. Neubert,C. T. Sachrajda, Nucl. Phys. B483,339 (1997).

[33] DELPHI Collaboration, EPJ C10 185.

[34] OPAL Collaboration, Phys. Lett. B426 161 C10 185.

[35] ALEPH Collaboration, EPJ C2 197.

[36] CDF Collaboration, Phys. Rev. D55 1142.

[37] Adam Leibovich and Iain Stewart, hep-ph/9711257.

Chapter 2

The CDF Detector at the Tevatron

2.1 The Fermilab Tevatron

For the time being, the Tevatron (proton-antiproton collider) is the highest-energy particle collider operational anywhere in the world. The initial goal for Run II is to achieve a luminosity of $8 \times 10^{31} cm^{-2} sec^{-1}$ and a integrated luminosity of 2 fb^{-1}. Currently the luminosity has reached a record of $4.75 \times 10^{31} cm^{-2} sec^{-1}$. However, it is thought that the ultimate potential of Run II can achieve up to $2 \times 10^{32} cm^{-2} sec^{-1}$, although this may need a reasonable length of time to achieve after the initial luminosity goal is reached.

A schematic diagram of the Fermilab accelerators is shown in Figure 2.1. The accelerating process starts with electrical discharges in a hydrogen gas bottle, where H^- ions are produced. These H^-'s are pulled out from the gas bottle by a Cockcroft-Walton which is a 750KV DC voltage source, and H^-s get accelerated to 750 KeV. Then they are accelerated to 400 MeV by a 500 foot long linear accelerator–called Linac. There the H^-s are accelerated through AC electromagnetic waves generated by a series of cavities in Linac, and as a result, the continuous beams are separated into several bunches. Then the two electrons are stripped off by letting the ions pass through a thin carbon foil and the protons are injected into the Booster ring, which is a circular accelerator with a circumference of 475 m. The energy of the protons is increased to 8 GeV in the Booster ring and then the protons are injected into a larger

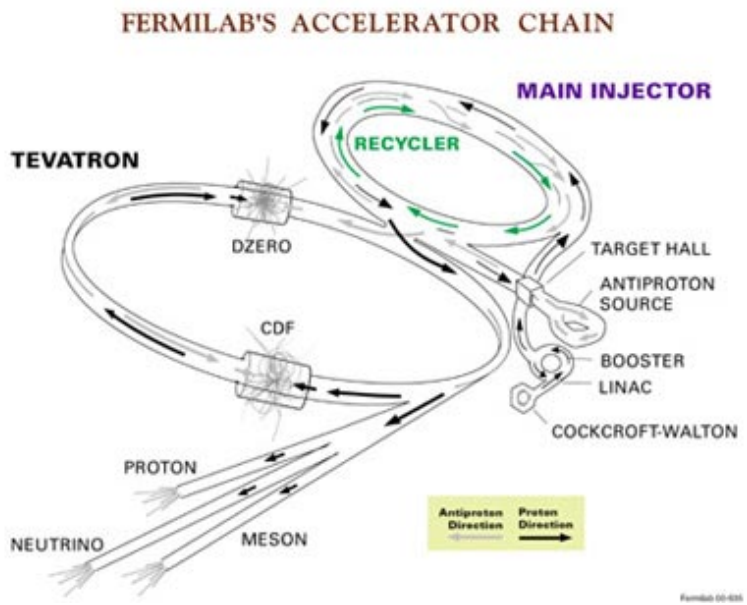

Figure 2.1: A schematic diagram of the Tevatron.

circular accelerator–the Main Injector. The Main Injector adds energy to the proton up to 150 GeV–for fixed target experiments, or up to 120 Gev–for the $p\bar{p}$ collision at Tevatron.

When the beam is running for the Tevatron, a fraction of the proton beam will be extracted to bombard a Tungsten target to produce antiprotons. These antiprotons have a wide spread both in energy and direction, so they have to undergo a process called stochastic cooling to reduce the random motion [1]. There another ring called Accumulator will accumulate these cooled antiprotons, after sufficient accumulation, these antiprotons are injected back into the Main Injector. The antiprotons in the ring will get accelerated. When the energy of the protons and antiprotons reach 150 GeV, they are transferred into the Tevatron (with a circumference of 4 miles)–where the energies of the proton and antiproton will be increased to 1000 GeV. The protons and antiprotons share the same ring but move in opposite direction. Actually the protons and antiprotons are bent by superconducting magnets so that they will not collide inside the ring except in two points which will be discussed later. The good thing about an proton-antiproton collider is that the protons and antiprotons can

share the same ring and thereby greatly reduce the cost, but the luminosity is limited by the possible intensity of the antiproton beam. On the other hand, for the proton-proton collider, it will cost more money for another ring–because the two proton beams have to accelerated and stored in separate rings, but the luminosity can reach a much higher value [2].

There are two collision points at the Tevatron, the two detectors at the two collision points are called CDF and D0. There are quadruples at both ends of CDF to focus the beams into a small transverse cross sectional area width with a radius of about 35 μm. The instantaneous luminosity(L) at CDF can be written as :

$$L = \frac{N_p N_{\bar{p}} N_B f}{4\pi\sigma_A^2} \tag{2.1}$$

where N_p and $N_{\bar{p}}$ are the numbers of particles in proton and antiproton bunches, typically about the order of 10^{11} and 10^{10} respectively. N_B is the number of bunches in the Tevatron, which is 36 now. f is the revolution frequency at which proton or antiproton travel around the Tevatron, which is about 70 KHZ. σ_A is the cross sectional area, which is about $(35\mu m)^2$. The collision point forms a Gaussian distribution with a $\sigma = 30cm$ along the z direction. The time between each bunch crossing currently is about 396 ns. The average number of collisions in each crossing is about $1 \sim 2$ with the luminosity so far achieved.

2.2 The Collider Detector at Fermilab

CDF II is a general purpose solenoidal detector which combines precision charged particle tracking with fast projective calorimetry and fine grained muon detection [3]. The detector was constructed and is maintained by a multinational collaboration of physicists and designed for multipurpose physics topics. It is capable of studying top, QCD , electroweak and heavy flavor physics, as well as searching for Higgs, SUSY and exotic particles. As shown in Figure 2.2, it is nearly cylindrically symmetric with respect to the beamline, and forward-backward symmetric with respect to the nominal interaction point. The tracking system is in a 1.4 T axial magnetic field provided by a superconducting solenoid. At CDF, the antiprotons move in a direction which is from

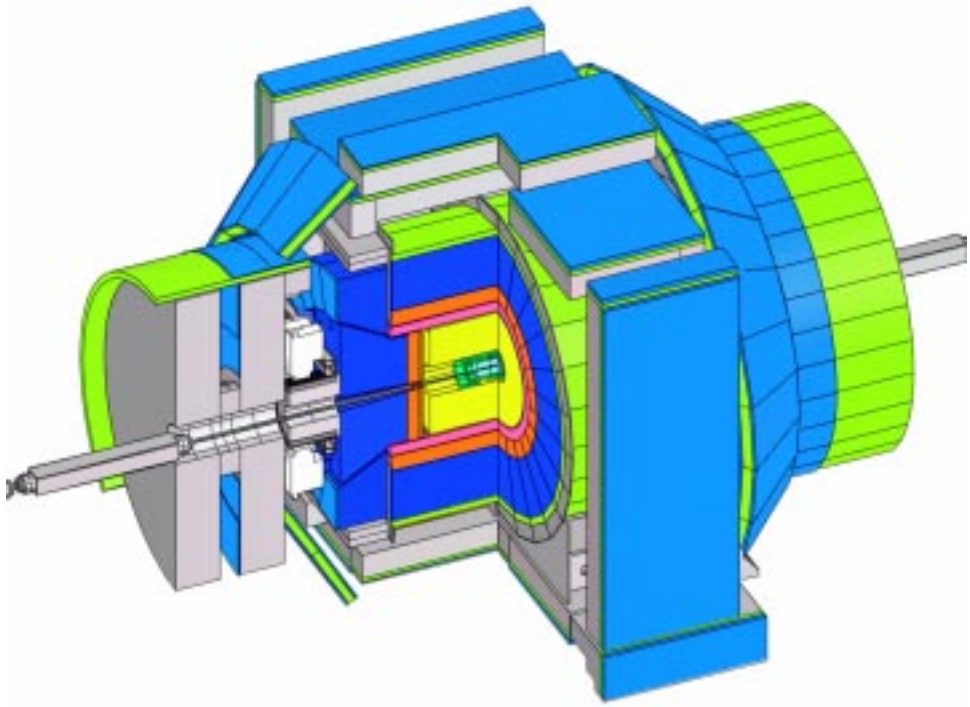

Figure 2.2: A view of the CDF II detector

west to east and is used as the z direction, the north horizontal direction is defined as the x direction, and up is defined as the y direction, forming a right-handed coordinate system. The rapidity, which is defined as:

$$y = \frac{1}{2} \ln \frac{E + P_z}{E - P_z} \tag{2.2}$$

is often used instead of the polar angle θ in the laboratory coordinate frame. The advantage of rapidity is that a change of rapidity is a constant $\delta y = \tanh^{-1} \beta$ under a boost in z direction with velocity β. For the case where $E >> m$, the rapidity can be approximated by pseudo-rapidity:

$$\eta = \frac{1}{2} \ln \frac{E + P_z}{E - P_z} = -\ln \tan(\frac{\theta}{2}) \tag{2.3}$$

The interaction point at CDF is not at the coordinate (0,0,0), however, the reconstructed default track at CDF assume it is from (0,0,0), so the pseudo-rapidity calculated from default track is not exactly the pseudo-rapidity and this is called detector pseudo-rapidity.

When a particle is created in the $p\bar{p}$ collision, the momentum and charge are measured by the tracking system if the particle is a charged particle. The subtracking system-Central-Outer-Tracker (COT) will measure dE/dx for charged particles which is useful for particle identification. Right outside the tracking system, there is the Time-of-Flight detector which measures the time-of-flight of particles and it is very useful for particle identification in the Λ_b lifetime measurement. Besides the TOF system, there is the calorimeter in which hadron, electron, photon deposit most of their energy. This is useful to identify electrons and photons. Unlike hadrons and electrons, muons only deposit minimum ionization energy in the calorimeters, so a muon system outside the carlorimeter is used to identify muon. Further details of these systems, plus the Cherenkov Luminosity Counters(CLC) and trigger methods are described below.

2.2.1 Cherenkov Luminosity Counter

In Run II, a Cherenkov Luminosity Counter(CLC) has been built to measure the luminosity. It is designed to measure Run II luminosity with an uncertainty of 5% or less in the very high rate regime of $L \sim 2 \times 10^{32} cm^{-2} s^{-1}$ [4]. There are CLC modules in the CDF detector, installed at small angle in the proton (East) and antiproton (West) directions with rapidity coverage between 3.75 and 4.75. Each module consists of 48 thin, long, gas-filled, Cherenkov counters. The counters consist of three concentric layers around the beam-pipe, each layer has 16 counters and points back to the collision point, as shown in Figure 2.3.

2.2.2 Tracking System

At CDF, the tracking system is composed of two parts, the Central Outer Tracking(COT) and the Silicon Tracking. For historical reasons, the silicon tracking is divided into three parts: "Layer Zero Zero" (L00), "Silicon Tracking at Run II" (SVX II) and the "Intermediate Silicon Layers" (ISL). However, because of unfinished alignment, only the COT and SVX II are currently used for physics analysis currently. The tracking system provides precision momentum measurement of charged

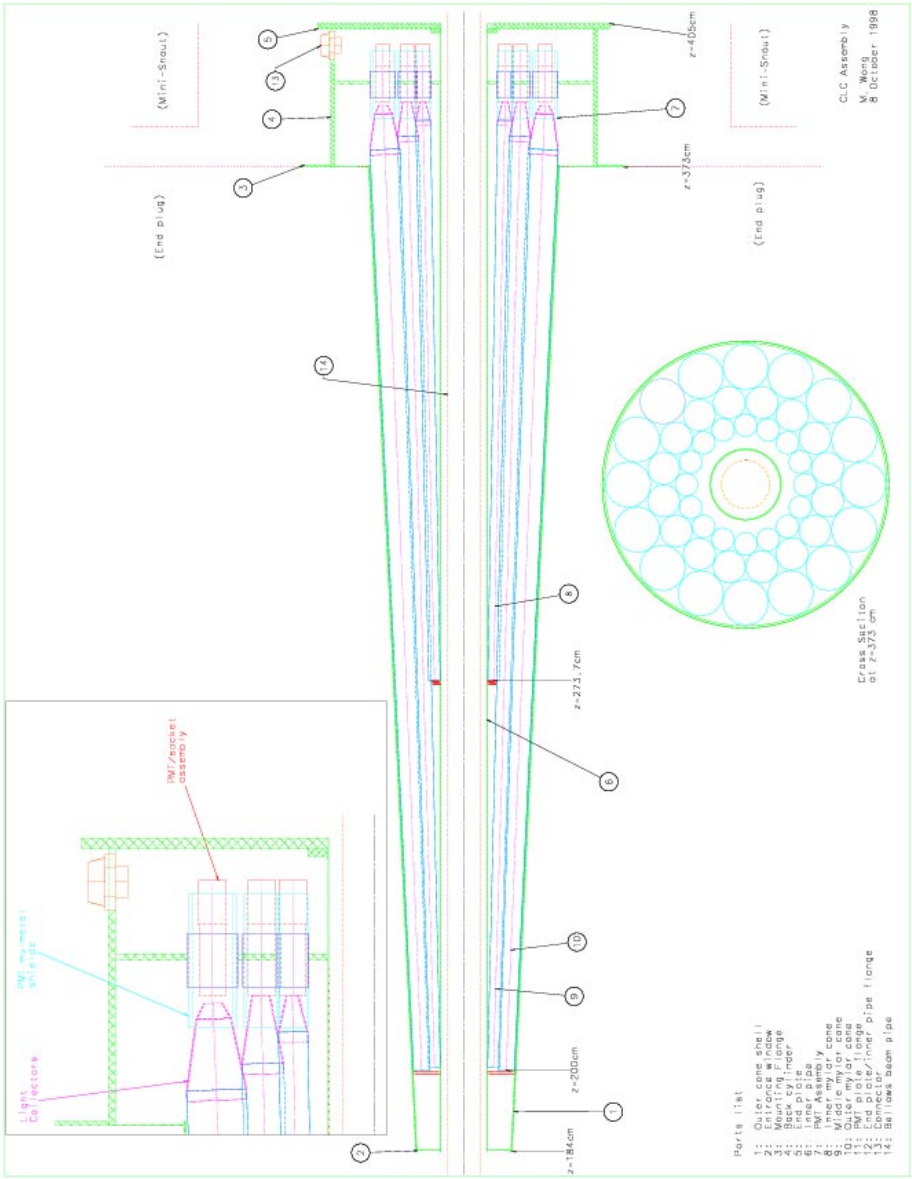

Figure 2.3: The CDF II CLC detector

particles by combining the COT and silicon tracks and extrapolating tracks down to the interaction point. We can reconstruct both the primary vertex, corresponding to interaction point and displaced vertices, corresponding to the long lived particles like b hadrons. Since the b quark has a relatively long lifetime, the tracking system provides a means of b identification. This is very important for Higgs searches and for top physics because both Higgs and top mainly decay via the b quark. For b physics, this is extremely important, not only for b identification, but also the lifetime measurements directly depend on the displaced vertex. Even for other measurements like mass measurements it is still very useful for it can reduce the huge QCD background in the $p\bar{p}$ collision environment by requiring a good displaced vertex. Moreover, when combined with the Calorimeter and muon system, the tracking system can provide information for electron, photon, and muon identification, and the dE/dx information provided by COT can be used for hadron particle identification which is an important part of the Λ_b lifetime measurement.

SVX II Tracking

The silicon detector consists of three parts: L00(Layer-Zero-Zero), SVX II and ISL (Intermediate Silicon Layers) [3] [10]. An end view and a side view of the silicon tracking system are shown in Figure 2.4. L00 is a single-sided layer of 48 ladders mounted directly on the beampipe, at a radius of 1.5 cm from the beamline, which is designed to enhance the impact parameter resolution. The SVX II is a replacement of the Run I silicon detector. It has three barrels , each 29 cm long, and there are 12 wedges in ϕ, each with five layers of silicon(layer0–layer 4). It is 360 double-sided ladders in a layout of six 15 cm axial sections $\times$ twelve 30° ϕ slices $\times$ five radial layers between 2.5 and 10.6 cm. The ISL covers the area between the SVX II and the COT detector (layer 5 and 6), with 296 double-sided ladders at radii of 20 or 28 cm, in total 1.9 m long, providing silicon hits out to $|\eta| < 2$. In total there are 8 layers (7 layers for central region), 704 ladders, 722432 channels for the whole silicon detector. Among the 8 layers, layer 0, 1, 3 have a 90 degree stereo design (two sides tilted by 90 degree) while 2, 4, 5, 6 have a small angle stereo design (two sides tilted by a small

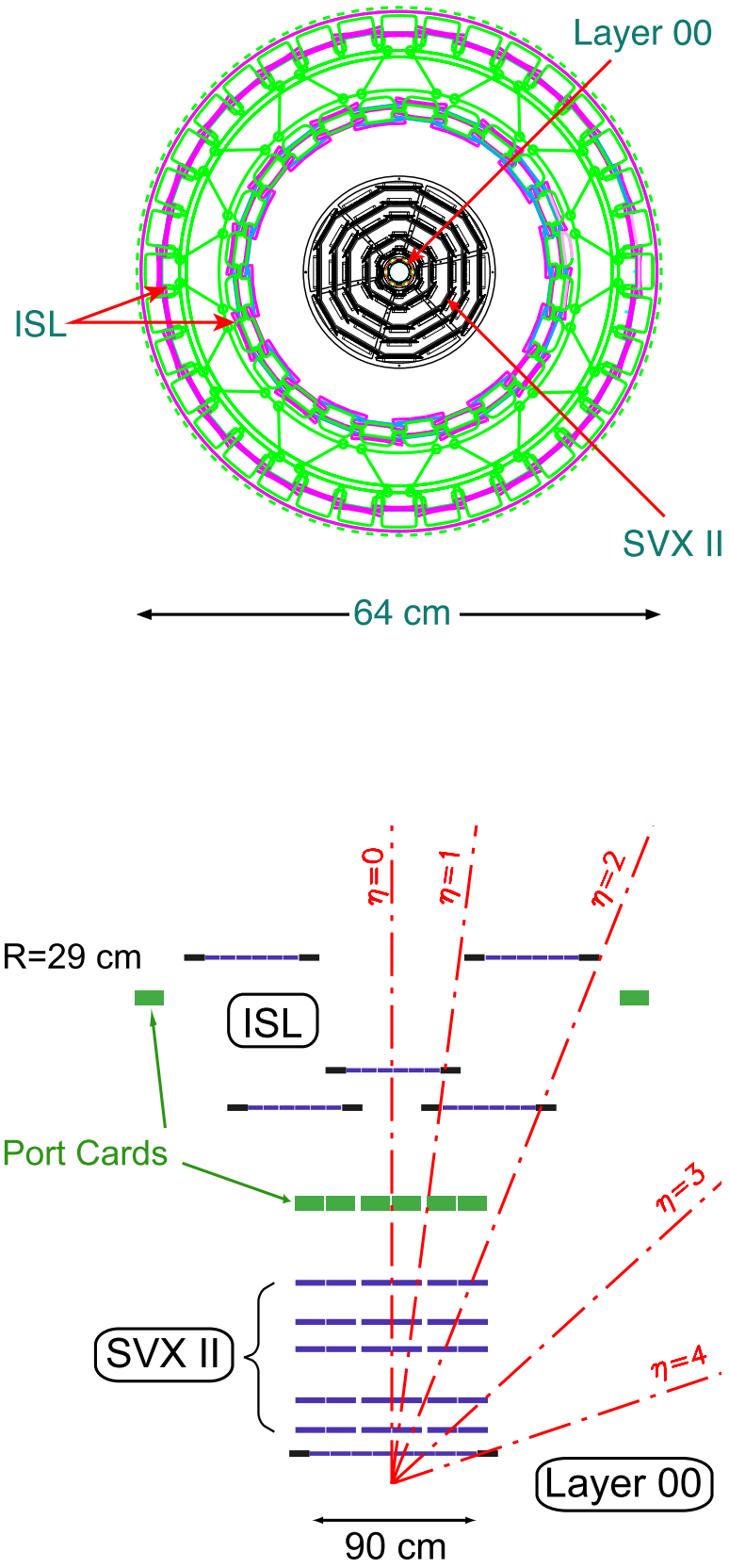

Figure 2.4: End view (top) and side view (bottom) of the CDF II silicon system

angle of 1.2^o).

The silicon detector is formed from small silicon wafers, each is about 30 cm long, 8 cm wide and 1 mm thick. These wafers are either from Hamamastu or MICRON. Before the wafers get mounted into the detector, the bulk capacitance-voltage , bulk capacitance-leakage voltage and selected strip leakage current are measured.

On one face of each silicon wafer there are hundreds of metal strips, each separated by 60-65 μm. The bulk silicon is n-doped, but under each strip is a p-doped region, resulting a high density array of pn diodes, and this face is the p side of the detector. On the other face, under each strip is a n-doped region implanted with higher n-typed material. Between the n-typed diodes, there is a p-typed diode to separate those n-typed diodes. This is the n-side of the detector. The p-side is used to measure the $r\phi$ position of a particle and the n-side is used to measure the rz position of a particle. When a charged particle passes through the active volume of the silicon detector, some electrons in the valence band will be excited into conduction energy bands and this results in some charges and "holes". These charges and holes are swept out of the diode region by the electric fields, and eventually the metal strips pick them up. With its high strip density, the silicon detector is a high resolution tracker. Taking the spatial distance of the strips as 60 μm, ideally the expected resolution in $r\phi$ can be: $60/\sqrt{12} = 18\mu m$ for the transverse impact parameter resolution. This is very powerful to identify a b track.

COT Tracking

COT is a large cylindrical drift chamber constructed to replace original CDF's central drift chamber for the expected high luminosity at Run II [3] [6], as shown in Figure 2.5. It covers the detector region of radius from 43.4 cm to 132.3 cm. Its length is about 310 cm along the beam covering η from -1.1 to 1.1. The entire azimuth, ϕ, is covered. There are 96 radial sense wire layers which are grouped into eight "super layers", and each super cell has 12 sense wires and a maximum drift distance that is approximately the same for all super layers. Therefore the number of super cells in a given layer scales approximately with the radius of the super layer. Among the

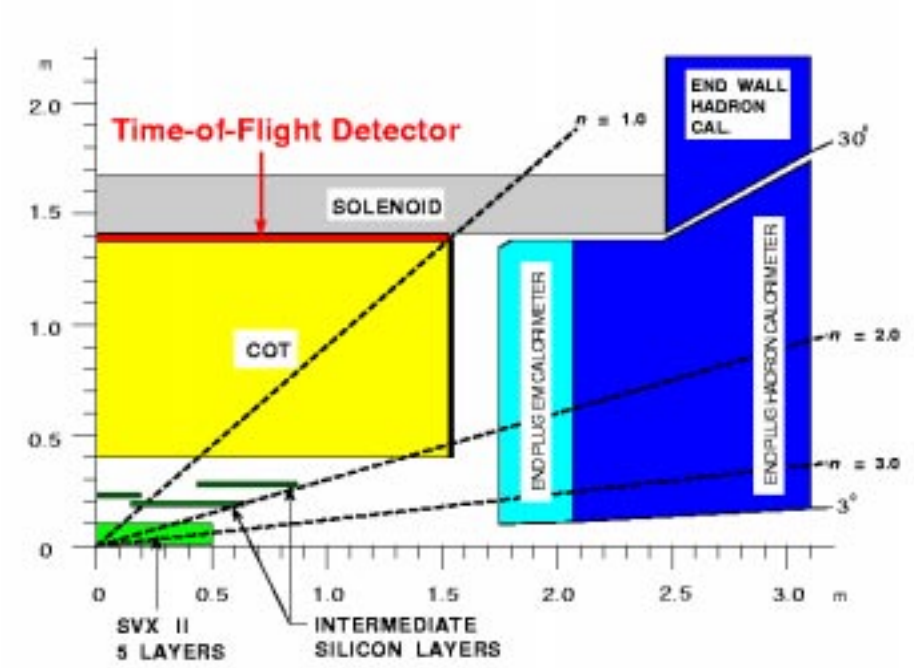

Figure 2.5: Side view of the central region of the CDF(quarter section)

sense wires, approximately half of the wires are axial(run along the z direction) and half of them are small angle(2 degree) stereo. Charged particles ionize gas molecules, and the resulting electrons and ions then drift along paths determined by the electric and magnetic fields and are picked up by the sense wires. From the drift time of ions in the electric field, the track producing the ionization can be reconstructed in space and the pulse height can be used to measure the amount of ionization. The main impetus for the upgrade of the COT at Run II is ensure that the maximum drift time is less than the 396 ns of the bunch spacing in 36 bunch operation and less than 132 ns in 108 bunch operation (The original Run II design). A maximum drift time of about 100 ns is achieved in the COT, which has a maximum drift distance of 0.88 cm, when using a fast drift velocity gas mixture as Argon/Ethane/CF_4(50:35:15). A more standard gas like Argon/Ethane(50:50)(maximum drift time of about 177 ns and maximum drift distance of 0.88 cm) is used now for running with 36 bunches. Within each superlayer, the sense wires in all layers form a cell structure with a tilt angle of 35° with respect to the radial direction in order to resolve the left-right

ambiguity when reconstructing the tracks. In Run I , the Central-Tracking-Chamber (CTC) had a $r\phi$ resolution about $200\mu m$, a longitudinal resolution about 1 mm, and a momentum resolution is better than $\delta p_T/p_T^2 < 0.002(GeV/c)^{-1}$ [7]. While in Run II, a similar performance is expected.

An Amplifier/Shaper/Discriminator(ASD) chip was developed in the COT [8]. One function of the ASD is to encode the magnitude of the charge deposited in the chamber cell in the trailing edge of the discriminator output pulse, and the leading edge of the discriminator is logarithmically related to the total charge deposited on the sense wire, therefore providing the dE/dX information of a charged particle [9]. In the analysis of the Λ_b lifetime measurement, dE/dX was used for proton identification.

2.2.3 Calorimetry

Outside the solenoid is the calorimeter system, which absorbs particles and measures the resulting energy depositition [3] [11]. Because of the different characteristics of energy loss of different particles, which will be discussed later, the electromagnetic calorimeters are always put before the hadronic calorimeters, so that the particles will reach the electromagnetic calorimeters first and the electrons and photons will deposit most of their energy there. The calorimeter system covers a broad range in pseudo-rapidity from -4.2 to 4.2 by several components. The central region of CDF, $|\eta| < 1.1$ for Central-ElectroMagnetic calorimeter (CEM) and $|\eta| < 0.9$ for Central-HAdron calorimeter (CHA), was covered by the CEM and CHA. A Wall-Hadronic-Calorimeter (WHA) is used to complete the pseudo-rapidity coverage of CHA($< 0.7|\eta| < 1.3$ for WHA). A schematic view of the CDF II calorimeter system are shown in Figure 2.6 and one of the central wedges is shown in Figure 2.7. The plug and forward electromagnetic and hadronic carlorimeters, PEM, FEM, PHA, FHA, combine to provide a $1.1 < |\eta| < 4.2$ coverage. Only CEM and CHA are used for the Λ_b lifetime measurement. The central calorimters are divided into halves at $\theta = 90^o$. Each half is 2.5 m long and segmented into 24 wedges in the azimuthal direction and 10 towers in η. The size of each tower is 0.1×15° in the $\eta - \phi$ space. These towers form a projective geometry which point back to the collision point.

Most hadrons lose their energy by nuclear interaction in the steel absorber of the hadronic calorimeter. Photons tend to lose their energy quickly via pair production, and electrons via bremsstrahlung. Muons, on the other hand, tend to deposit little energy in absorbers and will be detected by the muon detectors outside the calorimeters. The characteristic length of electron energy loss due to electromagnetic interaction is roughly:

$$X_0 = \frac{716.4\ gcm^{-2}A}{Z((Z+1)\ln(287/\sqrt{Z})} \tag{2.4}$$

where X_0 is the radiation length, Z and A is the atomic number and mass number of the absorbors, respectively. What is important is that the energy loss per unit is larger per unit length for higher-Z absorbers, in contrast with the hadronic energy loss for which the characteristic length is roughly:

$$\lambda_I = 35\ gcm^{-2}A^{1/3} \tag{2.5}$$

due to the nuclear interactions. In this case, the energy loss is less for higher $A \propto Z$. It is this difference makes the two kinds of calorimeter construction possible–an inner electromagnetic calorimeter made of high-Z absorber to detect electrons and photons, and a larger outer hadronic calorimeter made of relatively inexpensive low-Z absorber to detect hadronic particles. At CDF, the inner CEM is constructed of lead aborber plates interspersed with plastic scintillator, and outer CHA is constructed of steel absorber and plastic scintillator. The plastic scintillator planes collect light from the showering particles and guide it to the phototubes which convert the light into electrical signals. A significant difference between electrons and hadrons lies in the transverse size of their showers: electron showers tend to be small, a few centimeters across, while hadronic showers tend to be large, on the order of tens of centimeters across. The calorimeter tower geometry allows some checking of the transverse energy distribution. Since the electrons (photons) tend to deposit all their energy into electromagnetic calorimeter, and hadrons only deposit a fraction of their total energy into electromagnetic calorimeter, the ratio of a particle energy deposition into these two detectors is used to distinguish between electrons and hadrons. Moreover, there is a layer of wire proportional chambers (CES, shown in Figure 2.8) near shower

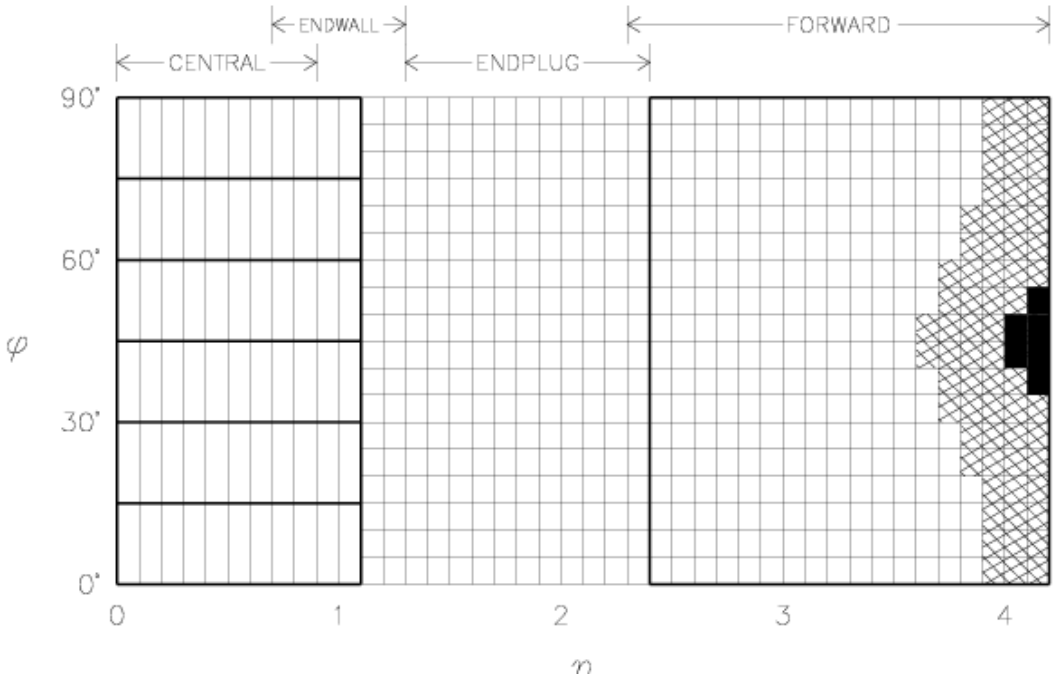

Figure 2.6: A schematic view of the CDF II calorimeter system.

maximum in the CEM, which provides good shower size, shape, and position measurement. This is very useful for the matching between a track and a tower for electron identification.

2.2.4 Muon Chambers

Because the muon is 200 times heavier than the electron, bremsstrahlung radiation is about 40000 times weaker than for an electron, so muons deposit only a little energy in the calorimeters, which totally absorb most other particles. In order to identify muons, there are several muon detectors outside the calorimeters. Moreover, muon is a charged particle so the tracking system can measure its charge and momentum. Combining the information from a muon detector and tracking system, CDF can provide a good muon identification [3]. There exist four muon detectors outside the calorimeters: CMU(Central Muon Detector), CMP(Central Muon Upgrade), CMX(Central Muon Extension), IMU(Intermediate Muon System). The muon cov-

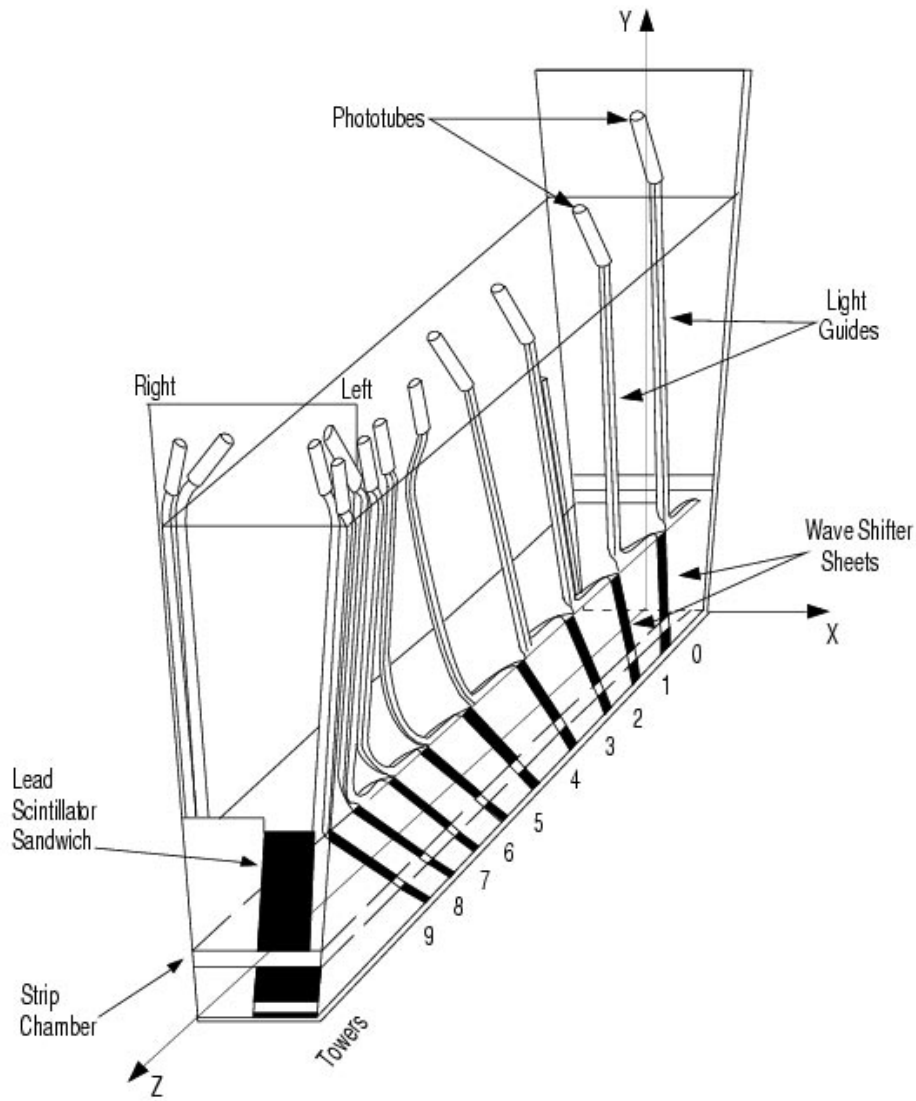

Figure 2.7: A 15° calorimeter wedge.

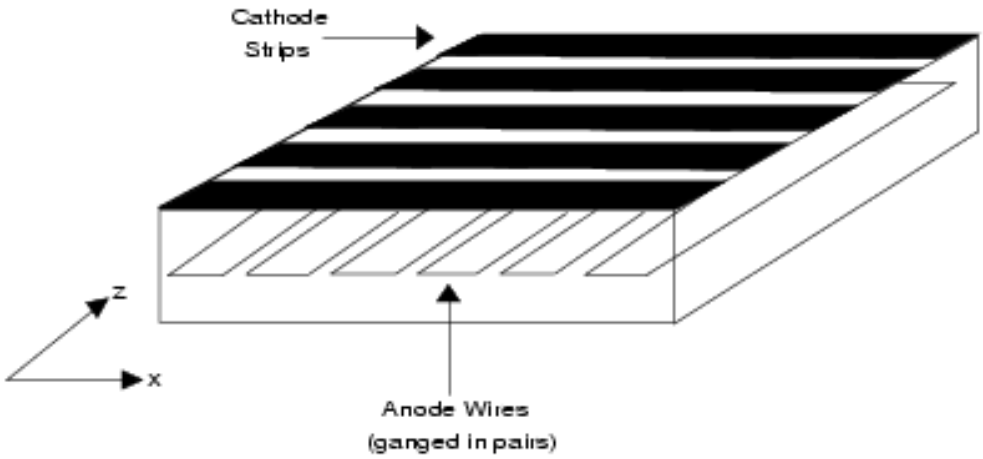

Figure 2.8: A schematic view of CES.

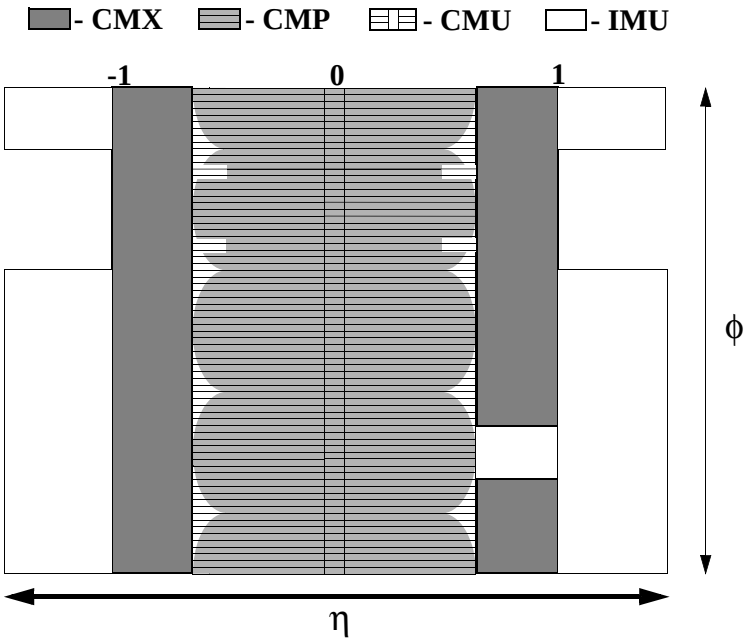

Figure 2.9: Muon system coverage in $\eta - \phi$ space.

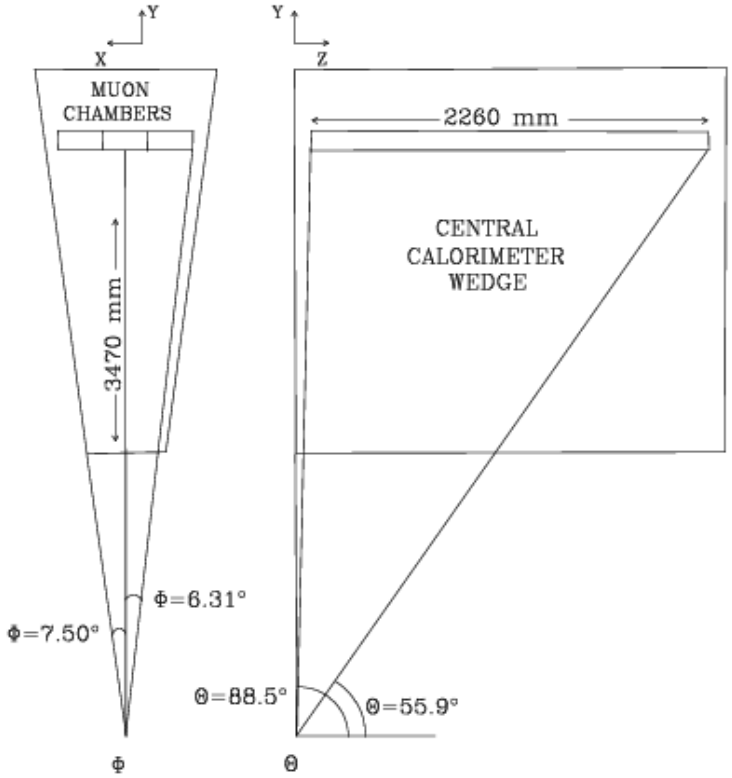

Figure 2.10: A wedge of CMU.

erage in $\eta - \phi$ is shown in Figure 2.9.

The CMU is separated into two halves at $\theta = 90^o$, each half is segmented into 24 wedges. The wedge segmentation in the ϕ direction is the same as the central calorimeter. As shown in Figure 2.10, each wedge has three towers, which covers 226 cm in z direction, and each tower consists of 16 cells. Each cell has a cross section of 2.68 $\times$ 6.35 cm. The drift time information recorded by the stainless steel wire in the center of each cell is used to calculate the muon $r - \phi$ position, while the charge distribution along wires is used to determine the z position. This information will be used for the muon match between muon stub and the tracks from tracking system.

CMP consists of a second set of muon chambers behind an additional 60 cm of steel in the range of $55^o < \theta < 90^o$, and it is located outside of the magnetic field's return

yoke. The chambers are of fixed length in z and form a box around the central detector, thus the pseudo-rapidity coverage varies with azimuth as shown in Figure 2.9. Basically the CMP overlaps the region covered by CMU, but requiring additional CMP stub matching can further reject the hadron punch-through background. Both CMU and CMP cover the pseudo-rapidity up to 0.6.

The CMX is a extension of the central muon detector, covering polar angle from 45° to 55°, and therefore extends the pseudo-rapidity coverage from 0.65 to 1.0. In order to improve the muon identification efficiency, IMU was designed to extend the pseudo-rapidity coverage to 1.5 and offline identification up to 2.0. However, CMX and IMU information are not used for the analyses.

2.2.5 TOF Detector

A Time-of-Flight(TOF) detector has been added to the CDF II detector to enhance the particle identification [12]. The primary goal is to provide a 2σ separation between $\pi^{\pm}$ and $K^{\pm}$ for momentum $p < 1.6GeV/c$. By combining it with dE/dx it is expected to improve the neutral B meson flavor determination. Another purpose of TOF detector is to search for highly ionizing particle–monopole [7]. Since the mass difference between π and proton is even bigger than the difference between π and K, the particle identification ability of selecting proton from pion by combining TOF and dE/dx together is very powerful in Λ_b lifetime measurement, as will be shown in next chapter.

The TOF detector consists of 216 bars of $4cm \times 4cm \times 280cm$ Bicron BC-408 scintillator located at a radius of 138 cm from the beamline in the 4.7 cm of radial space between the COT and the solenoid, as shown in Figure 2.5. It covers the pseudo-rapidity of CDF II detector from -1 to 1. A photomultiplier tube(PMT) of diameter 1.5 inches is attached to each end of every bar inside the 1.4 Tesla magnetic field of the CDF solenoid. The PMTs have a gain of about 30000. The output of the PMTs is used to measure the timing(through discriminator-TAC-Time-to-Amplitude-Converter and ADC-Amplitude-to-Digital-Conveter) and pulse height. Pulses of different magnitude will fire the discriminator at different times, resulting in a pulse height dependence of

the time measured by TAC. This effect is called the time walk. The measured pulse height is used to correct the TOF for the time walk.

The big challenge in making TOF functional is to calibrate it offline using data. The time measured for each ADC is parameterized by:

$$t(adc) = t_{stop} - (t_0 + tof + \frac{L/2 \pm z}{s} + t_c - \frac{\alpha}{\sqrt{Q}}) \tag{2.6}$$

where t_{stop} is the time of the common stop signal—at which the discriminator on certain channel is fired after the nominal $p\bar{p}$ bunch crossing time, t_0 responds the time at which the $p\bar{p}$ collision occurred, tof is the actual time of flight of the particle, L is the length of the scintillator bar, z is the position of the track hit along the bar, s is the effective speed of light propagation in the scintillator, t_c is a constant term related to cable and electronic delays, and $\alpha/\sqrt{Q}$ is the time walk correction, Q is the pulse height, α is a calibration constant. Currently, the mean value for the resolution of TOF at the face of the PMT is 122 ps, and the distribution has an r.m.s of 20 ps.

2.3 Trigger

The trigger plays an important role in hadron collider experiment because the collision rate is so high that each collision can not be read out and the data must be filtered to obtain interesting events. The maximum tape writing speed is 75 Hz and that is the limit for any trigger design. On the other hand, most of the events are just hadronic background; the interesting physics events are only a small fraction of the total events. By using the trigger to select different classes of interesting physics events, one can make the data storage and event processing much more efficient.

The online physics event selection process at CDF is achieved by three-layer trigger system(four layers if the minimum bias trigger is also regarded as one layer) [3] [13]. The idea for using multi-layer structure is to minimize the deadtime by using fast, relative simpler triggers to filter events to slower, more sophisticated triggers. Eventually, the purpose of any physics trigger path is to reduce the event rate to be less than 50 Hz after the events get through the Level 3 trigger.

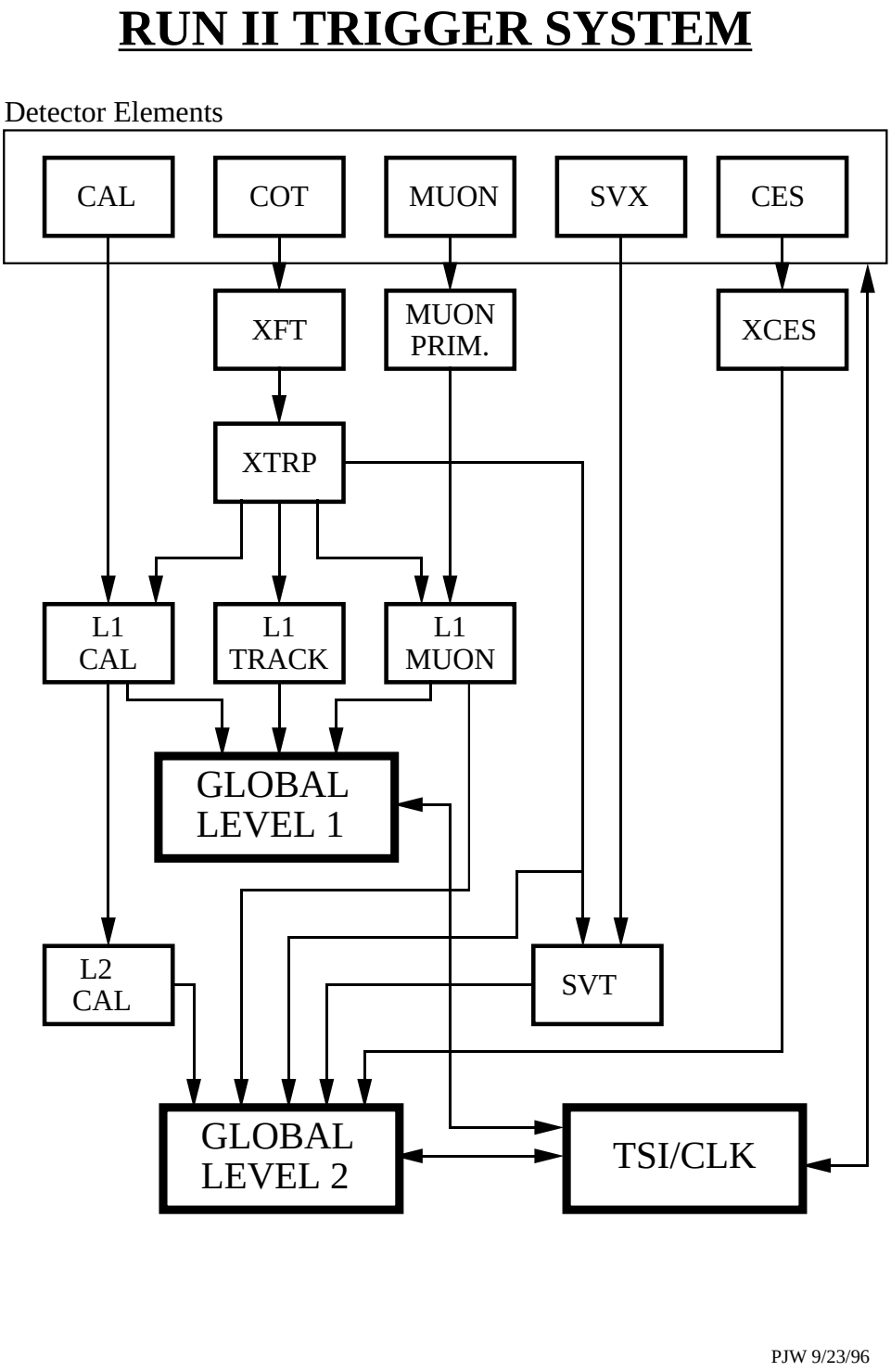

Figure 2.11: The run-II trigger-system block diagram.

The Run II trigger system block diagram is shown in Figure 2.11. The information from the calorimeter, COT, Muon, SVX II and CES are used to make trigger decisions. The XFT (the eXtremely Fast Tracker) uses the outer four superlayers of the COT to reconstruct a high momentum track by first finding track segments in each superlayer and then linking the found segments into a track. This process is done for each bunch crossing(396 ns for Run II), and therefore it must be highly parallel to be sufficiently fast. The XTRP(the Extrapolation Unit) is a unit that receives tracks from XFT and distributes the tracks or information derived from the track into Level 1 and Level 2 trigger subsystems. Muon Prim generates muon track candidates based on single hits and coincidence of hits in the scintillators of the muon system, while XCES produces muon track candidates based on the hits of wire chamber of the muon system. The L1 Muon trigger combines tracks from XFT and muon candidates from Muon Prim by means of a look-up table and sends the derived information to Global Level 1 subsystem so that Level 1 can make decision for any trigger path related to muons. The L1 CAL trigger combines calorimeter information from a set of eight bits for each 15 degree wedge segment, and XFT track information by means of a look-up table and sends them to Level 1 trigger subsystem. The L1 TRACK trigger will generate a L1 accept signal if 5 or more tracks were found, otherwise it will send track information to Global Level 1 subsystem. After sending out the Level 1 trigger information, all tracks are put into a pipeline and stored pending the L1 decision. If an accept decision is made by L1 trigger, this information will be delivered to Level 2 electronics.

L2 CAL reduces the event rate by adding E_t information from a cluster of trigger towers and then sends information to Level 2 trigger subsystem. The SVT (Silicon Vertex Tracker) was designed for displaced track trigger. The silicon hits information gets clustered by an internal hit finder, then the found clusters combines with the tracks from XFT in its Associative Memory(AM), and the AM implements the pattern recognition by means of a look-up table. Once a pattern is recognized, the XFT track along with the found silicon hits are fitted and send to L2 subsystem to make a decision. The L2 subsystem has four buffers. When a event has been written into one of these buffers, it starts to make a decision. Currently the L1 accept rate is required

to be less than 20 kHz, L2 accept rate is required to be less than 350 Hz.

Level 3 trigger will make a decision based on the full detector information and the fully reconstructed events in a processor farm.

Specifically for the Λ_b lifetime analysis we used the lepton+SVT trigger path: at Level 1, a CMU and CMP muon with $p_T > 4GeV$ is required for muon+SVT sample, a CEM tower with $E_T > 4GeV$, $p_T > 4GeV$, and the ratio of energy deposited into Hadronic and EM calorimeter is required to be less than 0.125 for electron+SVT sample. At Level 2, an SVT track with $120\mu m < |d_0|$ (impact parameter) $< 1mm$, $p_T > 2GeV$ correlated with $p_T > 4GeV$ CMUP track with $5^o < \Delta\phi(\mu, SVT) < 90^o$ for muon+SVT sample, the same requirement on the SVT track and its correlation with the electron, plus a XCES 4 GeV track is added for electron+SVT sample. At Level 3, for both muon+SVT and electron+SVT samples, the level-2 objects should be confirmed, lepton cuts should be applied and reconstructable charm should be checked, however, this has not being implemented now.

For the X(3872) mass measurement, we used the di-muon trigger, at Level 1, which requires two tracks from muon chambers, and at Level 2 each track must have a $p_T > 1.5$ GeV/c. At Level 3, the invariant mass of the two tracks is required to be in the range of 2.7 to 4.0 GeV/c^2.

Bibliography

[1] D. Mohl, G. Petrucci, L. Thorndahl and S. van der Meer, Phys. Rep. 58, 73(1980)

[2] $http://lhc-new-homepage.web.cern.ch/lhc-new-homepage/$

[3] CDF Collaboration, FERMILAB-Pub-96/390-E.

[4] CDF luminosity group, "The Performance of the CDF Lumonosity Monitor",submitted to NIM, May 2002;
CDF luminosity group,CDF/DOC/CDFR/CDF4330.

[5] Kai Yi, et al,CDF/DOC/TRACKING/CDFR/5896.
W.-M. Yao and K. Bloom, CDF/TRACKING/DOC/CDFR/CDF5991.

[6] COT group,CDF/PUB/TRACKING/PUBLIC/6267.

[7] F. Abe, et al, Nucl. Ins. Meth., A271,387(1988)

[8] F. M. Newcomer et al, IEEE Trans. on Nucl. Sci., 40(1993)

[9] Shin-Shan Yu et al, CDF/DOC/BOTTOM/PUBLIC/6361.

[10] S. Nahn,CDF/PUB/TRACKING/PUBLIC/6264.

[11] R. Erbacher et al,CDF/PUB/CALORIMETRY/PUBLIC/6135.

[12] C. Grozis et al, "The Time-of-Flight Detector at CDF", Nucl. Phys. Proc. Suppl. vol. 47 (2001) 344.
C. Grozis et al, "A Time-of-Flight Detector for CDF", Int. J. Mod. Phys. A16S1C(2001) 1119.

[13] Trigger group, CDF/PHYS/TRIGGER/CDFR/4718

Chapter 3

Particle Identification

Currently, the particle identification at CDF is based on the following features: electrons are identified by their tracks in the tracking system and their energy profile in the Calorimeters; muons are identified by their tracks in the tracking system and the hits they caused in the muon chambers; while hadrons are identified by their tracks in the tracking system, their ionization energy loss (dE/dx) in COT, and their TOF information collected by the TOF detector. In the Λ_b lifetime measurement, TOF information was used to identify proton for the first time. Combined with dE/dx, the performance to select protons from pions is excellent.

3.1 Electron Identification

3.1.1 Longitudinal and Transverse Shower Sharing

Although the CDF calorimeter covers η from -4.2 to 4.2, in the Λ_b lifetime measurement, only the region covered by the tracking system is used, so only the Central-ElectronMagnetic(CEM) and Central-HAdron(CHA) calorimeters are discussed. The energy sharing in the calorimeters can be divided into two situations: Longitudinal sharing, the energy sharing between CEM and CHA for the same tower, and Transverse sharing, the energy sharing between towers. For electrons, the energy sharing between towers is only in the η direction, since the CEM is constructed such that the

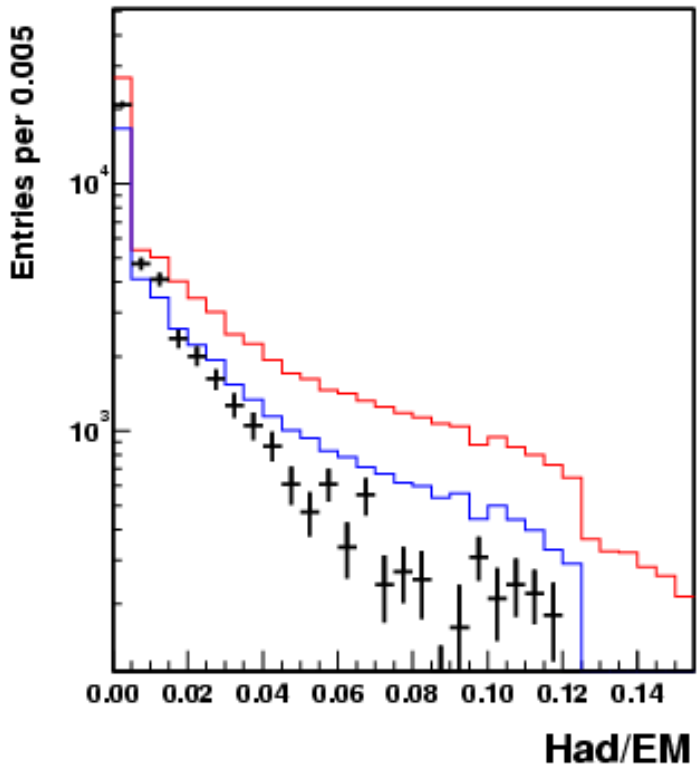

Figure 3.1: The Hadem distribution for electrons, the red (or gray in black-white) line is the distribution for default electron candidates, the blue curve is the distribution for electrons which passed the LeptonSvtSel model [2], and the black one is the distribution of sideband subtracted electron candidate for electron+D^0 sample.

eletromagnetic energy is not shared across ϕ boundaries.

In the Longitudinal case, electrons will first meet the CEM and deposit most of their energy, while hadrons deposit little energy into the CEM and go deeper to meet the CHA and deposit most of their energy into the CHA. The variable "Hadem" is defined as the ratio of hadronic to electromagnetic transverse energy measurements and this variable is used to distinguish electrons from hadrons. A distribution of electron Hadem in lepton+SVT sample is shown in Figure 3.1 [2]. The cut of Hadem$<$ 0.125 is used to select electrons. However, this cut also implies an isolation requirement because an electron surrounded by hadrons, such as a b jet, tends to have a higher Hadem value and most likely will be rejected.

The behavior of the transverse shower profile of electrons and hadron is also very useful to identify the electrons from hadrons. Typical electron showers are only a few centimeters in diameter, and the shower is well contained within a single tower, whereas hadronic showers have larger sizes and usually tend to span across several towers. The energy sharing among adjacent towers occurs when a electron enters the boundary of two adjacent towers in the η direction. Therefore electrons can be also identified by their distinct lateral energy profile. A χ^2-like quantity–Lshr is defined to express the lateral energy sharing profile:

$$Lshr = 0.14\Sigma\frac{M_k - P_k}{\sqrt{0.14^2 E_T + (\Delta P_k)^2}} \tag{3.1}$$

where the summation is over its n-1 adjacent towers, and n denotes the two-tower or three-tower case. M_k is the measured energy in one tower, P_k is the predicted energy given the CES z measurement. The term of $0.14\sqrt{E_T}$ is the electromagnetic energy measurement resolution, and ΔP_k is the estimated uncertainty of P_k, which is the P_k change due to a 1 cm change in z. A distribution of Lshr is shown in Figure 3.2. At Level 2 trigger a cut $Lshr(n = 2) < 0.2$ is applied, while offline trigger confirmation requires $Lshr(n = 3) < 0.2$.

3.1.2 Shower Shape

The electromagnetic shower max can provide the information about the electron shower shape both in the z view and the $r\phi$ view, and this can be compared with data from test beam measurements [1]. A measurement of the shower shape match both in z and $r\phi$ view is given by the following χ^2 formula:

$$\chi^2 = \frac{1}{4}\Sigma_{i=1}^{11}\frac{q_i^{obs} - q_i^{pred}}{\sigma_{q_i}^2} \tag{3.2}$$

where q_is are normalized pulse heights and σ_{q_i}s are the uncertainties. The distributions of the χ^2 in z(strip) and $r\phi$(wire) view are shown in Figure 3.3. A cut of $\chi^2 < 10$ in both z and $r\phi$ view are required in the Λ_b lifetime analysis.

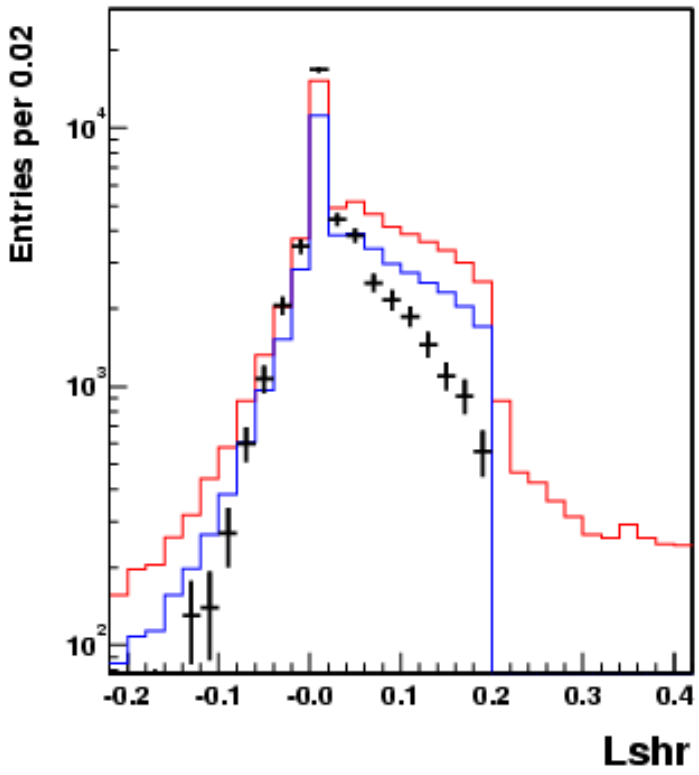

Figure 3.2: The Lshr distribution for electrons, the red (or gray in black-white) line is the distribution for default electron candidates, the blue curve is the distribution foe electrons which passed the LeptonSvtSel model [2], and the black one is the distribution of sideband subtracted electron candidate for electron+D^0 sample.

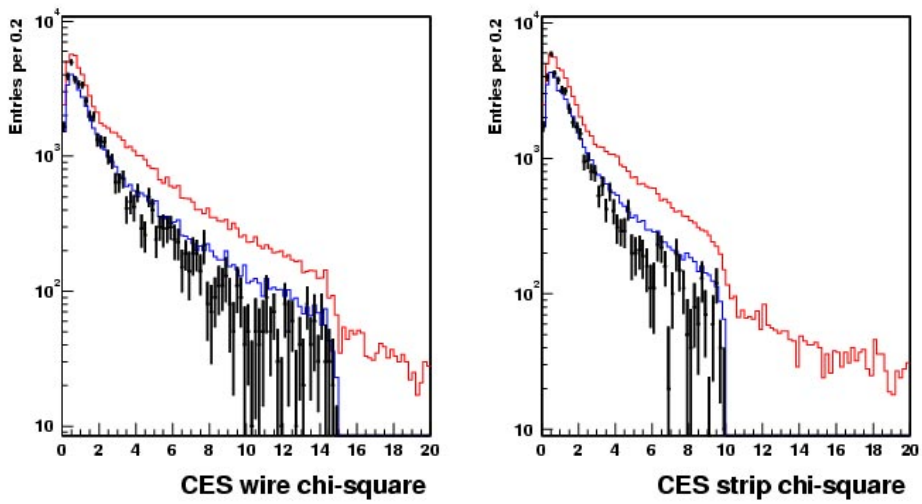

Figure 3.3: CES matching χ^2 in x and z direction distribution. For electrons, the red (or gray in black-white) line is the distribution for default electron candidates, the blue curve is the distribution for electrons which passed the LeptonSvtSel model [2], and the black one is the distribution of sideband subtracted electron candidate for electron+D^0 sample.

3.1.3 Track-cluster Matching

An electron will leave a track in the tracking system and hits in the shower max, and deposit energy into the calorimeter. Therefore the matching or consistency among this position information in three detectors can be used to identify electrons. The best wire and strip cluster in the CES are selected to be the highest-energy cluster consistent in position with the calorimeter, and the best track is taken to be the highest-p_T track pointing to any tower in the cluster. In the Λ_b lifetime analysis, the candidate track is required to be a silicon track which has at least three $r\phi$ silicon hits.

By extrapolating the track into the CES, the difference between the CES cluster position and the extrapolated position from the track can be calculated. The position in $r\phi$ view(wire) is denoted as x and the position in z view(strip) is denoted as z. The distributions of the differences between x and z are shown in Figure 3.4. The $\Delta x < 2$cm and $\Delta z < 3$cm cuts are required for electron candidate.

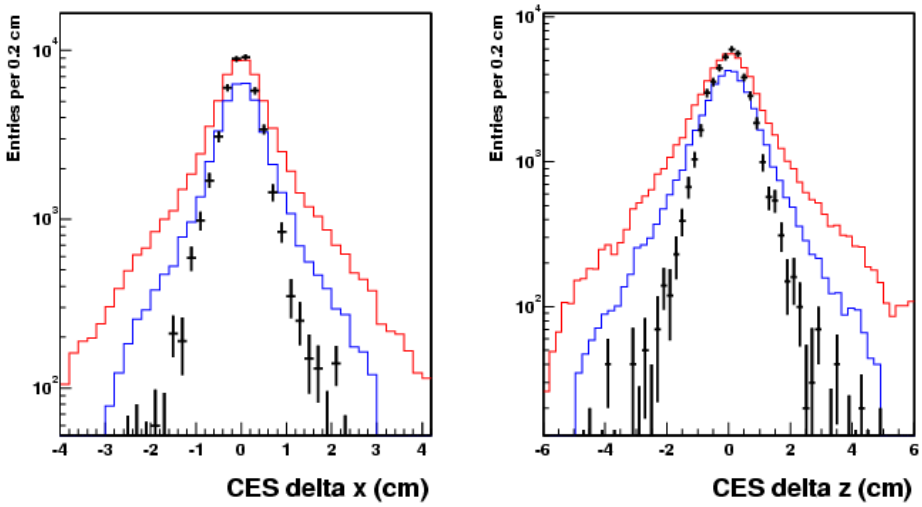

Figure 3.4: CES position difference in x and z direction (Δ_x and Δ_z) distribution. For electrons, the red (or gray in black-white) line is the distribution for default electron candidates, the blue curve is the distribution for electrons which passed the LeptonSvtSel model [2], and the black one is the distribution of sideband subtracted electron candidate for electron+D^0 sample.

The energy measured by the CEM and the momentum measured by the tracking system should be consistent for a electron candidate. The electron mass can be neglected, so the ratio between E_T and p_T (E/p)should peak at 1. A distribution of E_T/p_T is shown in Figure 3.5. A cut of $0.5 < E_T/p_T < 1.5$ is required.

3.1.4 Electron removal of γ conversions

The photon conversions to e^+e^- pairs are an electron background. The two electrons produced in photon conversions are nearly parallel to each other so that the difference of the track parameter $cot\theta$ between these two tracks is very small, and since these two tracks are produced at the same point, the transverse separation, Sep_{xy}, between these two tracks should also be small. To remove the photon conversion background, the $\Delta cot\theta$ and Sep_{xy} are calculated for an electron candidate with other oppositely charged tracks. These two quantities from a γ conversion sample are shown in Figure 3.6 and Figure 3.7 [3]. A photon conversion is identified if $Sep_{xy} < 0.2cm$

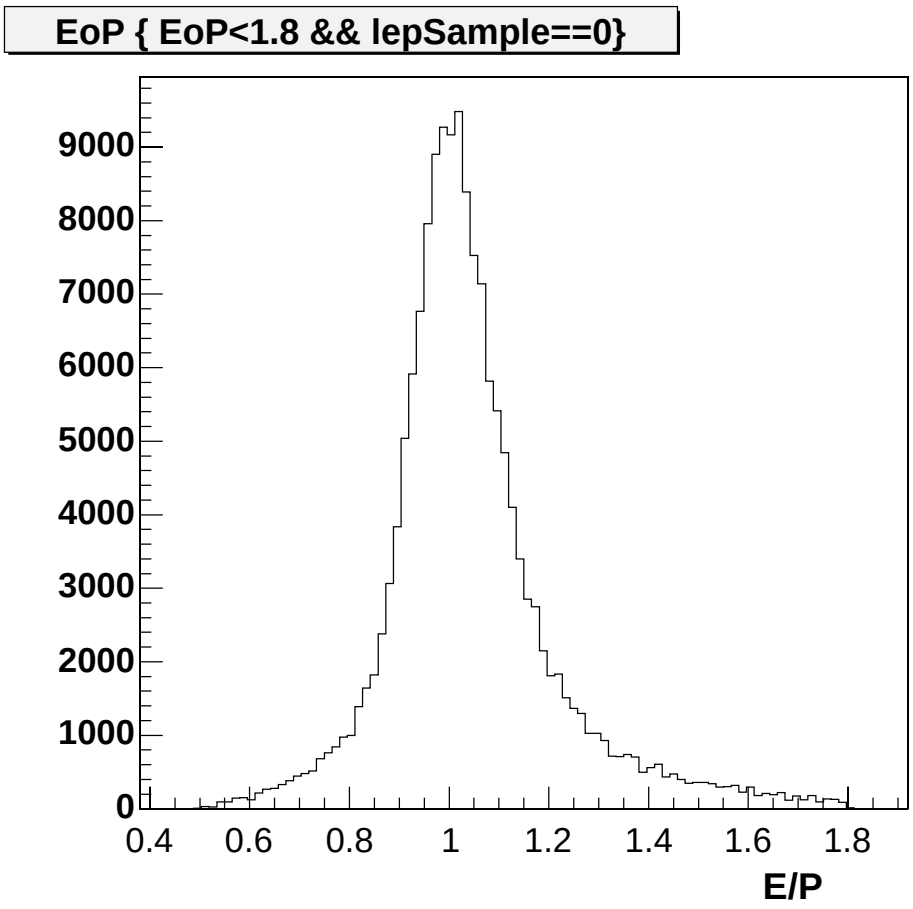

Figure 3.5: E/p distribution for electron in electron+SVT sample.

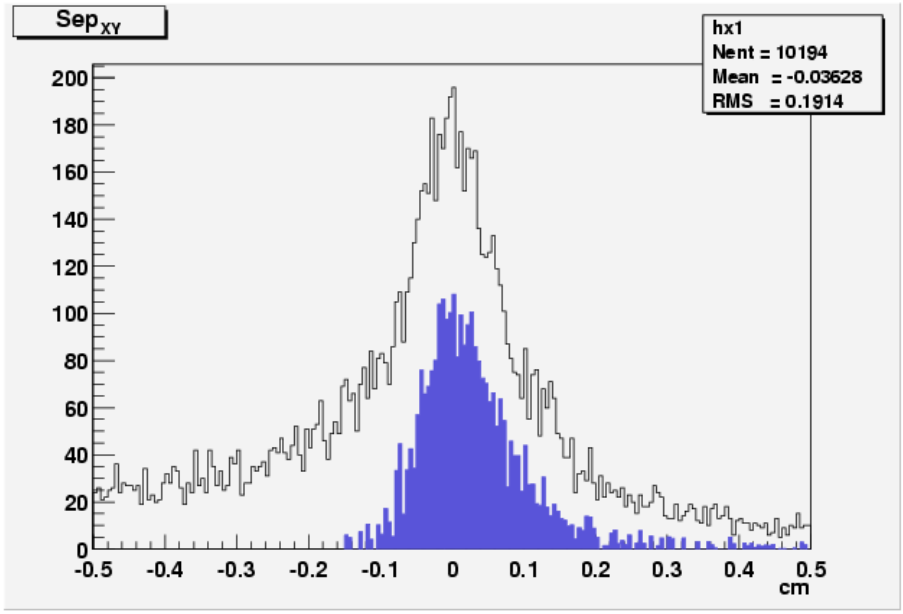

Figure 3.6: Sep_{xy} distribution of conversion electrons for the momentum range 1.0 to 2.0 GeV. The black histogram is for all default cuts; the blue (or gray in black-white) one is the same distribution after sideband subtraction in $\Delta cot\theta$.

and $|\Delta cot\theta| < 0.006$, and if so the identified electron candidate will be removed from the data sample. However, this method can not remove all the photon conversions because some partner tracks of photon conversion can not be reconstructed due to the detector acceptance.

3.1.5 Fiducial Requirement and Trigger Confirmation

To make sure that the quantities measured by CEM and CES are well measured, some fiducial cuts are applied. A cut of $|x_{CES}| < 21.5cm$ is applied to make sure that the electron candidate falls far away from CEM's wedge boundary. In order to choose good electrons which are well measured by CES, the z_{CES} is required to be between 9.0 cm and 200 cm.

In this analysis, a SemiLeptonic/LeptonSvtSel offline filter module is [2] used to confirm all the trigger requirements, while other cuts are implemented separately.

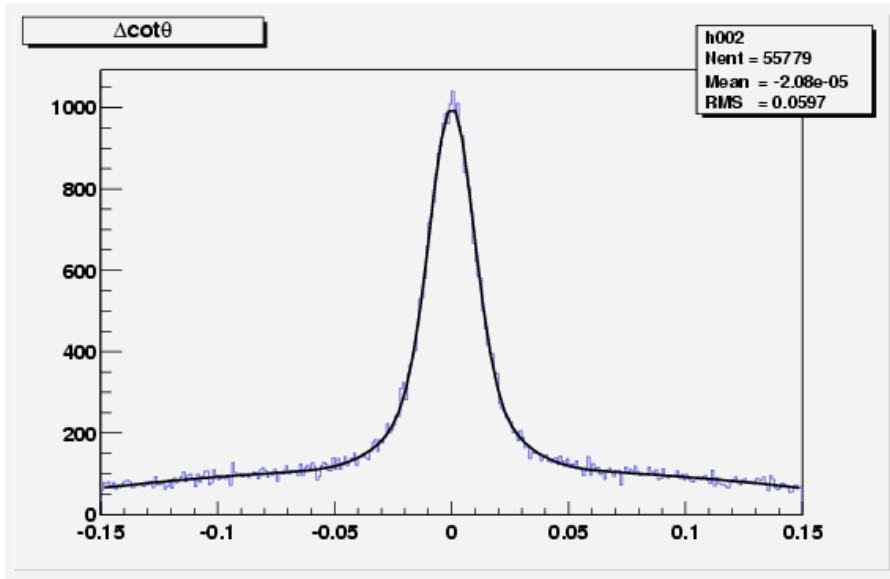

Figure 3.7: $\Delta cot\theta$ distribution of the conversion electrons for the momentum range 1.0 to 2.0 GeV.

3.2 Muon Identification

Muon identification at CDF is based on the two facts: a muon is a charged particle which leaves a track in the tracking system and a muon can penetrate material more easily than all other charged particles. Because of the latter fact, a muon can traverse the calorimeter and reach the muon system to create hits in the muon chambers, while electrons deposit most of their energy into electromagnetic calorimeter and hadrons deposit most of their energy into hadronic calorimeter.

3.2.1 Track-Muon chamber matching

The track left by a muon in the tracking system can be extrapolated into the CMU muon chamber and be be compared with the position of the track reconstructed in the muon chamber. A muon hit cluster in the muon chamber may match to more than one track in the tracking system. So the best matched(minimum χ^2) is selected as the muon candidate. A match variable, the $r\phi$ position difference $|\Delta X|$, is required to be less than 15 cm in trigger level. In order to reduce the hadron punch through

background, a further requirement of the match between the track and the CMP muon chamber is applied offline to the muon candidate, $|\Delta X| < 10$ cm. Furthermore, the χ^2 of the position match between track segments in the CMU and CMP and the extrapolated track is required to be less than 9 in $r\phi$ plane offline.

3.3 Proton Identification

While dE/dx was used for a few analyses at Run I, the current Λ_b lifetime analysis uses TOF for particle identification for the first time at CDF. In the Λ_b lifetime measurement, the background from B decays such as $\ell + D^+ + \bar{\nu}_\ell$, $\ell + D_s^+ + \bar{\nu}_\ell$, $\ell + D^* + \bar{\nu}_\ell$ should be excluded as much as possible because they contaminate the Λ_b lifetime measurement. Since most tracks are pion tracks, and the pion tracks contribute a lot of combinatorial background, this background can be significantly reduced by selecting protons from pions. The dE/dx and TOF have different separation power in different momentum ranges and are complementary in different momenta, which will be discussed later. In the Λ_b lifetime measurement, dE/dx and TOF are combined to select protons from pions.

3.3.1 dE/dx

A charged particle will lose energy by means of ionization when it traverses material. If the incident energy is moderately relativistic, ionization is the primary energy loss except for electrons. The energy loss per unit length in material is defined as dE/dx. The average dE/dx by ionization is described as Bethe-Bloch formula [4]:

$$\frac{dE}{dx} = \frac{4\pi N e^4}{mc^2\beta^2} z^2 (\ln \frac{2mc^2\beta^2\gamma^2}{I} - \beta^2 - \frac{\delta(\beta)}{2}) \tag{3.3}$$

where

- N is the number density of electron in the material

- m is the electron mass
- z is the charge of the incident particle
- I is the mean excitation energy of the material
- $\beta = v/c$
- $\gamma = 1/(1-\beta^2)$
- $\delta(\beta)$ is the correction of the density effect at high β

When a charged particle passes through the gas volume inside the COT, it leaves an ionization trail along its flight path. The amount of ionization charge deposited is proportional to dE/dx, so the dE/dx can be calculated from the deposited charge after calibration. However, CDF uses the measured deposited charge to represent dE/dx. From the Bethe-Bloch formula, the dE/dx is only a function of the particle velocity $\beta\gamma$ for a given gas inside a drift chamber. Because of this characteristic, particles with different mass can have quite different dE/dx in certain momentum ranges, and this feature can be used for particle identification. Figure 3.8 shows the dE/dx for different particles as a function of momentum. The particle separation power is defined as the difference between two particle types divided by dE/dx resolution. Even though the COT is not optimized for dE/dx measurements, the dE/dx still has certain separation power. Figure 3.9 shows the dE/dx particle separation powers as a function of momentum. The mean dE/dx as a function of $\beta\gamma$ for different particle species are used to fit the following empirical formula, the so-called "universal" curve:

$$\frac{dE}{dx} = \frac{c_1 \log \frac{\beta\gamma}{\beta\gamma+b} + c_0}{\beta^2} + a_1(\beta-1) + a_2(\beta-1)^2 \tag{3.4}$$

where c_0, c_1, b, a_1 and a_2 are derived from the fit to data. From this curve, the predicted dE/dx can be calculated for different particles at a given momentum [5].

Samples of $\Lambda \to p\pi$ and $K_s \to \pi\pi$ from the μ+SVT data were used to study proton identification in Λ_b lifetime measurement. A mass spectrum of Λ and K_s candidates are shown in Figure 3.10. An interesting plot of the comparison of the Λ

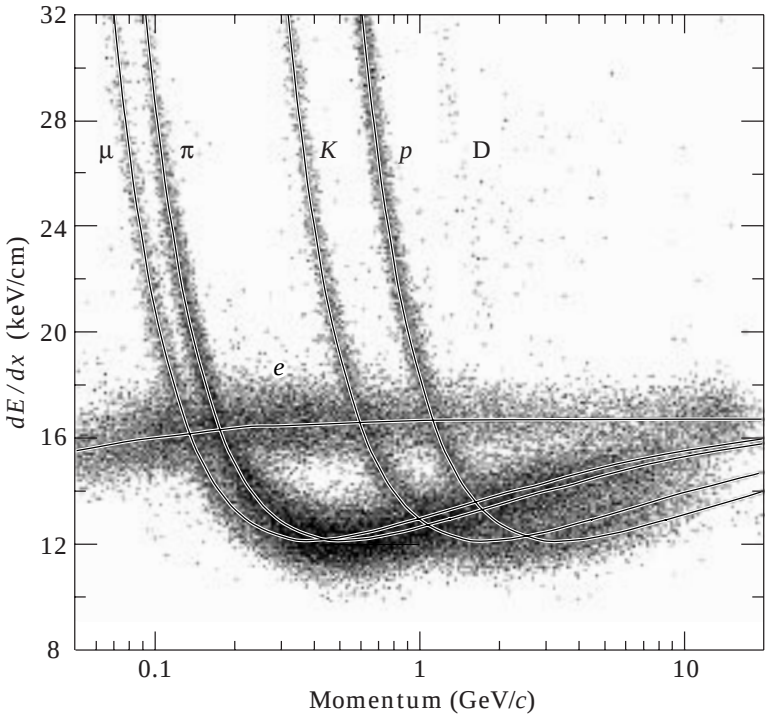

Figure 3.8: dE/dx separation power from PDG [7].

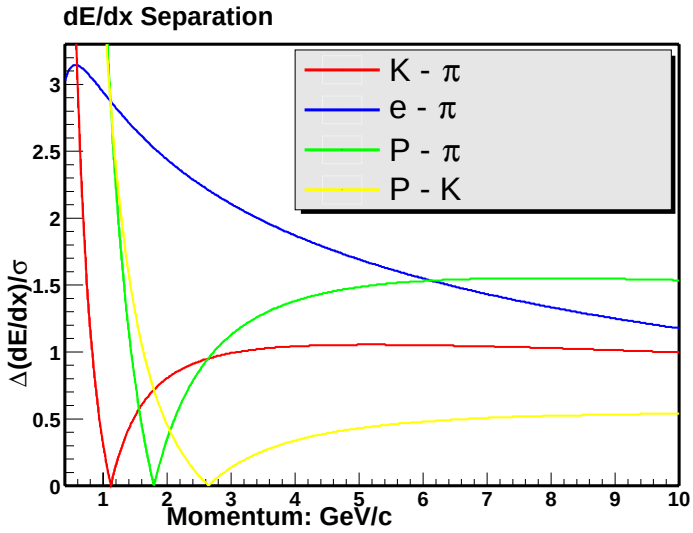

Figure 3.9: Ideal dE/dx separation power at CDF.

mass spectrum with the average dE/dx for the corresponding mass bins is shown in Figure 3.11. The Λ mass distribution can be interpreted in another way: in the mass peak region, the proton is at its highest purity; away from the mass peak, the proton purity decreases, and in the sideband region, the proton purity is close to zero. Since proton dE/dx is lower than pion dE/dx for $p_T > 2GeV$, for Λ mass distribution, most background is from pion/proton misidentification. So the averaged dE/dx vs Λ mass reflects the proton purity as a function of the $p\pi$ mass. This directly shows that proton can be selected over pions by using dE/dx.

The original dE/dx calibration is based on sample from another trigger [5]. In order to use dE/dx more properly in the μ+SVT sample, a small modification to the predicted proton and pion dE/dx was made by looking at the difference between proton/pion dE/dx and the predicted proton/pion dE/dx in the Λ and K_s samples. The observed results of the small modification are shown in Figure 3.12. The proton/pion dE/dx pull distribution after modification are shown in Figure 3.13 where the pull distribution is defined as $(dE/dx(p/\pi) - dE/dx(p/\pi)_{predicted})/\sigma_{dE/dx(p/\pi)}$. Two gaussians were used to fit the pull distribution, and the central values returned from the narrow gaussian(90 percent fraction) were 0.015(proton) and -0.045(pion), the sigmas were 0.84(proton) and 0.85(pion), and the dE/dx uncertainty was rescaled by a factor of 0.84.

3.3.2 TOF

CDF II added a new TOF detector into the detector system. The TOF information provided by the TOF detector can be used for particle identification. Actually, TOF and dE/dx are complementary, so combining them together can provide good particle identification power. The TOF is measured by the time of arrival of a particle at the scintillator with respect to the collision time. One way to do TOF particle identification is to calculate the TOF mass by:

$$m = \frac{p}{c}\sqrt{\frac{c^2t^2}{L^2} - 1} \tag{3.5}$$

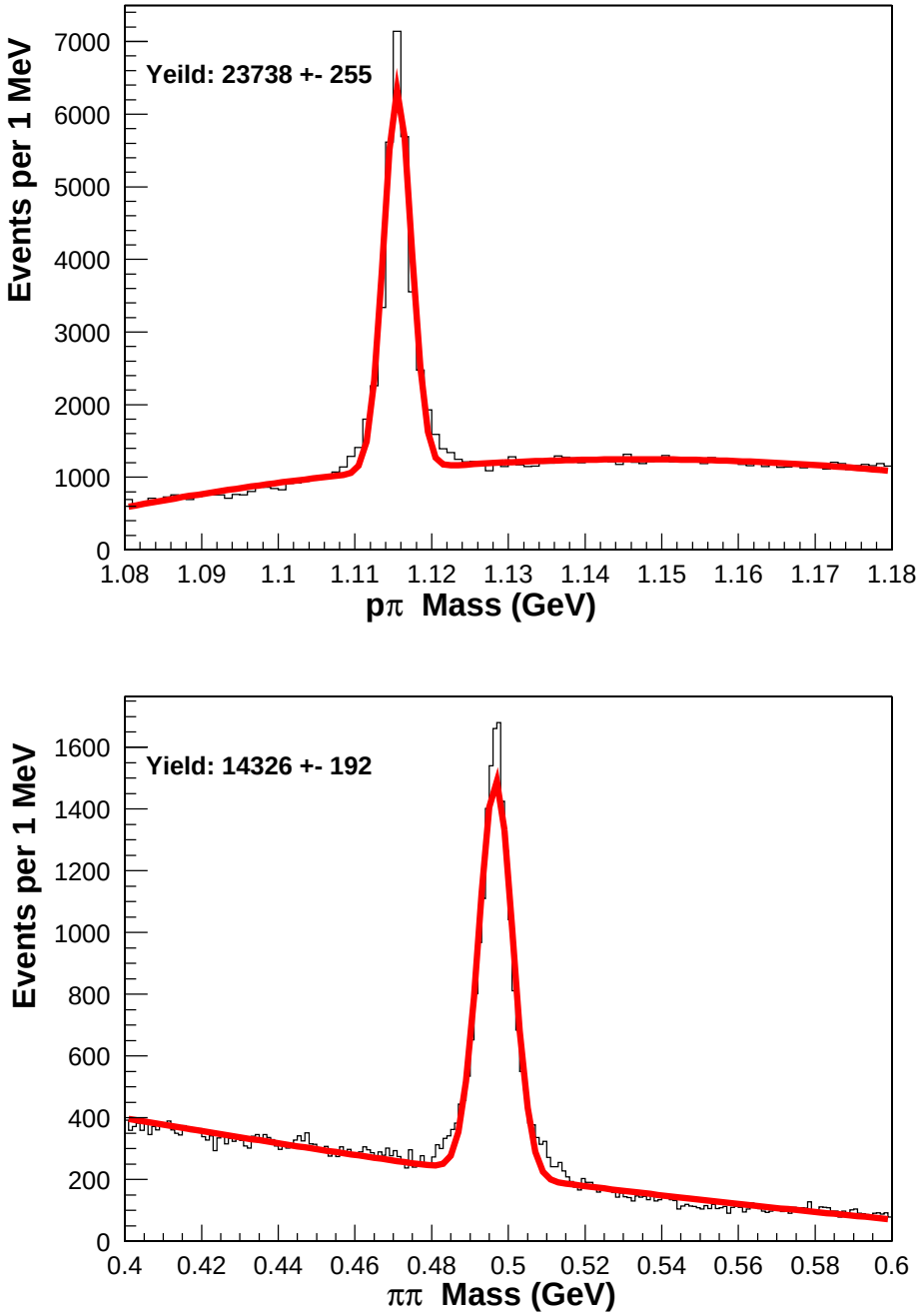

Figure 3.10: The $p\pi$ and $\pi\pi$ mass distribution.

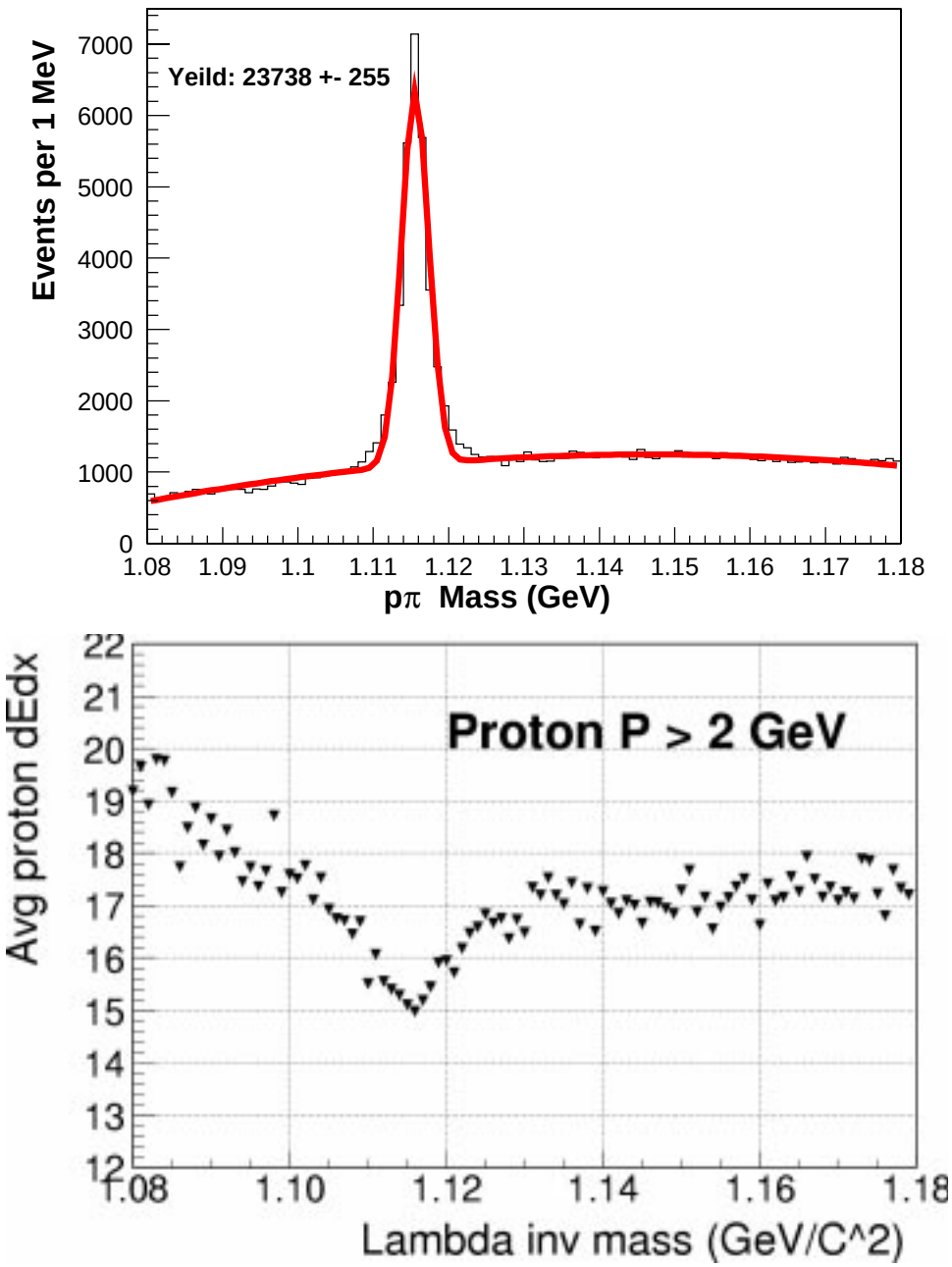

Figure 3.11: The $p\pi$ mass distribution and the average dE/dx for corresponding mass bin.

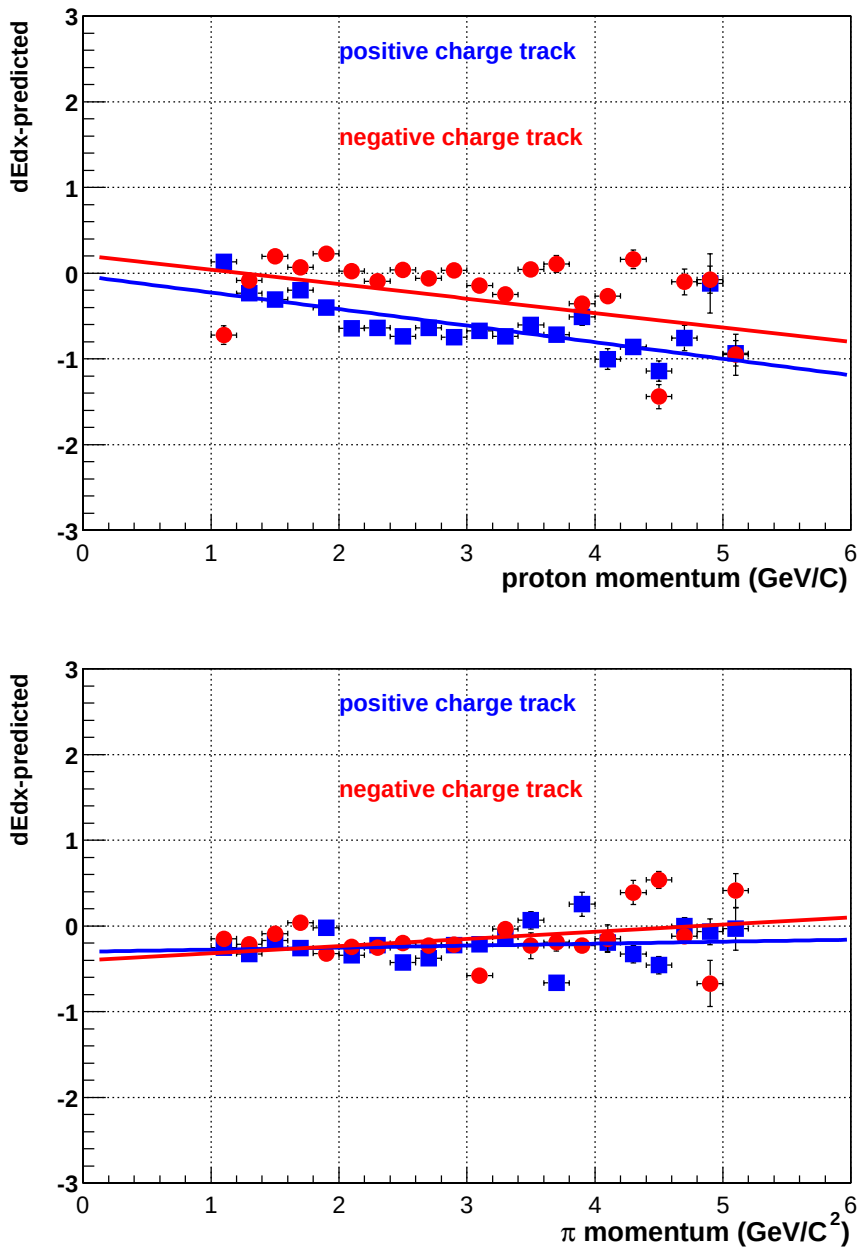

Figure 3.12: Top: the difference between proton dE/dx and predicted proton dE/dx in the Λ sample. Bottom: the difference between proton dE/dx and predicted proton dE/dx in the K_s sample.

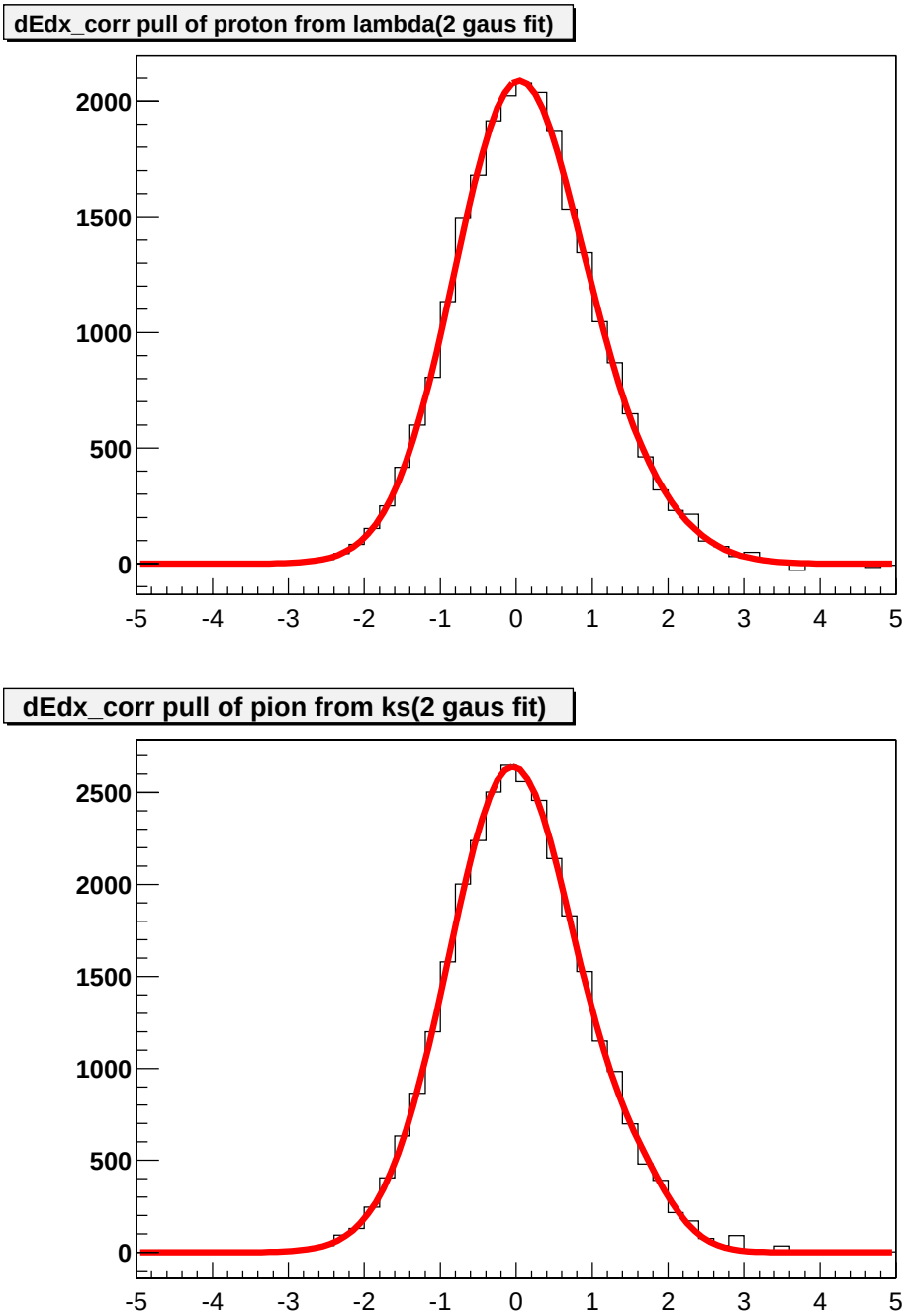

Figure 3.13: The dE/dx pull distribution after the modification for proton(top) and pion(bottom).

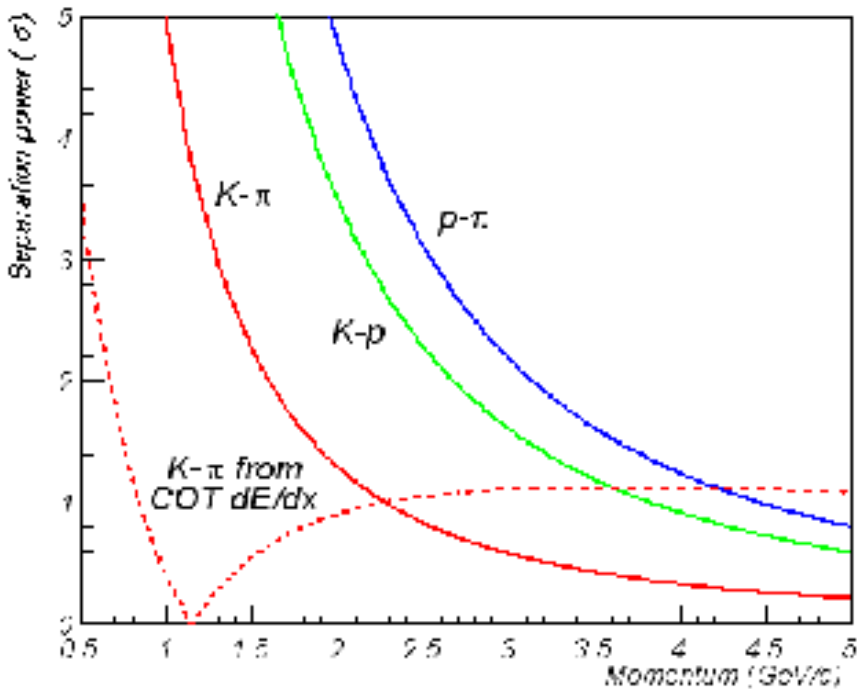

Figure 3.14: TOF separation power

where p is the particle momentum, L is the particle path length measured by tracking system, and t is the particle time-of-flight measured by TOF detector. Assuming a TOF resolution of 100 ps the expected particle separation power from the time-of-flight difference as a function of momentum is shown in Figure 3.14.

The pull distribution of proton/pion TOF from Λ and K_s are shown in Figure 3.15. However, since Λ and K_s are long lived particles they travel a long distance from primary vertex before they decay, and the TOF reconstruction assumed that they have come from primary vertex , so the pull distribution is not a perfect gaussian. However in the Λ_b semeleptonic decay situation, because of the short lifetime of Λ_b and Λ_c(hundred μm order), the TOF information attached on the proton track does not have the vertex effect.

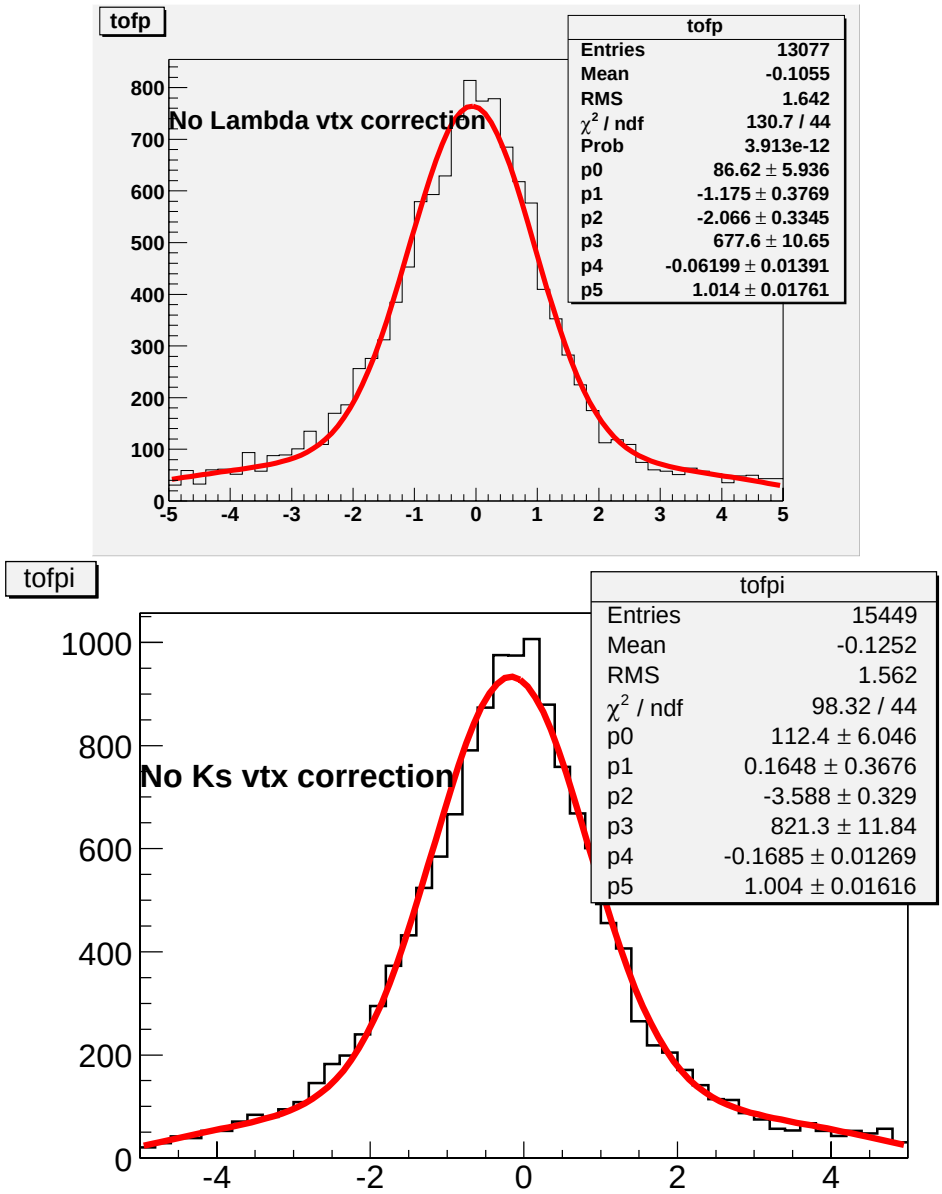

Figure 3.15: TOF pull distribution for proton(top) and pion(bottom).

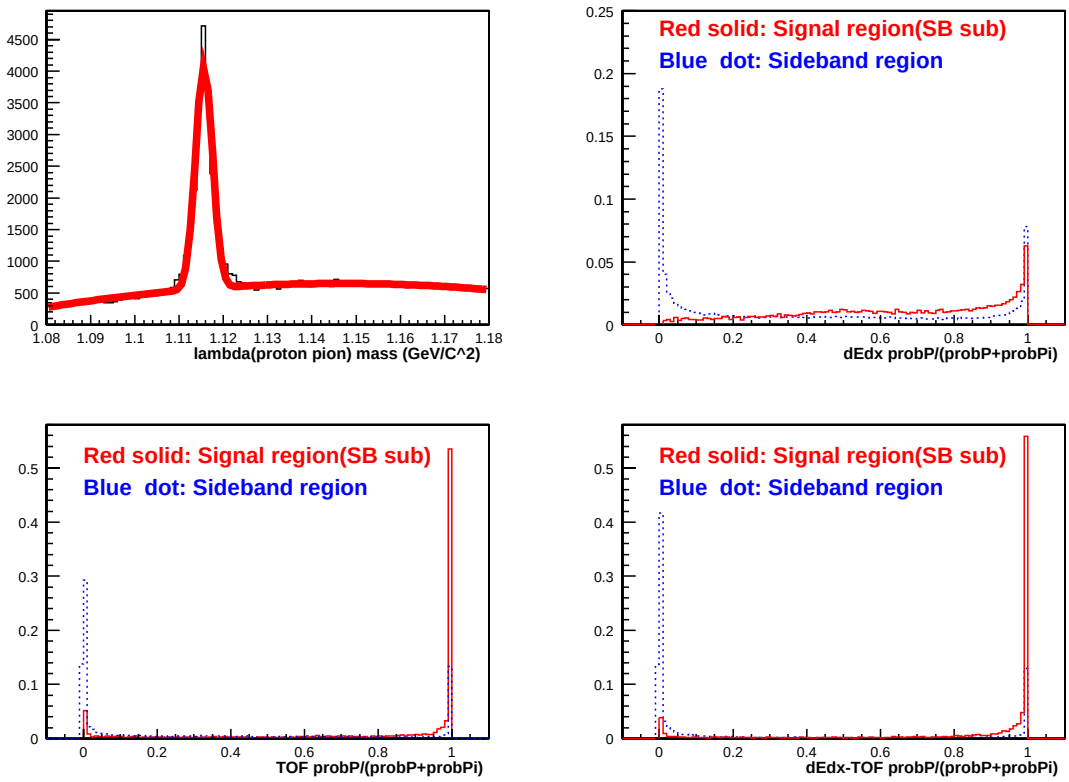

Figure 3.16: $p\pi$ invariant mass and likelihood ratio distribution. The left top is the $p\pi$ invariant mass distribution of candidates used to demonstrate the proton likelihood ratio distribution. From the right top to the right bottom are the real proton(in the Λ mass window of [1.112,1.12], sideband subtracted) and fake proton(sideband in the Λ mass window of [x,y]) likelihood ratio distribution in the cases of TOF/dE/dx both being used,only TOF being used,only dE/dx being used to calculate the probability, respectively.

3.3.3 Combined dE/dx and TOF Performance

For each proton candidate track, we calculate the upper tail probability of Chi-Squared distribution per degree of freedom for both $p\&\pi$ hypotheses, so called p-value, for a given χ^2 value X using :

$$Prob(p,\pi) = \frac{1}{\sqrt{(2^N)}\Gamma(\frac{1}{2}N)} \int_X^\infty e^{-\frac{1}{2}t} t^{\frac{1}{2}N-1} dt \tag{3.6}$$

where N is the number of devices(TOF,dE/dx) we used to calculate the X, and X is defined as:

$$X = \sum_{i=TOF,dE/dx} \frac{(X_i - X_{i-predicted})^2}{\sigma^2_{Xi}} \tag{3.7}$$

From these p-values, we calculate a particle identification ratio :

$$Ratio(p) = \frac{Prob(p)}{Prob(p) + Prob(\pi)}. \tag{3.8}$$

Real protons have a $Ratio(p)$ distribution peaking at 1 while fake protons have a distribution peaking at zero. The probability distributions of this ratio in cases where only dE/dx is used, or only TOF is used, or both dE/dx and TOF together are used are shown in Fig 3.16. We choose $prob(p) > 0.0027$ which corresponds to a 3σ cut for one degree of freedom and $Ratio(p) > 0.5$ as the proton identification cut. Applying this proton identification cut to the Λ sample for TOF only, dE/dx only and TOF dE/dx together, we see the power of CDF II particle identification. The Λ mass spectrum and K_s reflection inside the Λ mass window for TOF-dE/dx / TOF / dE/dx are shown in Fig 3.17, 3.18, 3.19 respectively. For the best case of TOF and dE/dx both being used for the proton identification, the Λ signal-to-background(S/B) ratio is increased from 2.4 to 8.3. Almost all candidates from the K_s reflection are excluded, while the overall efficiency of $\sim 77\%$ is maintained. For the case of only TOF being used to identify protons, it can increase the S/B ratio from 2.4 to 6.1, and for the case of only dE/dx being used to identify protons, it can increase the S/B ratio from 2.2 to 4.2. We also measured the proton particle identification efficiency by fitting the Λ mass spectrum before and after applying proton particle identification. The efficiency curves as a function of proton p_T for TOF+dE/dx and dE/dx are shown

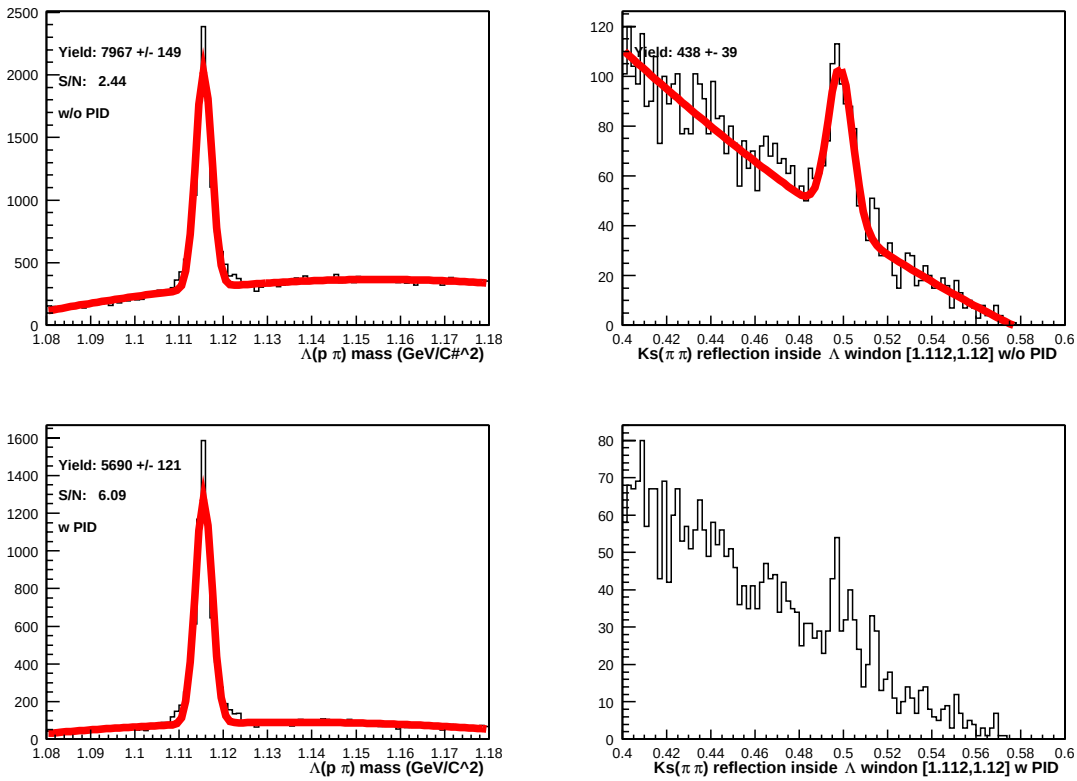

Figure 3.17: Top left: Λ mass distribution without proton identification. Top right: K_s reflection by assign pion mass to the proton inside the Λ mass window without proton identification. Bottom left: Λ mass distribution with proton identification (TOF only). Bottom right: K_s reflection by assigning pion mass to the proton inside the Λ mass window with proton identification.

in Fig 3.20. In Fig 3.21 the invariant mass of $pK\pi$ in about 60 pb^{-1} lepton+SVT sample before and after proton identification application while keeping all other cuts the same are shown. This identification reduces the background by a factor of 4$\sim$5 while keeping about $\sim 60 - 70\%$ of the signal events.

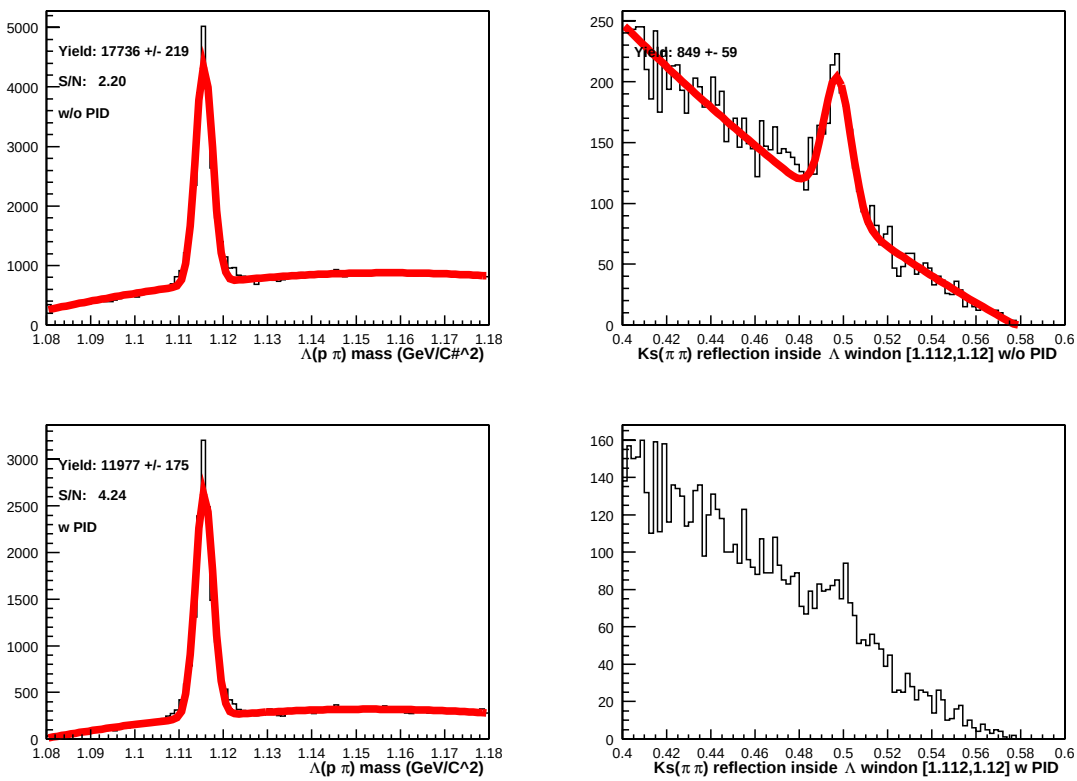

Figure 3.18: Top left: Λ mass distribution without proton identification. Top right: K_s reflection by assign pion mass to the proton inside the Λ mass window without proton identification. Bottom left: Λ mass distribution with proton identification (dE/dx only). Bottom right: K_s reflection by assign pion mass to the proton inside the Λ mass window with proton identification.

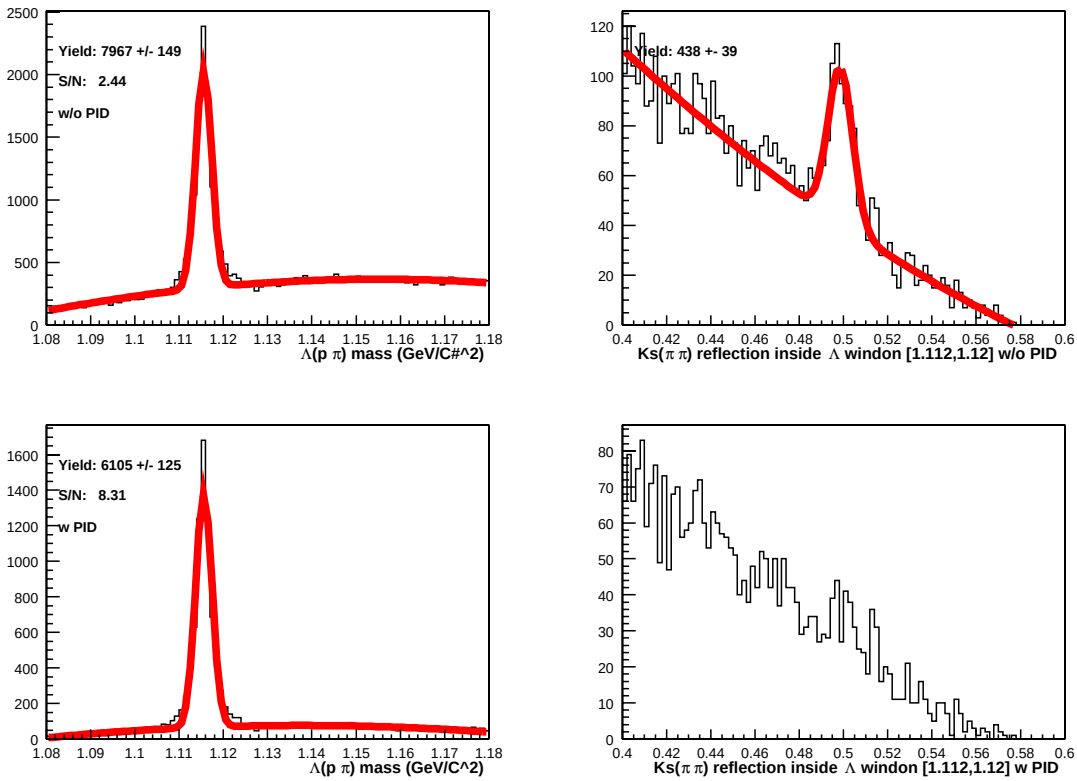

Figure 3.19: Top left: Λ mass distribution without proton identification. Top right: K_s reflection by assign pion mass to the proton mass inside Λ mass window without proton identification. Bottom left: Λ mass distribution with proton identification (TOF+dE/dx). Bottom right: K_s reflection by assign pion mass to the proton inside the Λ mass window with proton identification.

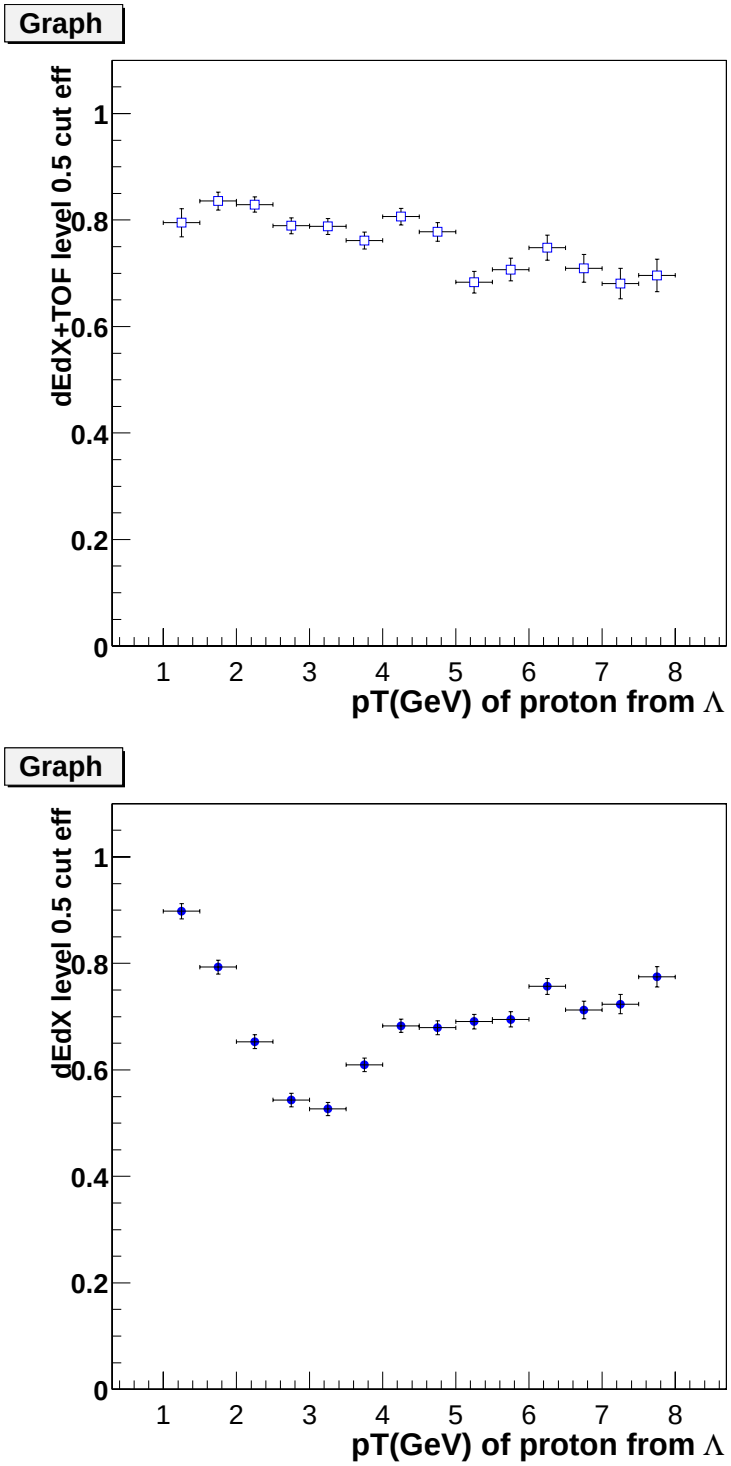

Figure 3.20: Proton identification efficiency as a function of proton p_T. Top: TOF and dE/dx are both used for proton identification, bottom: only dE/dx is used for proton identification.

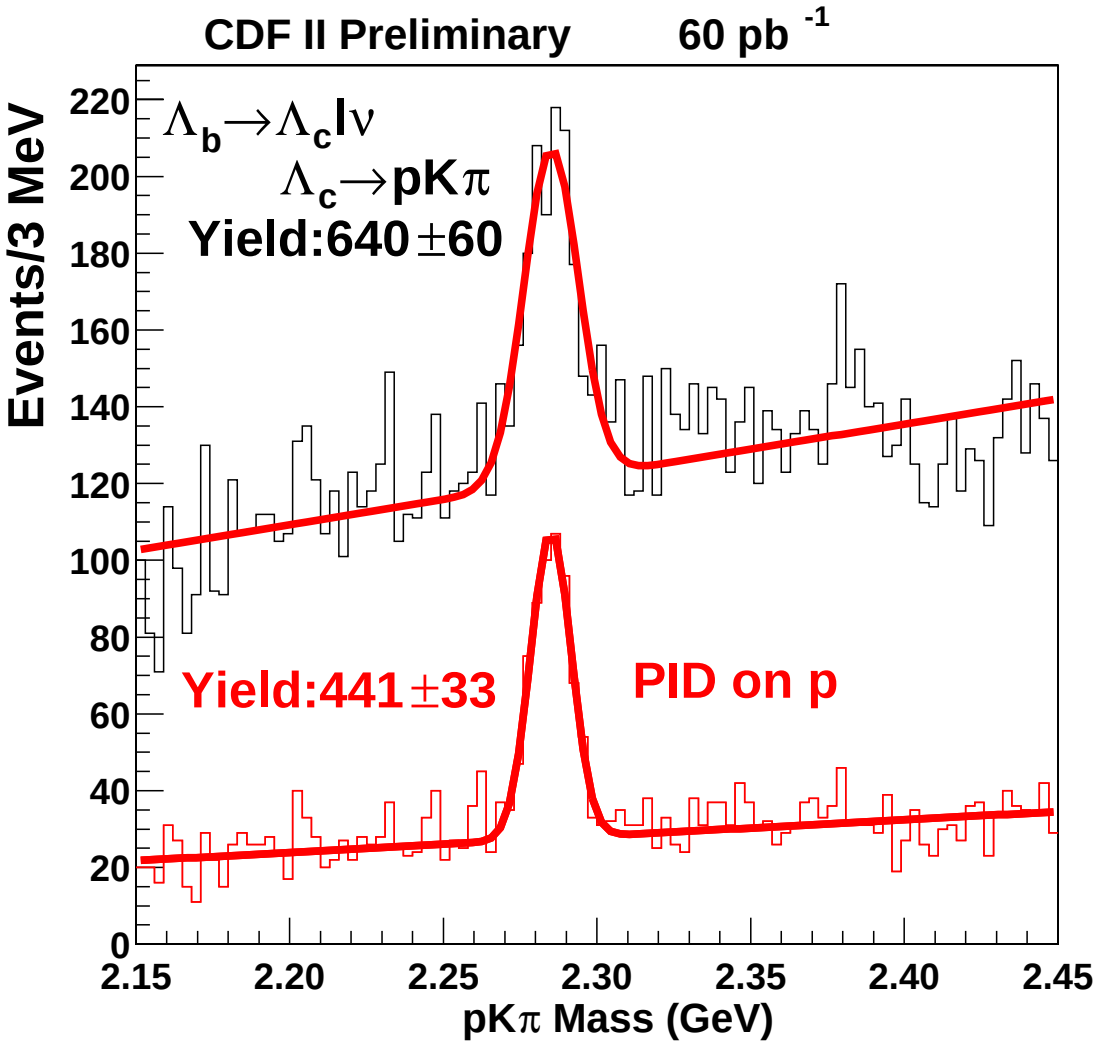

Figure 3.21: $pK\pi$ invariant mass from Λ_b without(top) proton identification and with(bottom) proton identification.

Bibliography

[1] N. Solomey, A.B. Wicklund, CDF 247(1984)

[2] H.-C. Fang et al, CDF/DOC/BOTTOM/CDFR/6326.

[3] H.-C. Fang, CDF/DOC/BOTTOM/CDFR/5910.

[4] W. Blum, L. Rolandi. PArticle Detection with Drift Chambers. Spring Verlag.

[5] Shin-Shan Yu et al, CDF/DOC/BOTTOM/PUBLIC/6361.

Chapter 4

Event Reconstruction for Λ_b

At CDF in Run II, the total cross section, $c\bar{c}$ cross section, and $b\bar{b}$ cross section are estimated to be about 75 mb, 1 mb, 100 μb [1]. The $b\bar{b}$ cross section is quite large compared to 1 nb for $b\bar{b}$ in e^+e^- collisions at $\Upsilon(4S)$, and 6 nb at Z pole [2]. With a total luminosity of about 70 pb^{-1}, which is used in the Λ_b lifetime measurement, about 7×10^9 $b\bar{b}$ events were produced at CDF. This is a huge advantage in studying B physics at Tevatron. However, due to the large total cross section, $\sim$ 75 mb–3 orders of magnitude higher than the $b\bar{b}$ cross section, it is a big challenge to select B events from the huge background. Fortunately, the b quark has a longer lifetime($c\tau \sim= 450\mu m$) compared to other particles, so the key point to distinguish b events is to find the displaced vertex caused by B hadrons. This requires good vertex resolution, and the CDF silicon detector plays a very important role for this.

The signature of $\Lambda_b \rightarrow \ell^+\Lambda_c^-\bar{\nu}_\ell$ is an identified lepton(e, μ), a reconstructed Λ_c, the charge correlation between the lepton and Λ_c, the displaced vertex formed by the lepton and the Λ_c, and the invariant mass of lepton and the Λ_c. In the Λ_b lifetime measurement, the Λ_c was reconstructed by its decay channel pKπ. The three stable particles form a Λ_c vertex which is a little bit displaced from the Λ_b vertex because of the short lifetime of the Λ_c, $\sim$ 60 μm. Since the radius of the beampipe is about 1.5 cm, both the Λ_c and Λ_b vertices are inside the beampipe, and thus also inside the silicon detector. The good vertex resolution provided by silicon detector is important for purifying the signal.

4.1 Data Sample and code version

The Lepton+SVT samples used in the Λ_b lifetime analysis from Run II were collected by the CDF detector from Jan. 2002 to Jan. 2003 and processed with CDF software version 4.8.4 [2]. Data from run numbers 138425 to 156484 are used, which corresponds to about $70pb^{-1}$ luminosity for runs with SVX II operational. The validated CDF software version 4.9.1hpt2 is used for the Λ_b event reconstruction.

4.2 Track Reconstruction

CDF charged track reconstruction starts from the COT. When a charged particle goes through the COT chamber, the wires inside the COT will collect the ionization charge caused by the charged particle. From the measured drift time(t) and the constant drift velocity(v), the actual hit position can be calculated by:

$$x = x_w \pm tv \tag{4.1}$$

in an ideal drift chamber. In reality, due to some nonuniformities and nonlinearities, various corrections need to be done [3]. For example, the "$\pm$" ambiguity, it is due to the fact that the particle can pass one single wire's left side or right side and provide identical timing information, and this can not be resolved by a single wire. This ambiguity will be resolved by track finding from multilayer hits. The first step is to search for track segments inside each superlayer. For three consecutive layers i, $i+1$, $i+2$, if all the three layers have hits, it first calculates all the slope α with respect to the radial direction by looping over the drift signs($\pm$) in layer i and layer $i+2$, the each cell. There is a calculated limit on α. For each combination which passed the limit cut, they are sorted in order of increasing slope in order to improve the chance of finding high p_T tracks early. Then for each passed sign combination in layer i and layer $i+2$, it searches hits in layer $i+1$ along its road, if a hit is within its search window, this hit will be added to this combination. For each combination where three hits have been found, it will fit a line to it and then extend this line through the superlayer. Each hit on wire i is allowed to generate at most one line segment.

If more than one is generated, the one with most hits is kept. By going through this process, track segments are found. After all the segments have been found two COT track algorithms are run at the same time: segment linking which was used at Run I and histogram linking which was developed for Run II [4]. The segment link algorithm starts linking from the outmost layer: first axial linking and then stereo linking. The axial segment linking is based on the simple geometrical property of the segments that they belong to the same track: considering two segments as a straight line, they form two equal angles with the line which connects their central points. Once the axial segment linking is done, stereo linking begins by determining which stereo superlayers should be considered. Those superlayers which the axial track does not intersect are immediately discarded. The axial track will pick up the stereo hits and refit the track with the picked stereo hits.

On the other hand, histogram linking starts from the outer layer segment, by constraining the segment to the beam position, forms a "telescope", which means it forms a path from the outlayer segment to the beam position. The track curvature D was chosen to be be varied, that is to say, fix the other track parameters to describe the telescope, but the track curvature can be shifted by a distance. To speed up the process, a search window was set when to use the telescope to scan the inner layers to pick up hits. At this point, a log-likelihood is calculated as a function of D for each hit and this is filled into a histogram for each layer. All the histograms in different layers will be summed together afterwards. Ideally, all the contribution due to the hits that belong to the telescope track should have the same D and this results in a sharp peak in the sum histogram. Then a set of hits is assigned to this telescope track by looking at the sum histogram and refitting the track. Finally, the tracks found by segment linking and histogram linking will be merged together and COT pattern recognition process is done [4].

In the central region, silicon tracking is based on COT tracking and has two algorithms: Outside-In (OI) and the so-called OIZ tracking which follows the same algorithm as OI but also uses the stereo information from the silicon detector (i.e the "z" side). Based on the COT track, the track error matrix is used to establish a road size in $r\phi$, the silicon hits in the outmost layer were scanned and determined if they

belong to this track. If so, the track was refit with silicon hits found in this layer. Based on the newly refitted track information the above process is repeated until the innermost of the silicon detector is reached. At the end of this process, there may be more than one track candidate associated with the original COT track. In this case, the candidate that has hits in the largest number of silicon layers is chosen as the best candidate or one chooses the best χ^2 of the track fit if more than one track candidate have the same number of hits.

OIZ tracking is a silicon tracking algorithm which is very similar to OI tracking. It starts from an OI track but takes the original COT track and the set of $r\phi$ hits found by OI tracking, extrapolates the track into the silicon detector by adding stereo (90 degree and small angle silicon hits) and $r\phi$ hits into the track via a progressive fit similar to OI track [5].

Outside of the central region, there is no COT track that can be used as a seed, so a tracking algorithm called StandardAlone is used to reconstruct the track in the silicon detector. In the Λ_b lifetime measurement, StandardAlone tracks are not used for event reconstruction.

4.3 Beam Position and Alignment

For lifetime measurement, we need to know the beam position where we assume b hadrons were produced, then we can calculate the decay length from beam position and the reconstructed secondary vertex. The average beam position is calculated run by run at CDF. By running a vertex finder tool called vxprim for each event, a series of vertices will be found, and we get the beamline from this information.

For a precision measurement like the b hadron lifetime, the silicon detector alignment is very important because misalignments between the silicon ladders after the rough alignment before assembly on the barrel can be in the order of 10 μm magnitude. For high statistics b hadrons sample, this is not negligible. A detailed alignment and its performance can be found in [6].

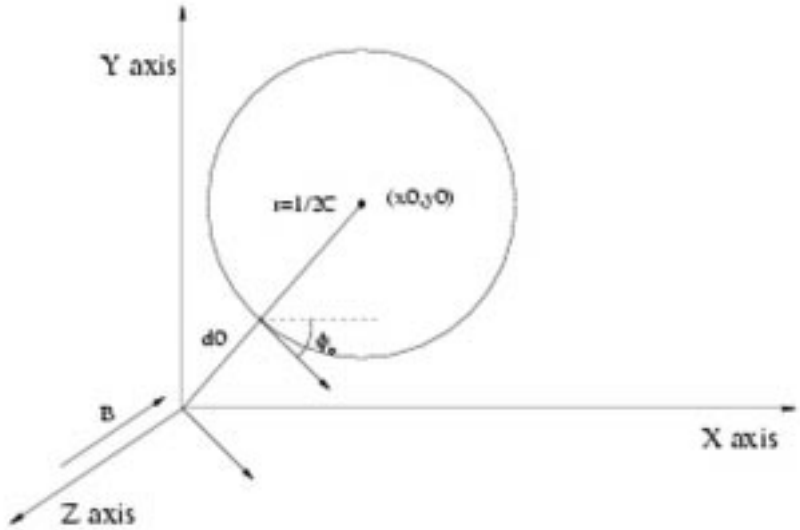

Figure 4.1: The five helix parameters describe a track.

4.4 Vertexing

At CDF, a track trajectory is described by the following five helix parameters: $(\cot\theta, c, z_0, d_0, \phi_0)$, and they are shown in Figure 4.1. Mathematically, the trajectory of a track is defined by the following equations:

$$x = r\sin\phi - (r + d_0)\sin\phi_0 \tag{4.2}$$

$$y = -r\cos\phi + (r + d_0)\cos\phi_0 \tag{4.3}$$

$$z = z_0 + s\lambda \tag{4.4}$$

where $\lambda = \cot\theta = p_Z/p_T$, $p_T = 0.149896B/c$, r=1/2c, $\phi = \phi(s) = s/r + \phi_0 = 2cs + \phi_0$, s is the projected length along the track, and B is the magnetic field (Tesla). Any point passed through by the track will satisfy the above equations. They can be solved for s, d_0, and z_0 as:

$$s = \frac{1}{2c}\sin^{-1}[2c(x\cos\phi_0 + y\sin\phi_0)] \tag{4.5}$$

$$d_0 = y\cos\phi_0 - x\sin\phi_0 - \frac{1}{c}\sin^2 cs \tag{4.6}$$

$$z_0 = z - \lambda s \tag{4.7}$$

At CDF, we use a module which is called VertexFit to find secondary vertices. For some given tracks, VertexFit finds a vertex point (x_s, y_s, z_s) and fitted track parameters for each track which satisfy the equations 4.5 through 4.7 by varying the track parameters within measurement errors for each track. The desired track parameters are the ones that have the least χ^2, which is defined as:

$$\chi^2 = \sum_{i=1}^{N} \xi_i^t G_i^{-1} \xi_i \tag{4.8}$$

where

$$\xi_i = \begin{bmatrix} \Delta c_i \\ \Delta\phi_i \\ \Delta\lambda_i \\ \Delta d_i \\ \Delta z_i \end{bmatrix} = \begin{bmatrix} c_i - c_{i0} \\ \phi_i - \phi_{i0} \\ \lambda_i - \lambda_{i0} \\ d_i - d_{i0} \\ z_i - z_{i0} \end{bmatrix} \tag{4.9}$$

and where Δs are the differences between track parameters constrained by Equations 4.5 to 4.7 and the measured (unconstrained) parameters (subscript 0). G is the 5×5 error matrix of the measured parameters. By varying the ξ variables to minimize the χ^2 one find the secondary vertex (x_s, y_s, z_s).

4.5 Background for $\Lambda_b \to \ell^+\Lambda_c^-\nu$

The largest background sources come from the combinatorial background and reflections from other charm hadrons. The combinatorial background comes from random association of any three tracks in the events that pass the kinematic cuts. This background forms most of the wrong-sign mass distribution and it will also get into the right-sign mass distribution. Other charm hadrons like $D^+ \to \pi^+K^-\pi^+$, $D_s^+ \to K^+K^-\pi^+$, $D^{*+} \to D^0\pi^+, D^0 \to K^-\pi^+$ etc have the same topology as $\Lambda_c^+ \to pK^-\pi^+$. The above statement assumes that there is no any particle identification. However, for the above charm hadron reflections, there is no proton in the event

decay, and most tracks in a event are pions, so these backgrounds can be significantly reduced by identifying a proton track from pions tracks. This can also significantly reduces the combinatorial background because by requiring a proton track for one of the three tracks significantly reduces the possible combinations.

The possible b hadron decays which can generate a true Λ_C and lepton in the final state are: $\Lambda_b^0 \to \Lambda_c^+ D_s^- X$ where $D_s^- \to \ell^- X'$, $B^0 \to \Lambda_c^+ D_s^- X$ where $D_s^- \to \ell^- X'$, $B^0 \to \Lambda_c^+ \ell^- \bar{\nu} X$, $b\bar{b}$ and $c\bar{c}$ pairs due to gluon splitting, and $\Lambda_b \to \Lambda_c^{*+} \ell^- \bar{\nu}$ where $\Lambda_c^{*+} \to \Lambda_c \pi^+ \pi^-$. The effects of the first four channels have been studied and found to be small in ref [7]. In the case of $\Lambda_b \to \Lambda_c^+ D_s^- X$ where $D_s^- \to \ell^- X'$ is suppressed by D_s semileptonic decay branching ratio. There is no significant contribution for $B^0 \to \Lambda_c^+ D_s^- X$ where $D_s^- \to \ell^- X'$ to the Λ_b signal because of the small $\ell\Lambda_c$ invariant mass due to another baryon in X (the baryon antibaryon are produced in pair). $\Lambda_b \to \Lambda_c^{*+} \ell^- \bar{\nu}$ is suppressed by its branching ratio and it is further suppressed by increasing the $\ell\Lambda_c$ invariant mass due to the additional pions from the $\Lambda_c^* \to \Lambda_c \pi^+ \pi^-$ decays in the final state. In the gluon splitting case, if a $b\bar{b}$ is produced, the two quarks are are close and therefore might produce an electron from one b and a Λ_c from the other. However, if the the lepton comes from the opposite b quark decay, the process produces wrong charge combination lepton-Λ_c pairs, of which none are seen in data. If the lepton comes from the opposite charm decays, it produces a right-sign pair, but it is suppressed by its softer p_T spectrum and the charm semileptonic decay branching ratio. If we assume that the branching fraction of $b \to c\ell$ is roughly the same as $c \to d\ell$ and b 100% goes to c, then the right-sign yield of this process is about the same as the wrong-sign yield resulting from another b direct semileptonic decay. Since no wrong-sign pairs are observed, the contribution from gluon $b\bar{b}$ pairs is negligible. In the case of gluon splitting to a $c\bar{c}$ pair, the Λ_c and lepton must come from different c quark of the pair and does generate a right-sign pair. Due to the statistics limitation, it is not possible to study it in this channel. However, from run I lepton+charm sample study, the contribution from $g \to c\bar{c}$ is less than 1.9% [8]. For the $\Lambda_b \to \Lambda_c^{*+} \ell^- \bar{\nu}$ where $\Lambda_c^{*+} \to \Lambda_c \pi^+ \pi^-$ case, the invariant mass of $\ell + \Lambda_c$ tends to be low due to the fact that the reconstruction of $\Lambda_b \to \Lambda_c^{*+} \ell^- \bar{\nu}$ loses two more pions. We increase the invariant mass cut from the kinematic limit(mass of Λ_c) to 3.5 GeV/c^2

and the p_T of $\ell + \Lambda_c$ to be greater than 9 GeV to further suppress the background. To further monitor other sources of background which produce same amount of signal in the right-sign and wrong-sign mass distribution, we monitor the wrong-sign mass distribution and find no events.

4.6 $\Lambda_b \to \Lambda_c^+ \ell^- \nu$ Signal

We search for the decay $\Lambda_b \to \Lambda_c^+ \ell^- \nu$ [9] by requiring a $\Lambda_c^+ \ell$ (right sign) pair with invariant mass in the kinematically allowed range $m_{\Lambda_c} < m_{\Lambda_c \ell} < m_{\Lambda_b}$.

We first require that the electron and muon pass the default selection criteria as defined in SemiLeptonicB module. For the electron, the Hadem cut is tightened to be less than 0.05 and the E/P cut is tightened to be $0.5 < E/P < 1.5$. Photon conversion electrons are removed if $|s| < 0.2cm$ and $\Delta cot\Theta < 0.03$. Lepton candidates are required to have a minimum transverse momentum of 4 GeV/c. Muons are required to have hits in both CMU and CMP chambers to reduce background from hadron punch-through. The χ^2 of the position match between tracks segments in the muon chambers (CMU and CMP) and an extrapolated track is required to be less than 9 in the transverse plane. Lepton tracks are required to have $r\phi$ SVX hits in at least 3 out of the total of 5 SVX layers, and also require the number of hits on COT axial/stereo wires be greater than 24, the number of superlayers of COT axial/stereo wires be greater than 2, and the number of hits on 1 COT axial/stereo superlayer be greater than 6. We further require the total number of layers which have $r\phi$ SVX hits to be greater than or equal to one less than the number of integrated SVX layers. To reduce the background further, we require the excess transverse energy $(E^{iso})_t$ inside a 0.4 cone in $\eta - \phi$ around the lepton be roughly the same as the transverse momentum of Λ_c, i.e., $E_t^{iso}/p_t(\Lambda_c) < 1.2$.

The charmed baryon Λ_c^+ is reconstructed through its decay to $pK^-\pi^+$. All three tracks have the same SVX hits requirement as the lepton, and they are required to be within a cone of $R = \sqrt{\Delta\eta^2 + \Delta\phi^2} < 1.2$ around the lepton. The four tracks are required to be separated by less than 5 cm in the rz view. The minimum transverse momentum required for the proton, kaon and pion are 1.0 GeV/c, 0.5 GeV/c, and

0.5 GeV/c respectively. Since Λ_cs produced from B meson decays and from heavier b-baryon decays have much softer momenta (due to the existence of other particles to share the initial energy), we use only Λ_c^+ candidates with a transverse momentum of at least 5.0 GeV/c to reject those backgrounds. The high momentum cut also rejects combinatorial backgrounds. We used the VertexFit module (CTVMFT in Run I) to reconstruct the Λ_c and Λ_b candidate vertices. We reject combinations which do not have a successful fit and require $\chi^2_{r\phi}$ be less than 9 [1]. For each Λ_b candidate, the primary vertex is determined by the position of the SVX beamline (averaged over the whole run) [6] calculated at the z position of the lepton, z_0. The Λ_c vertex is required to have a positive projection along its momentum vector. We used SemiLeptonicB module [2] to confirm that one of the three Λ_c tracks be matched to an online-SVT track. Following standard procedure for the current tracking alignment, L00 and ISL silicon hits are dropped and KAL TrackRefitter is used to refit tracks [7] , and select events. Then we dropped 90 z and Stereo silicon hits to get the $c\tau$ distribution.

As discussed in chapter 3, for each proton candidate track, using (p, π) assumption, we calculate its upper tail probability of Chi-Squared distribution per degree of freedom (or p-value) for a given χ^2 value and from these p-values, we calculate a particle identification ratio :

$$Ratio(p) = \frac{Prob(p)}{Prob(p) + Prob(\pi)}. \tag{4.10}$$

Real protons have a $Ratio(p)$ distribution peaking at 1 while fake protons have a distribution peaking at zero. We choose $prob(p) > 0.0027$ which corresponds to a 3σ cut for one degree of freedom and $Ratio(p) > 0.5$ as the proton identification cut. As shown in Fig 3.21, this identification reduces the background by a factor of 4 while keeping most of the signal events.

After Λ_c^+ reconstruction, the Λ_c^+ candidate is combined with a negatively charged lepton. The $\Lambda_c^+\ell^-$ pair is required to satisfy the invariant mass cut $3.5 < m_{\Lambda_c^+\ell^-} < 5.6\ GeV/c^2$. Background $\Lambda_c^+\ell^-$ pairs produced from decay sources other than the $\Lambda_b \to \Lambda_c^+\ell^-\nu$ have softer momenta and smaller invariant masses [12]. We also require

[1] A Λ_c mass distribution in μ+SVT sample is shown in Fig 4.2, where we keep other cuts unchanged and require $\chi^2_{r\phi}$ be great than 9. No signal can be seen.

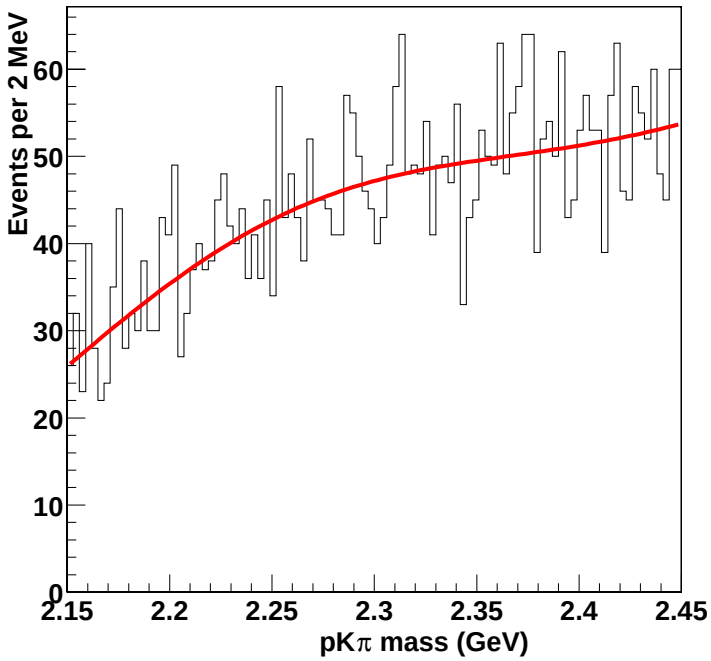

Figure 4.2: A $pK\pi$ mass distribution in μ+SVT sample, where we keep other cuts unchanged and require $\chi^2_{r\phi}$ be great than 9. No signal can be seen.

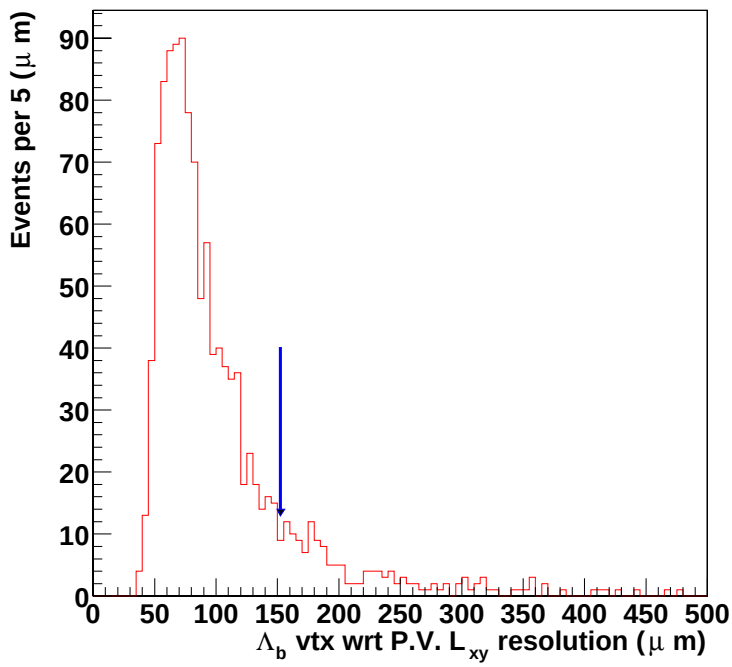

Figure 4.3: Λ_b Lxy resolution distribution.

the $L_{xy}(\Lambda_b)$ (which is defined as the distance between the Λ_b decay vertex and the production point along the $\ell^-\Lambda_c$ momentum direction) resolution to be less than 150 μm and $L_{xy}(\Lambda_c)$ with respect to primary vertex resolution to be less than 300 μm. The $L_{xy}(\Lambda_b)$ and $L_{xy}(\Lambda_c)$ resolution distributions are shown in Fig 4.3 and Fig 4.4. The Λ_b vertex is calculated from vertex information of the $\Lambda_c^+\ell^-$ pairs.

To determine the number of events passing our cuts, we fit the $pK^-\pi^+$ invariant mass distributions with proton particle identification, shown in Figure 4.5, where the distribution is fit with a function consisting of a Gaussian and a polynomial (n=2) background. The yield returned from the fit is 586$\pm$46. Figure 4.6 shows the $pK^-\pi^+$ invariant mass from the wrong sign sample, where no evidence of a signal can be seen.

The particle identification power is different between the two cases of a track having both TOF and dE/dx information and a track having only dE/dx information. The two cases can have a different background fraction and background $c\tau$ distribution shapes, so we treat them individually but add their log-likelihood together when we

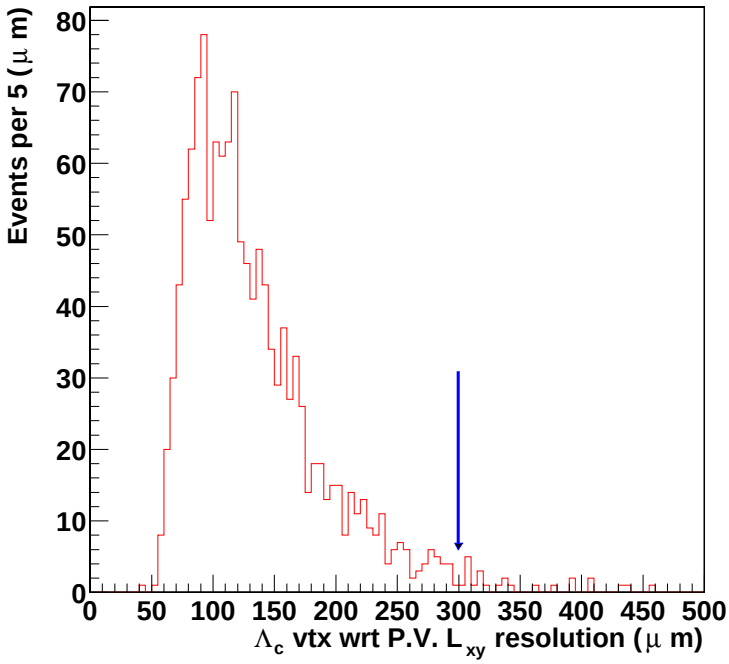

Figure 4.4: Λ_c Lxy with respect to primary vertex resolution distribution.

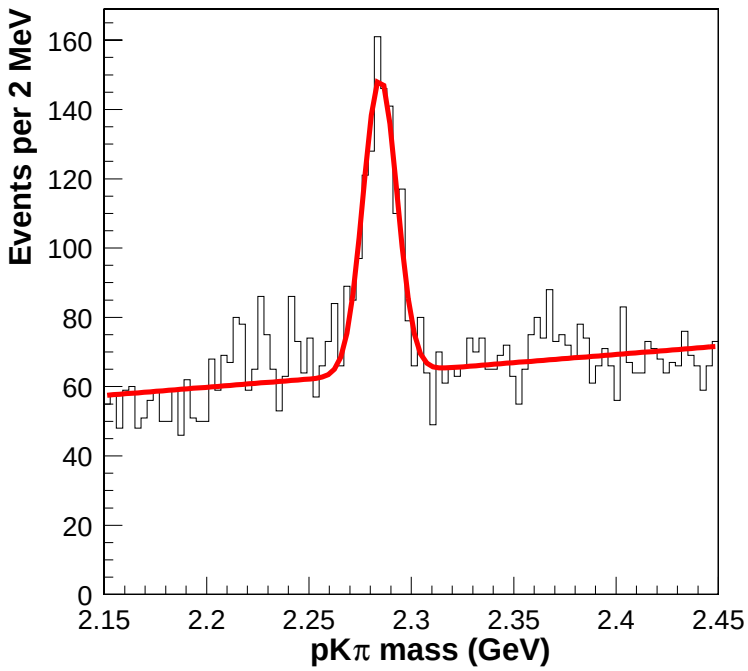

Figure 4.5: $pK\pi$ invariant mass for right sign events in lepton+SVT sample. The fit returns a yield of 586 ± 46 events.

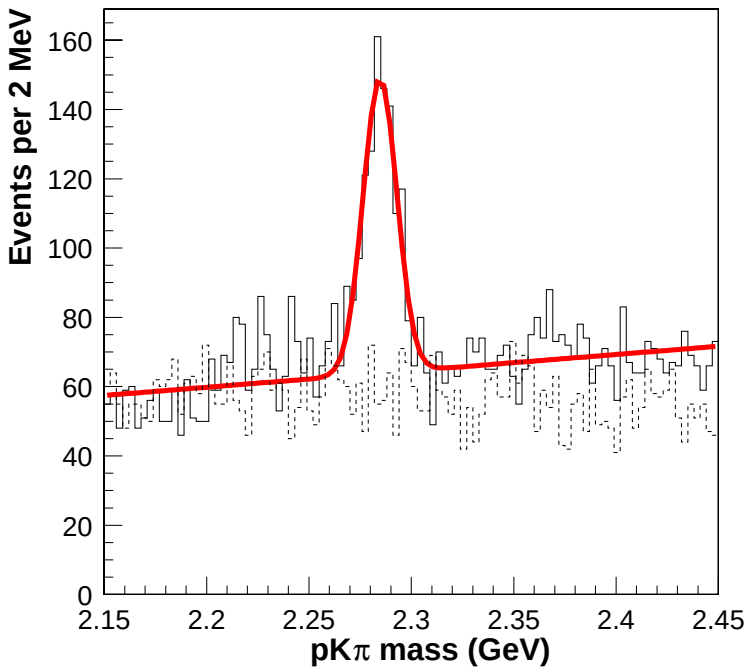

Figure 4.6: $pK\pi$ invariant mass for right sign(solid line) and wrong sign(dashed line) events in lepton+SVT sample. No signal can be attributed to the wrong sign sample.

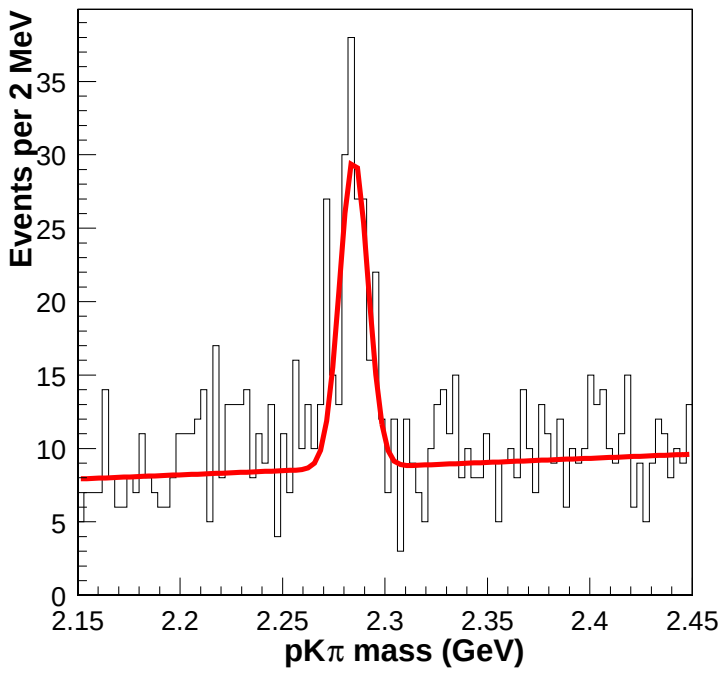

Figure 4.7: $pK\pi$ invariant mass in e+SVT sample where TOF and dE/dx are both required to identify the proton, proton likelihood ratio > 0.5.

fit the $c\tau$ distribution. Fig 4.9 shows the $pK^-\pi^+$ invariant mass from e+SVT sample where both TOF and dE/dx are used to identify the proton, and Fig 4.8 shows the $pK^-\pi^+$ invariant mass from e+SVT sample where only dE/dx is used to identify the proton. Fig 4.9 shows the $pK^-\pi^+$ invariant mass from μ+SVT sample where both TOF and dE/dx are used to identify the proton, and Fig 4.10 shows the $pK^-\pi^+$ invariant mass from μ+SVT sample where only dE/dx is used to identify the proton.

4.7 Λ_b Signal from 8 GeV sample

We also reconstructed the $\Lambda_b \to \Lambda_c \ell \nu$, where $\Lambda_c \to pK\pi$, signal from the inclusive 8 GeV lepton sample. We use this signal to extract the overall $L_{xy}(\Lambda_b)$ resolution scale factor and also as a double check of the Λ_b lifetime in a different sample. The reconstruction cuts are similar to the reconstruction cuts in lepton+SVT sample, but

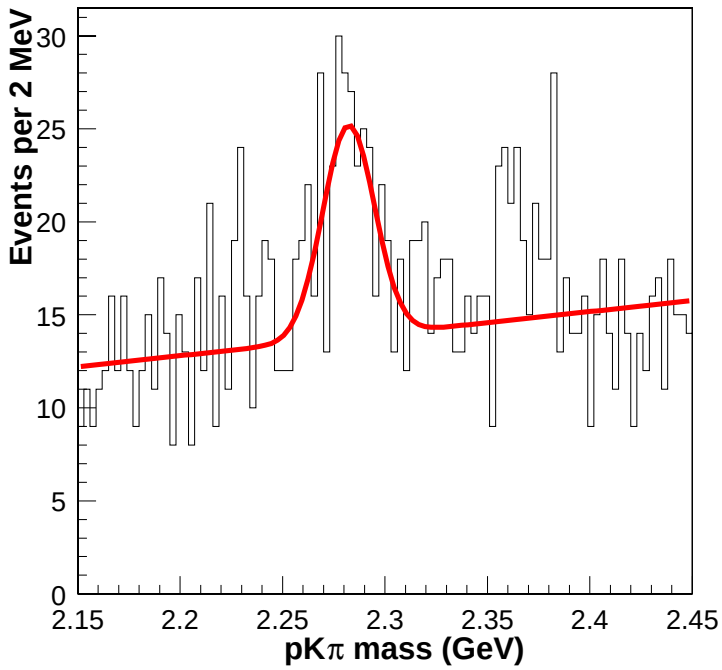

Figure 4.8: $pK\pi$ invariant mass in e+SVT sample where only dE/dx is used to identify the proton, proton likelihood ratio > 0.5.

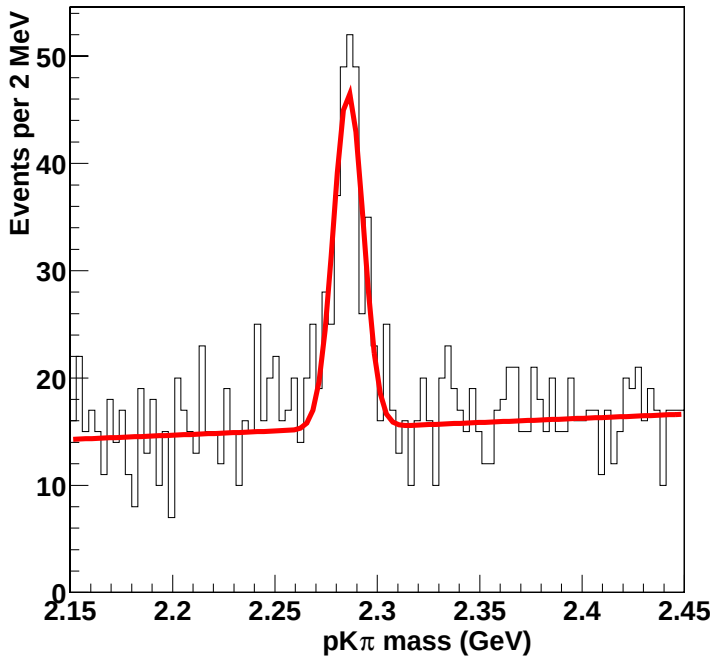

Figure 4.9: $pK\pi$ invariant mass in μ+SVT sample where TOF and dE/dx are both required to identify the proton, proton likelihood ratio > 0.5.

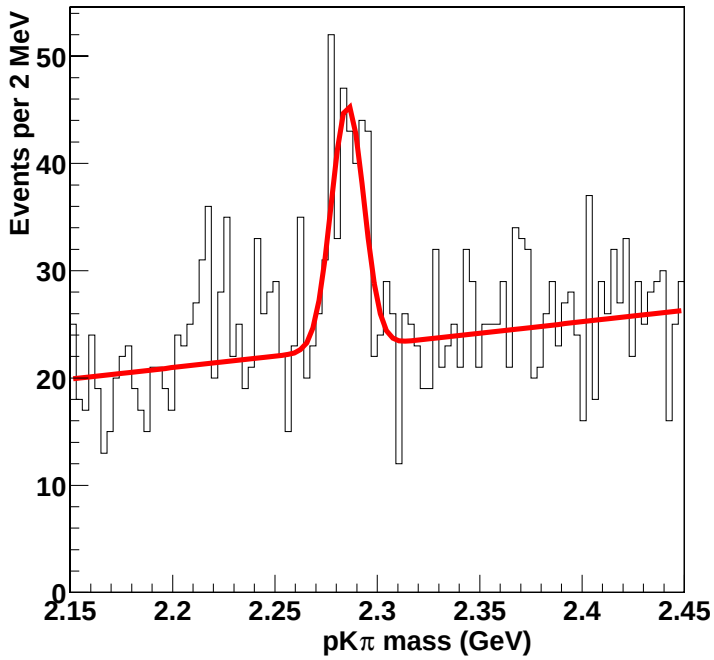

Figure 4.10: $pK\pi$ invariant mass in μ+SVT sample where only dE/dx is used to identify the proton, proton likelihood ratio > 0.5.

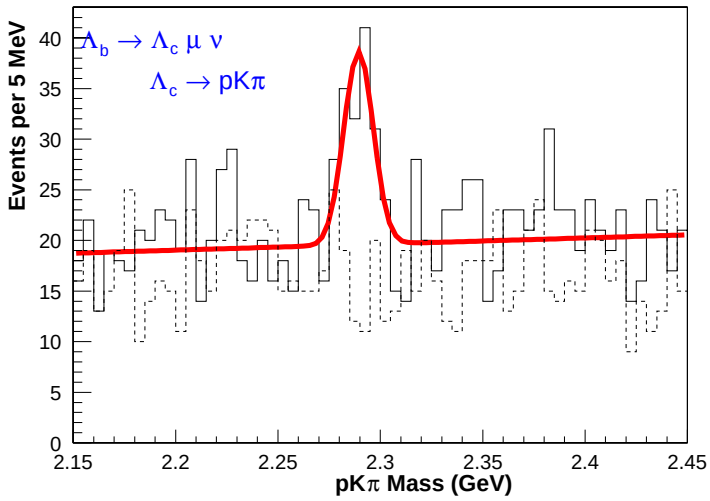

Figure 4.11: $pK\pi$ invariant mass for right sign(solid line) and wrong sign(dashed line) in inclusive 8 GeV muon sample.No signal can be attributed to the wrong sign sample. Proton likelihood ratio > 0.5 cut was applied and proton was required to have both TOF and dE/dx information. Yield returned was 68 ± 15.

we do not require an SVT track for the p,K, π tracks. The Λ_c decay distance is required to have a positive projection along its momentum vector: $L_{xy}(\Lambda_c) > 0.0$. Here decay length $L_{xy}(\Lambda_c)$ is calculated with respect to the primary vertex. And the proton is required to have both TOF and dE/dx information. The reconstructed $pK\pi$ mass from inclusive 8 GeV muon sample is shown in fig 4.11, the yield returned from a similar fit is 68 ± 15.

Bibliography

[1] B Physics at the Tevatron Run II and Beyond, FERMILAB-Pub-01/197

[2] N. Ellis, A. Kernan, Phys. Rep. 195,23 (1990)

[3] Asset Mukherjee, CDF note 5490.

[4] P. Azzi et al, CDF/DOC/TRACKING/CDFR/5562.

[5] K. Bloom and W.-M. Yao, CDF/DOC/TRACKING/CDFR/5991.

[6] Ray Culbertson, http://www-cdf.fnal.gov/internal/upgrades/align/alignment.html; Mary Bishai, et. al., CDF note 5931.

[7] J. Tseng, Observation of Semileptonic Decays of Baryons Containing Bottom Quarks at the Fermilab Tevatron, JHU thesis (1996), chapter 5.

[8] Petar Maksimovic, Observation of pi-B meson Charge-flavor Correlations and Measurement of Time Dependent BB Mixing, MIT thesis, page 227.

[9] Throughout this note charge conjugate modes are implied.

[10] Mike Kirk, et al., CDF/DOC/BOTTOM/CDFR/5324.

[11] H.-C. Fang, A. Cerri, M.D. Shapiro, M. Tanaka, S. Uozumi, CDF/DOC/BOTTOM/CDFR/6326

[12] S. Uozumi, CDF/ANAL/BOTTOM/CDFR/6321 betagamma correction

[13] Alex Cerri, $http://www-cdf.fnal.gov/internal/physics/bottom/control/montecarlo/Full_Simulation.html$

[14] Raymond Culbertson. $http://www-cdf.fnal.gov/internal/upgrades/align/beam.html$

[15] Matthew Herndon, Andreas Korn, Robyn Madrak.

[16] Kevin Burkett, Manfred Paulini, CDF/BOTTOM/ANAL/CDFR/4239.

[17] Gerry Bauer, Mathew Jones, Michael James Mulhearn.
$http://www-cdf.fnal.gov/upgrades/TOF/TOF_welcome.html$

[18] Shin-Shan Yu, Joel Heinrich, Nigel Lockyer, Dave Ambrose, Peter Wittich, CDF/DOC/BOTTOM/PUBLIC/6361.

[19] A.B.Wicklund, private communication on dedx.

[20] J.Tseng, B. Barnett, J.Skarha and T.Miao, CDF/ANAL/BOTTOM/CDFR/3353.

[21] K. Anikeeve., C. Paus, P. Murat, CDF/DOC/BOTTOM/CDFR/5092
P. Sphicas, CDF/ANAL/BOTTOM/CDFR/2655.

[22] S. Uozumi, CDF B meeting, March 6, 2003.

Chapter 5

Measurement of Λ_b Lifetime

5.1 Λ_b Vertex and Decay length

The decay length of the Λ_b in the transverse plane, L_{xy}, is defined as the distance between the Λ_b decay vertex and the production point along $\ell^-\Lambda_c$ momentum direction as shown in Figure 5.1. We assume that the Λ_b is produced at the primary vertex. We then relate the decay length to the Lorentz-invariant proper decay length by a Lorentz boost $\beta\gamma$,

$$c\tau = \frac{L}{\beta\gamma} = L_{xy} \cdot \frac{M}{p_t(\Lambda_b)} \tag{5.1}$$

where L is the three-dimensional decay length, M is the Λ_b mass and $p_t(\Lambda_b)$ is the transverse momentum of Λ_b. Since we do not fully reconstruct the Λ_b due to the undetectable neutrino, we can not calculate the Λ_b momentum directly. With the help of a Monte Carlo simulation and the momentum of the Λ_c-lepton pair, we can estimate the Λ_b momentum. We define a momentum ratio factor K as

$$K \equiv \frac{p_t(\Lambda_c\ell)}{p_t(\Lambda_b)}. \tag{5.2}$$

The distribution of the K factor is obtained from Monte Carlo. Now the proper decay length can be calculated as:

$$c\tau = L_{xy} \cdot \frac{M}{p_t(\Lambda_c\ell)} \cdot K = XK \tag{5.3}$$

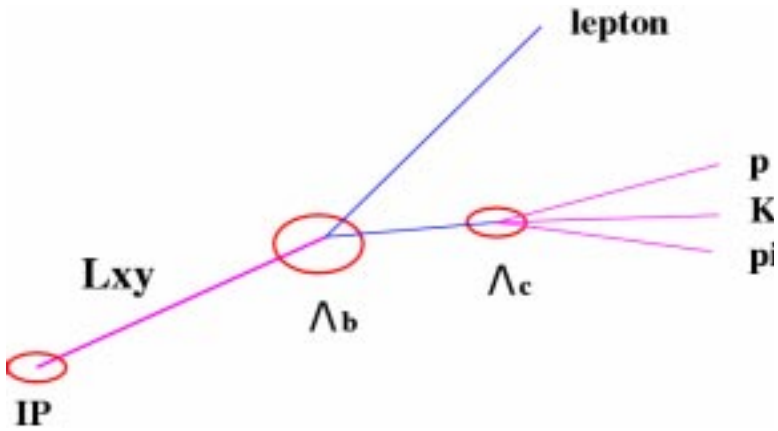

Figure 5.1: Topological sketch of semileptonic decay $\Lambda_b \to \Lambda_c^+ \ell\nu$ where $\Lambda_c \to pK^-\pi^+$.

$$X \equiv L_{xy} \cdot \frac{M}{p_t(\Lambda_c \ell)}. \tag{5.4}$$

where X is the pseudo-proper decay length and will be used as the input variable in the lifetime fitting. For simplicity we will omit the prefix 'pseudo' and call X the proper decay length.

5.2 Lifetime bias from displaced track(SVT)

The SVT track selection criteria in Lepton+SVT sample is $p_t(track) > 2.0GeV/c$, 4 $r\phi$ si-hits on this track and $120\mu m < |d0| < 1mm$, where $d0$ is the track impact parameter corrected for the beam spot as measured by SVT [2]. A correlation between Λ_b $c\tau$ and proton d_0 is shown in Fig 5.2. Since the $c\tau$ distribution is biased by the trigger SVT cut, we must correct for this [4].

A validated generator level Monte Carlo parameterized $c\tau$ acceptance distribution is shown in Figure 5.3. We smear the generated particle d0 with a $57\mu m$ Gaussian resolution function (measured average SVT resolution including beam spot) and accept tracks according to a parameterized SVT $d0$ efficiency function which is fitted from an inclusive J/ψ sample [4]. We use the following formula to fit the accepted Λ_b $c\tau$ distribution obtained by parameterized Monte Carlo:

$$\epsilon_{SVT}(x) = P(x^n) \cdot exp(-x/\lambda_\epsilon) \tag{5.5}$$

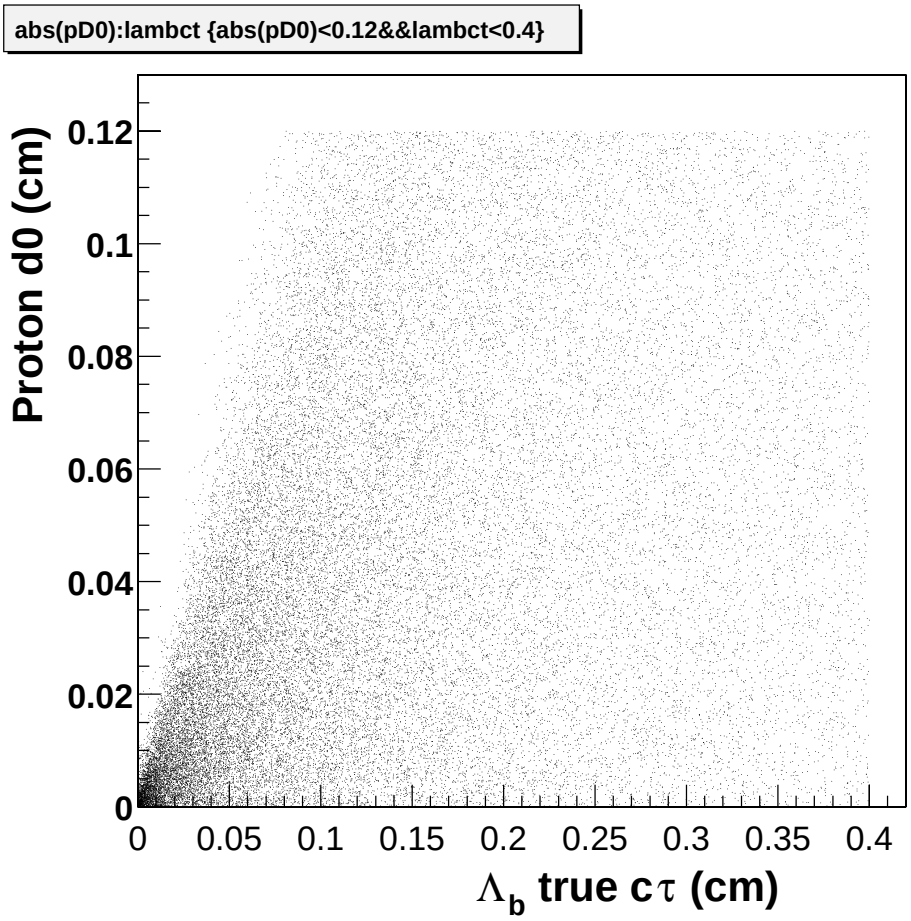

Figure 5.2: Correlation between Λ_b $c\tau$ and proton d_0. $c\tau$ is not uniform along proton d_0, therefore introducing a bias to the lifetime measurement.

where x is the Λ_b proper decay time and $P(x^n)$ is a 4th order polynomial. The effect of the SVT resolution and acceptance on the lifetime distribution is shown in Figure 5.4. Three functions are plotted: $f1(x)$ is the pure exponential $c\tau$ distribution, $f2(x)$ is the $c\tau$ distribution after SVT acceptance, and $f3(x)$ is the $c\tau$ distribution after SVT acceptance convoluted with a Gaussian detector resolution function.

By applying the same kinematic cuts to the $\Lambda_b \to \ell^- \Lambda_c^+ \nu$ Monte Carlo sample, we got the K factor as shown in Fig 5.5

As a comparison, the proton, μ and Λ_c transverse momentum spectra from a full Monte Carlo simulation are compared with the Λ_b signal μ+SVT data, which are shown in Fig 5.6, Fig 5.7, Fig 5.8.

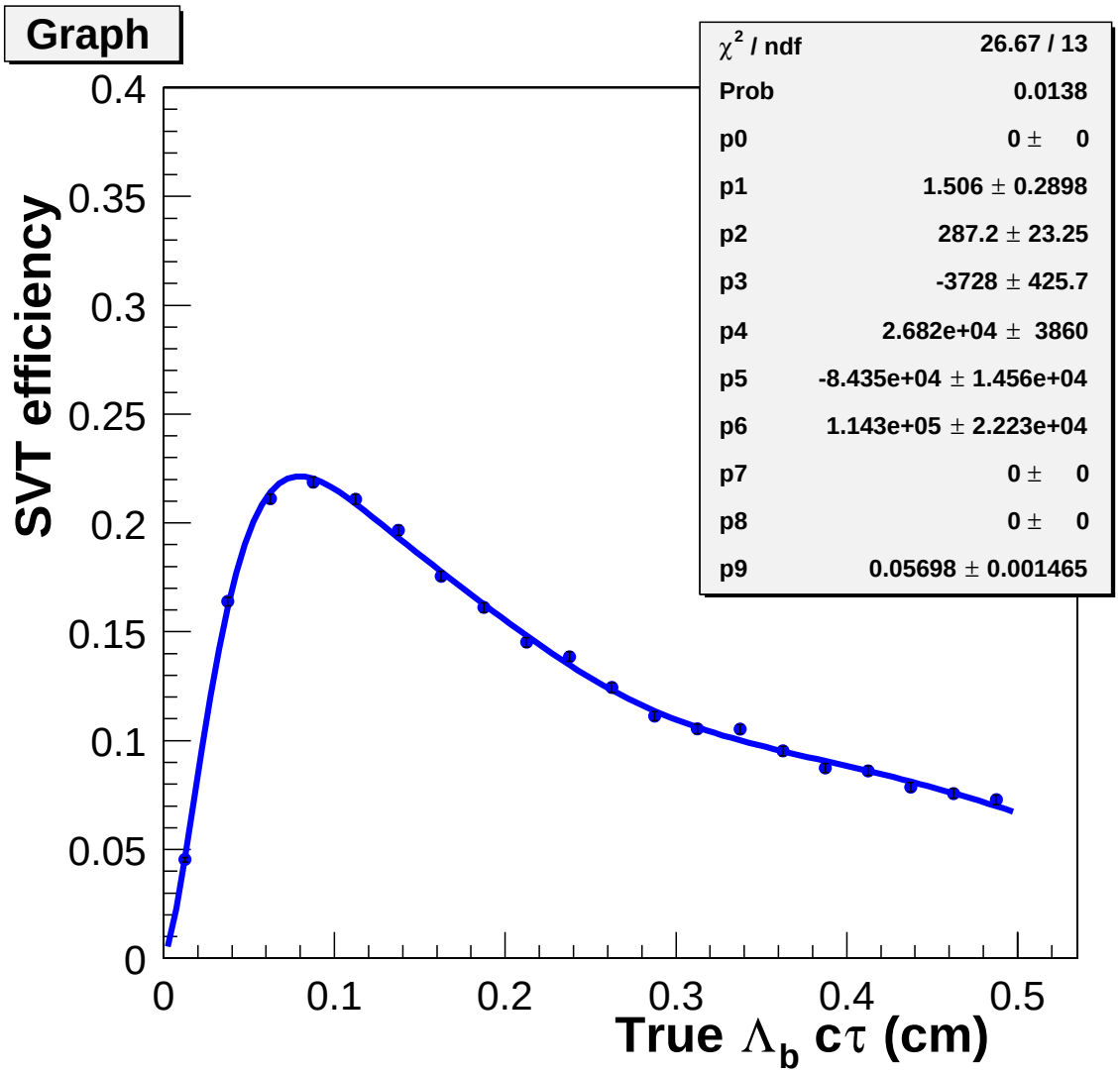

Figure 5.3: SVT efficiency obtained from parameterization method, where the parameters are measured from a inclusive J/ψ sample.

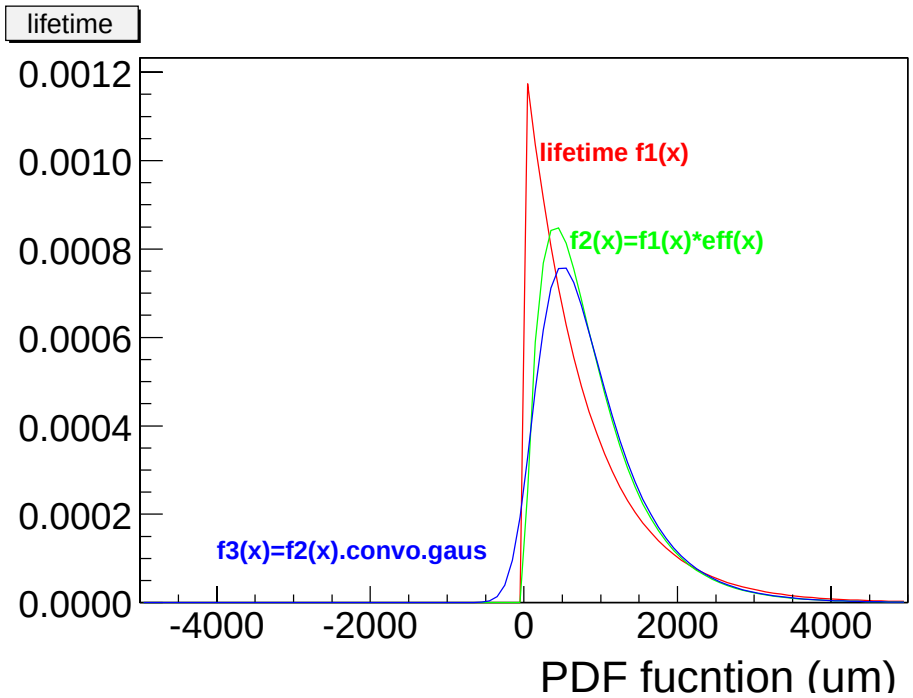

Figure 5.4: Effect of lifetime resolution and SVT acceptance on $c\tau$ measurements. The function $f1(x)$ is the pure exponential $c\tau$ distribution, $f2(x)$ is the $c\tau$ distribution after SVT acceptance, and $f3(x)$ is the $c\tau$ distribution after SVT acceptance convoluted with a Gaussian detector resolution function.

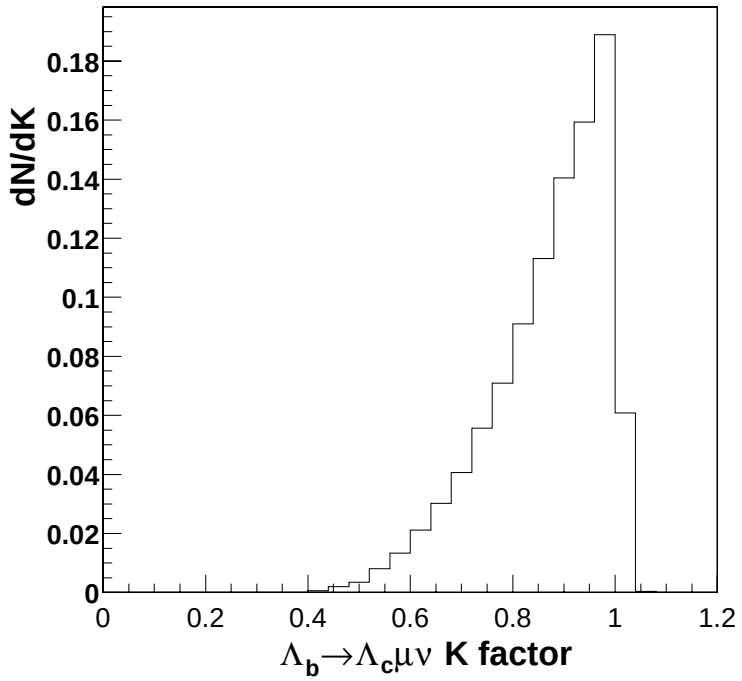

Figure 5.5: Distribution of the K factor in μ+SVT sample, where $K = P_t(\Lambda_c \ell)/P_t(\Lambda_b)$, obtained from parameterization MC.

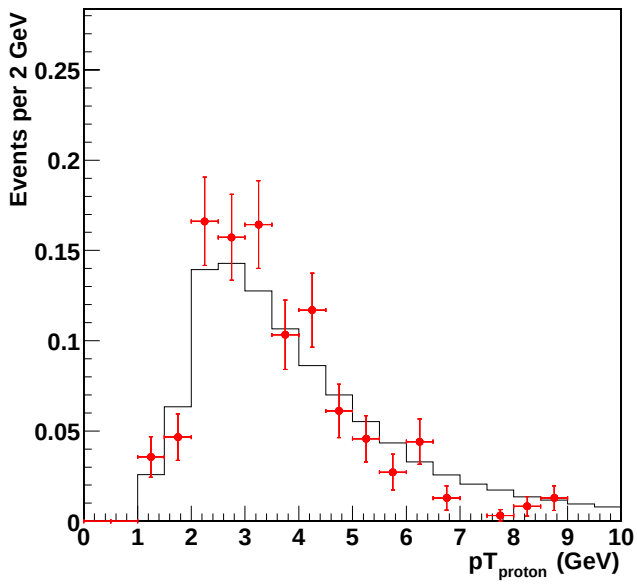

Figure 5.6: Comparison of proton transverse momentum distribution between data and full Monte Carlo for μ+SVT sample. The solid line is obtained from MC and the red (or gray for black and white) circles are obtained from data.

5.3 Lifetime Fitting

An unbinned maximum likelihood fitting method is used to extract the Λ_b lifetime from the data. The proper decay length, X, and its uncertainty, σ, are the input variables. The signal function is assumed to be a pure exponential lifetime distribution times the SVT $c\tau$ acceptance distribution then convoluted with a Gaussian resolution function and with the K factor distribution, $H(K)$, obtained from the full Monte Carlo as follows:

$$F_s = [\epsilon_{SVT}(X')exp(-\frac{KX'}{c\tau_{\Lambda_b}})] \otimes G(X' - X, s\sigma) \otimes H(K) \tag{5.6}$$

Where s is an overall vertex resolution scale factor which represents the possible amount by which we underestimate or overestimate the measurement uncertainty on X, and $\epsilon_{SVT}(X')$ is the normalized $c\tau$ acceptance function obtained from Equation 5.5.

We use the following parametrazation functions to fit the background shape. We

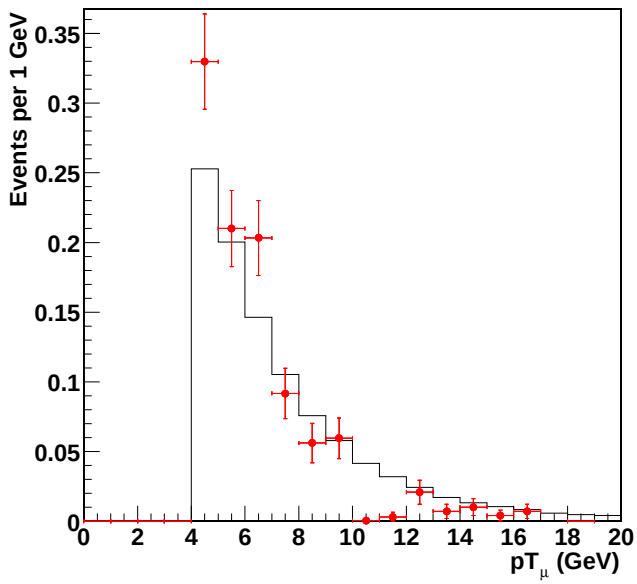

Figure 5.7: The μ transverse momentum comparison between data and full Monte Carlo for μ+SVT sample. The solid line is obtained from MC and the red (or gray for black and white) circles are obtained from data.

model the background function as the following four parts: a Gaussian component which let its center and width float, a positive slope exponential function times SVT $c\tau$ acceptance function, a negative slope exponential function and its reflection on the positive side:

$$\begin{aligned} F_b = \; & (1 - f_+ - 2f_-)G(X - x0, \sigma_{gaus}) + \frac{f_+}{\lambda_+}[\epsilon_{SVT}(X')exp(-\frac{X'}{\lambda_+})] \otimes G(X' - X, s\sigma) \\ & + \frac{f_-}{\lambda_-}exp(\frac{X'}{\lambda_-}) \otimes G(X' - X, s\sigma) + \frac{f_-}{\lambda_-}exp(\frac{-X'}{\lambda_-}) \otimes G(X' - X, s\sigma). \end{aligned}$$

We have f_+, f_-, x_0, σ_{gaus}, λ_+, λ_- floating. Sideband events from the $pK\pi$ invariant mass plots are used as the background sample to obtain the parameters of the background shape, and the sidebands are defined as in the mass window [2.12,2.25] and [2.32,2.46].

The signal region is defined to be 2σ around the Λ_c mass peak. The proper decay

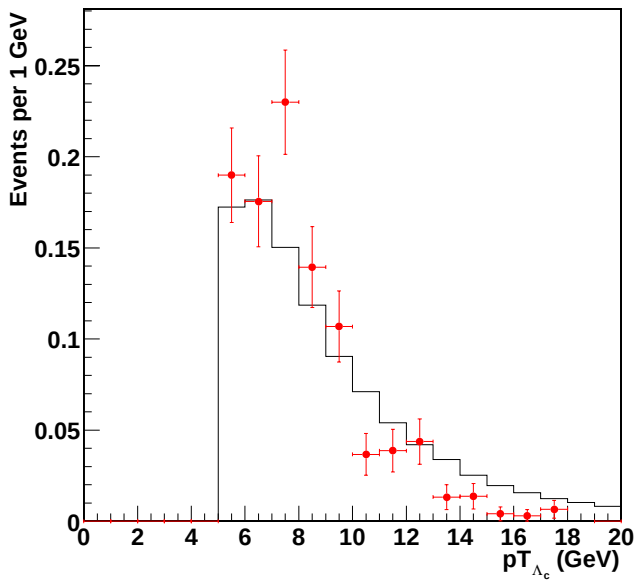

Figure 5.8: μ+Λ_c transverse momentum comparison between data and realistic Monte Carlo for μ+SVT sample. The solid line is obtained from MC and the red (or gray for black and white) circles are obtained from data.

length distribution is described by the following function,

$$F = (1 - f_b)F_s + f_b F_b. \tag{5.7}$$

The background fraction, f_b, is determined by fitting the Λ_c mass distribution. We fit the signal region events and background sample simultaneously using the log-likelihood function,

$$\ln L = \sum_{i=1}^{N_s} \ln F + \sum_{i=1}^{N_b} \ln F_b \tag{5.8}$$

where N_s and N_b are the numbers of events in the signal region and background sample. Since the particle identification power is different between the two cases of a track having both TOF and dE/dx and a track having only dE/dx, we use different f_b's obtained for these two cases and the same functional form of F_b but with different parameters to calculate F_b and F_s, then add the log-likelihoods together. We fix the $L_{xy}(\Lambda_b)$ resolution scale factor to 1.42 which is obtained from the inclusive 8 GeV sample and will be described later. The background fits to the sidebands are shown

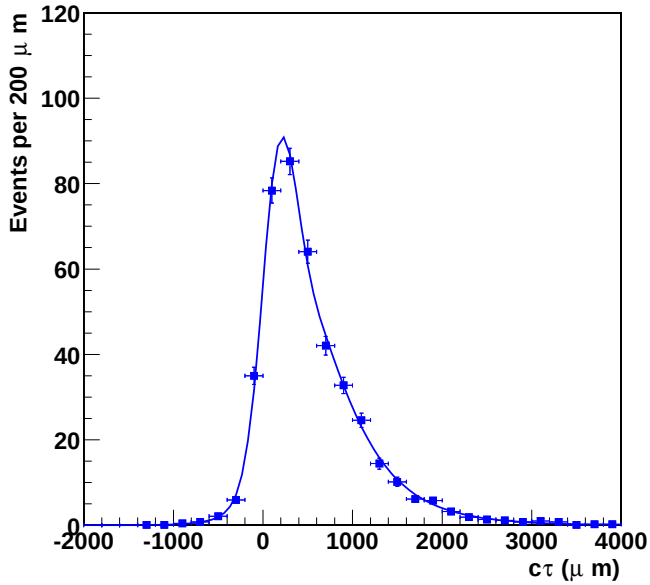

Figure 5.9: Sideband $c\tau$ fitting result in μ+SVT sample. The solid line is the fitting result, the squares with uncertainty bars are data in sideband region.

in Fig 5.9, Fig 5.10, and the fits to 345 $\mu + \Lambda_c$ pair events which passed the selection criteria described above are shown in Fig 5.11 and Fig 5.12. The overlap between signal and sideband are shown in Fig 5.13 and Fig 5.14. The background fit to the case of both TOF and dE/dx are used for proton identification are shown in Fig 5.15, Fig 5.16, and the background fit to the case of only dE/dx are used for proton identification are shown in Fig 5.17, Fig 5.18. The numerical result is listed in Table 5.1. The lifetime of Λ_b is determined to be $c\tau_{\Lambda_b} = 399 \pm 38\ \mu m$.

Because of the SVT track selection in the lepton+SVT sample, we do not have the prompt lifetime which was usually used to extract the $L_{xy}(\Lambda_b)$ resolution scale factor, so we fit to the 68 events which were selected from inclusive 8 GeV lepton sample to extract the $L_{xy}(\Lambda_b)$ resolution scale factor and also as a double check for the Λ_b lifetime.

An unbinned maximum likelihood fitting method is used to extract the Λ_b lifetime from the inclusive 8 GeV muon sample. The proper decay length X and its uncertainty σ are the input variables. The signal function is assumed to be a pure

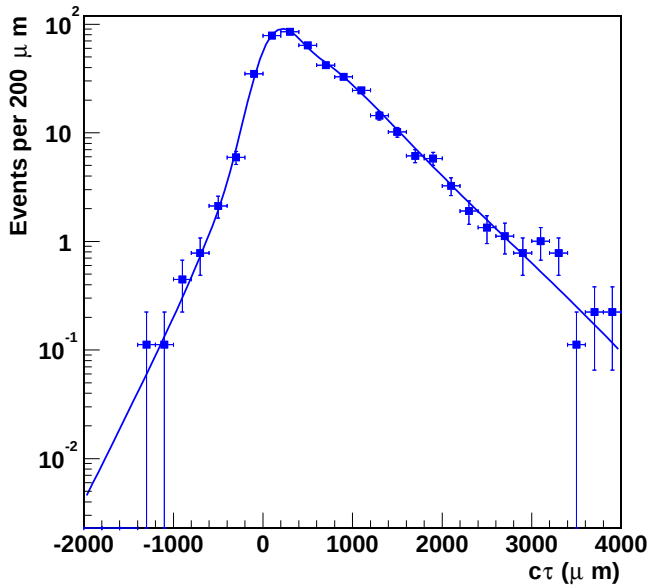

Figure 5.10: Same as Fig 5.9, but on a log scale.

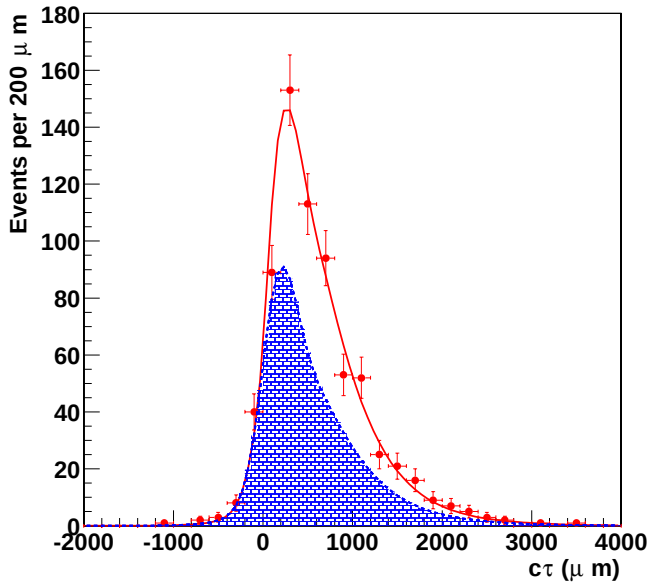

Figure 5.11: Signal region $c\tau$ fitting result in μ+SVT sample. The red (gray in black white) circles with uncertainty bars are data in signal region, the solid line is fit result in the signal region, the dashed line is the background contribution.

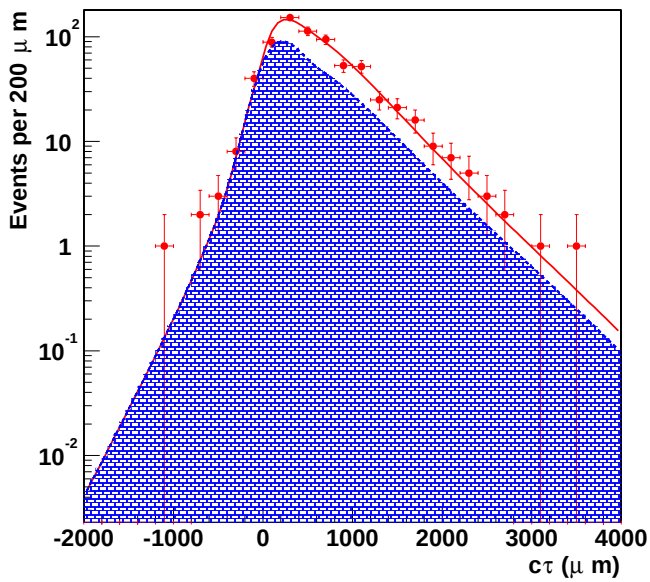

Figure 5.12: Same as Fig 5.11, log scale.

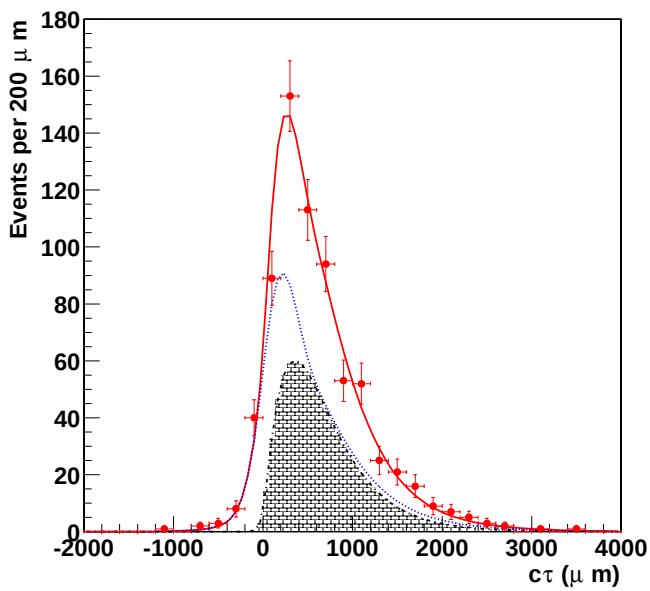

Figure 5.13: The $c\tau$ fit result in the μ+SVT sample. The red (gray in black white) circles with uncertainty bars are data in signal region, the solid line is fit result in the signal region. The blue dot line is the fitting result for sideband data. The black dash dot line is the extracted signal distribution.

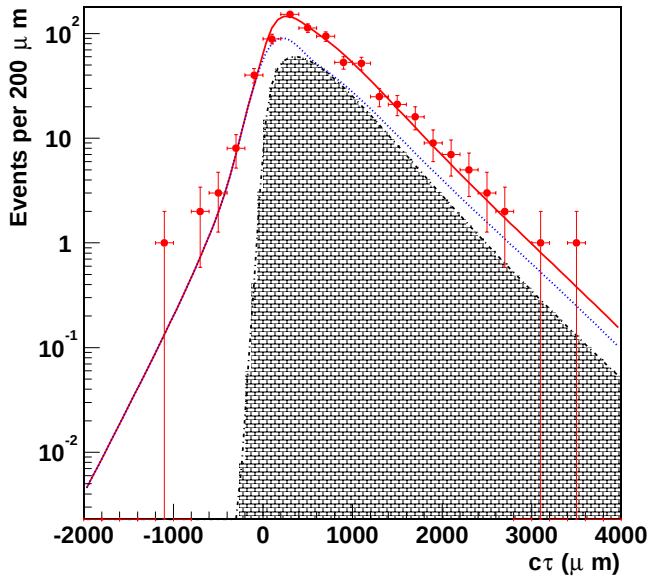

Figure 5.14: The $c\tau$ fit result in the μ+SVT sample, same as Fig 5.13 but on a log scale.

Table 5.1: Results of Λ_b lifetime fit from 345 $\mu + \Lambda_c$ events, where subscript 1 on background parameters represents only dE/dx was used for proton identification, the subscript 2 on background parameters represents both TOF and dE/dx were used for proton identification. The s factor is fixed to 1.42 which we extracted from inclusive μ sample.

$c\tau_{\Lambda_b}(\mu m)$	f_{+1}	$\lambda_{+1}(\mu m)$	$x0_1(\mu m)$
399 ± 38	0.68 ± 0.02	660 ± 28	110 ± 24
s	f_{-1}	$\lambda_{-1}(\mu m)$	$\sigma_{gaus1}(\mu m)$
1.42 ± 0.00	0.04 ± 0.015	263 ± 62	170 ± 14
	f_{+2}	$\lambda_{+2}(\mu m)$	$x0_2(\mu m)$
	0.64 ± 0.03	600 ± 33	281 ± 30
	f_{-2}	$\lambda_{-2}(\mu m)$	$\sigma_{gaus2}(\mu m)$
	0.10 ± 0.01	141 ± 14	145 ± 34

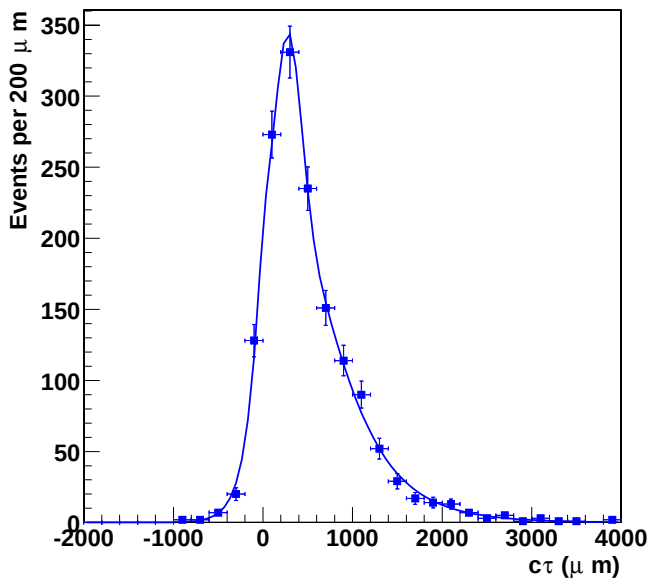

Figure 5.15: The $c\tau$ sideband fit result in μ+SVT sample for the case of TOF and dE/dx both being required to identify proton. The blue squares with uncertainty bars are data in sideband region, the blue dot-dash line is the fitting result for sideband data.

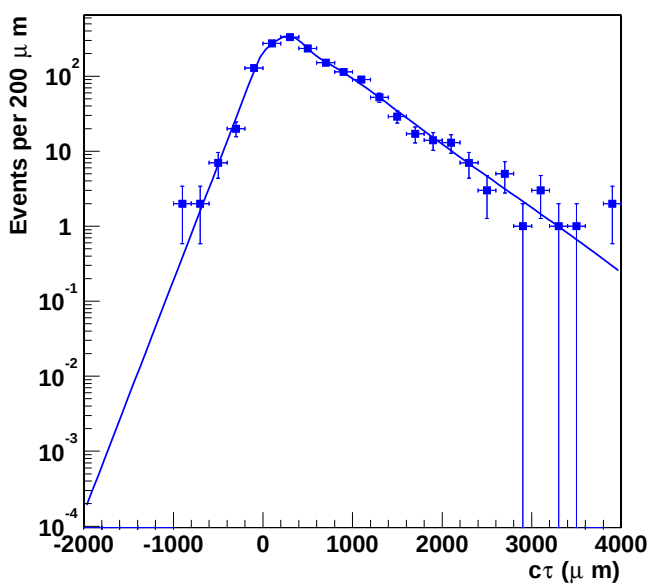

Figure 5.16: Same as Fig 5.15 but on a log scale.

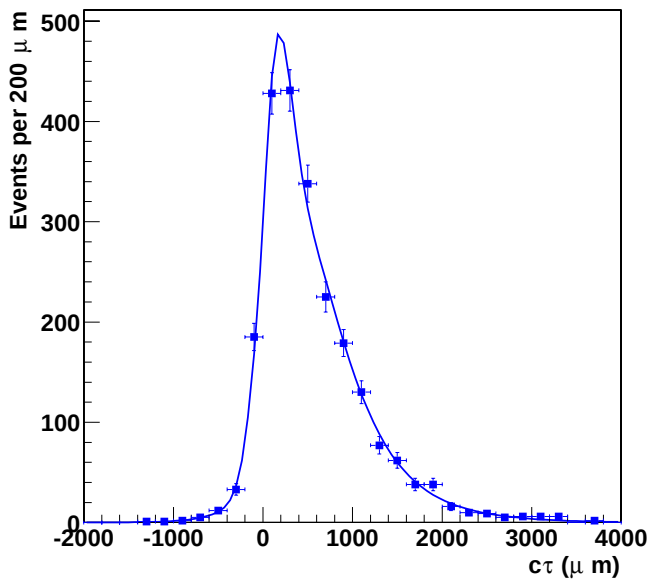

Figure 5.17: The $c\tau$ sideband fit result in the μ+SVT sample for the case of only dE/dx being required to identify proton. The blue squares with uncertainty bars are data in sideband region, the blue (gray in black white) line is the fit result for sideband data.

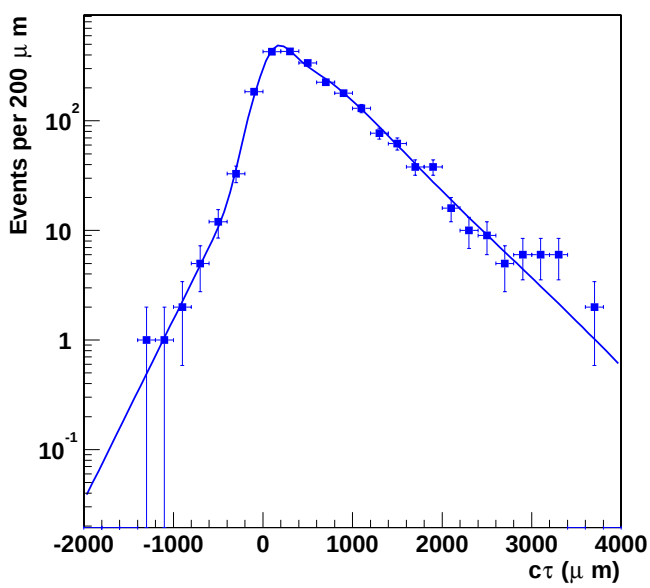

Figure 5.18: Same as Fig 5.17 but on a log scale.

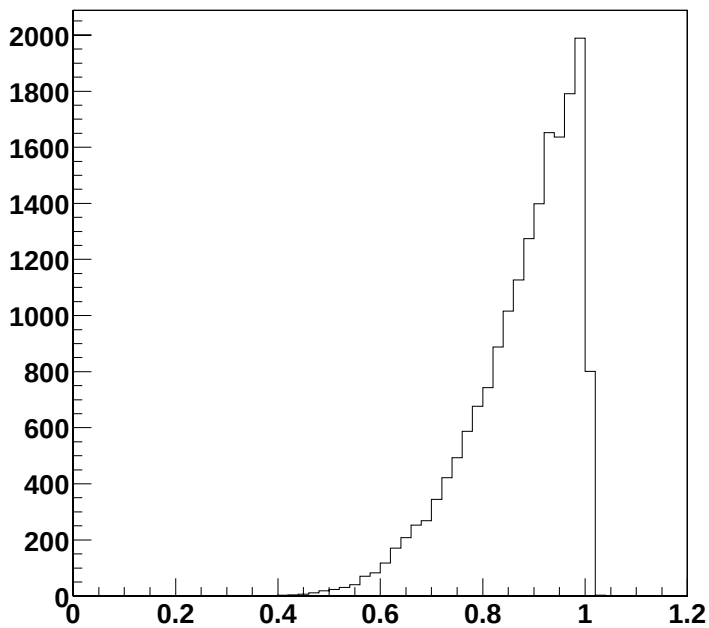

Figure 5.19: The K factor distribution for inclusive 8 GeV lepton sample obtained from validated Monte Carlo, $K = P_t(\Lambda_c \ell)/P_t(\Lambda_b)$.

exponential lifetime distribution, convoluted first with a gaussian resolution function and next with the K factor distribution $H(K)$ obtained from Monte Carlo,

$$F_{s8} = \frac{K}{c\tau_{\Lambda_b}} exp(-\frac{KX'}{c\tau_{\Lambda_b}}) \otimes G(X' - X, s\sigma) \otimes H(K) \tag{5.9}$$

where s is an overall Λ_b L_{xy} scale factor which represents the possible amount we underestimate or overestimate the uncertainty.

Figure 5.19 shows the K distribution obtained using the Monte Carlo [13]. The selection cuts on the inclusive sample described earlier are applied to obtain the distributions.

The background function is composed of four parts representing the zero lifetime component, positive slope exponential function, negative slope exponential function and its reflection on the positive side,

$$F_{b8} = \quad (1 - f_+ - 2f_-)G(X, s\sigma) + \frac{f_+}{\lambda_+} exp(-\frac{X'}{\lambda_+}) \otimes G(X' - X, s\sigma)$$

$$+\frac{f_-}{\lambda_-}exp(\frac{X'}{\lambda_-}) \otimes G(X'-X, s\sigma) + \frac{f_-}{\lambda_-}exp(-\frac{X'}{\lambda_-}) \otimes G(X'-X, s\sigma).$$

Sideband events from the $pK\pi$ invariant mass plots are used as the background sample to obtain the parameters of the background shape.

The signal region is defined to be 2σ around the Λ_c mass peak and the proper decay length distribution is described by the following function,

$$F_8 = (1 - f_{b8})F_{s8} + f_{b8}F_{b8}. \tag{5.10}$$

The background fraction, f_b, is determined from fitting the Λ_c mass distribution. We fit the signal region events and background sample simultaneously using the log-likelihood function,

$$\ln L_8 = \sum_{i=1}^{N_s} \ln F_8 + \sum_{i=1}^{N_b} \ln F_{b8} \tag{5.11}$$

where N_s and N_b are the numbers of events in the signal region and background sample.

The fits to the signal are shown in Fig 5.20 and Fig 5.21, the fits to the sideband are shown in Fig 5.22 and Fig 5.23, and the overlap between signal and background are shown in Figure 5.24, Figure 5.25. The numerical result is listed in Table 5.2 The lifetime of Λ_b is extracted to be $c\tau_{\Lambda_b} = 456 \pm 85\ \mu m$. This agrees with the result of $399 \pm 38 \mu m$ from $\mu + SVT$ sample within error.

Table 5.2: Lifetime fit result in inclusive 8 GeV lepton sample

$c\tau_{\Lambda_b}(\mu m)$	f_+	$\lambda_+(\mu m)$
456 ± 85	0.454 ± 0.020	482 ± 25
s	f_-	$\lambda_-(\mu m)$
1.42 ± 0.09	0.052 ± 0.017	129 ± 26

5.4 Systematic Uncertainties Check

By varying the parameters in the parameterization Monte Carlo, we estimate the lifetime uncertainty from SVT efficiency and a systematic uncertainty of 15 μm is quoted for SVT efficiency [4].

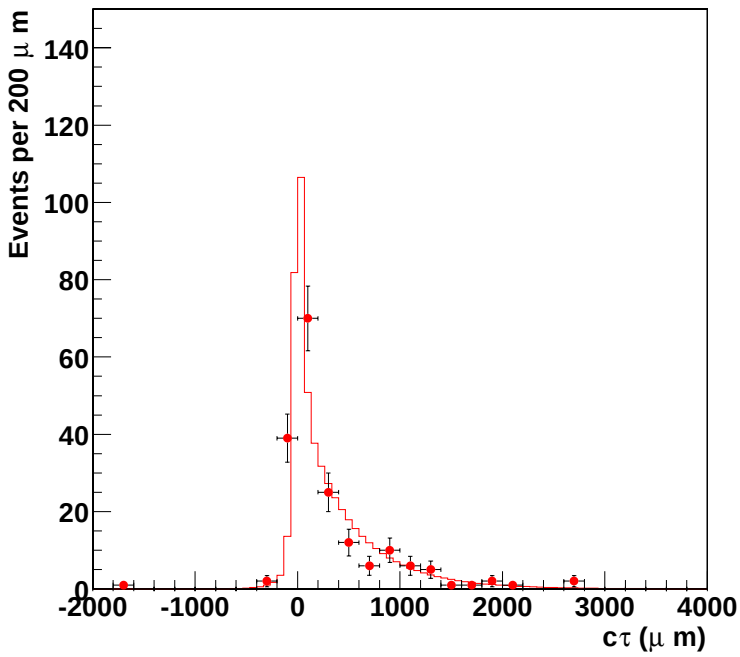

Figure 5.20: Signal region $c\tau$ fitting result in inclusive 8 GeV muon sample, both TOF and dE/dx are required to identify proton. The red (gray for black and white) circles with uncertainty bars are data in signal region, the solid line is fitting result in the signal region.

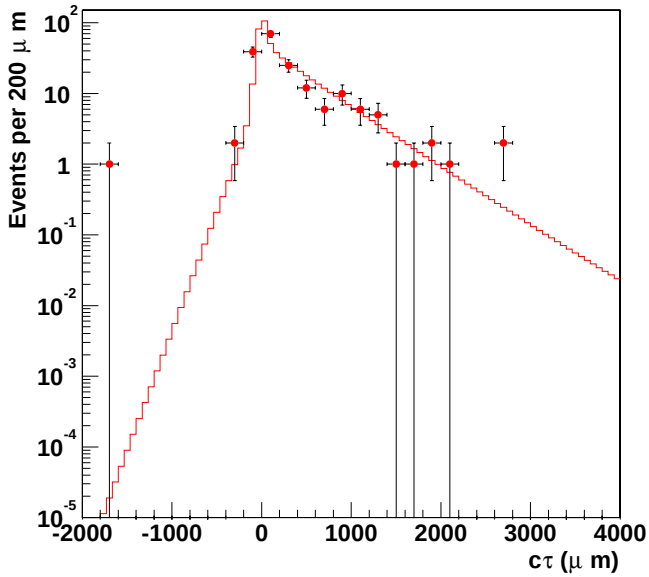

Figure 5.21: Same as Fig 5.20, log scale.

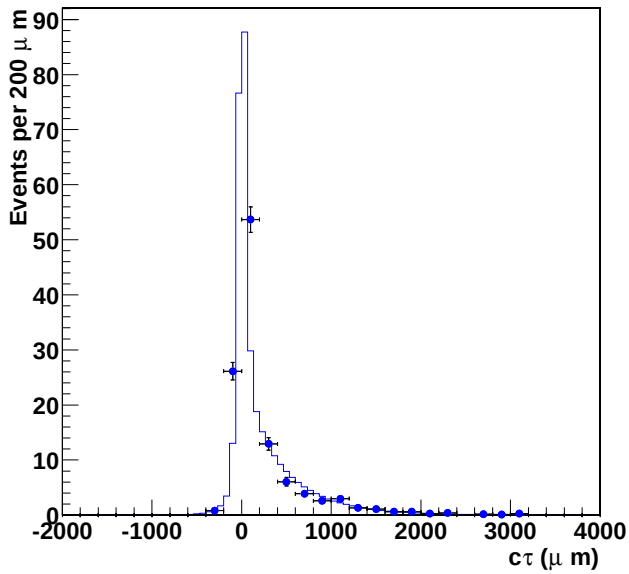

Figure 5.22: Sideband region $c\tau$ fit result in inclusive 8 GeV muon sample, both TOF and dE/dx are required to identify proton. The red (gray for black and white) circles with uncertainty bars are data in signal region, the solid line is fit result in the signal region.

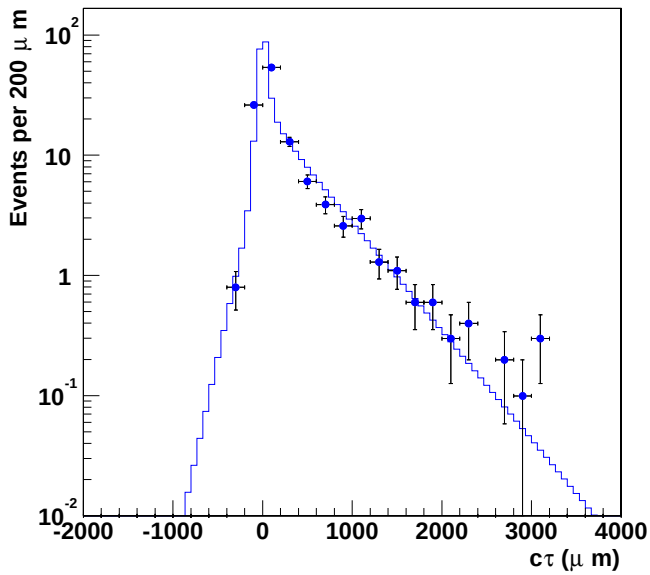

Figure 5.23: Same as Fig 5.22, log scale.

We generate four high statistics full Monte Carlo samples of $\Lambda_b \to \Lambda_c \mu \nu_\mu$ with different lifetimes. We then analyze them the same way as the data except for proton particle identification. The result is shown in Fig 5.26, and the fit for one lifetime is shown in Fig 5.27 and Fig 5.28. The last point has a maximum 9 μm shift, but this point has only half of the other's statistics due to cpu limitations. The other three points have 0,4,4 μm shifts. This indicates some cuts we applied could bias the lifetime, so we quote 9 μm as the systematic uncertainty for selection cuts.

A two step fitting procedure is used to estimate the uncertainty introduced by the fitting procedure. We first determine the background function by fitting only the background sample, then we fit the lifetime using the fixed background shape determined by previous step. The lifetime shift for this fitting is 2 μm. The background function parameters determined from fitting the background sample only is shown in Table 5.3. Comparing with table 5.1, we see the background shape is pretty stable between two step fitting and simultaneous fitting. A 2 μm systematic uncertainty is quoted for the fitting procedure.

From the proton particle identification efficiencies of chapter 3, we see that they are

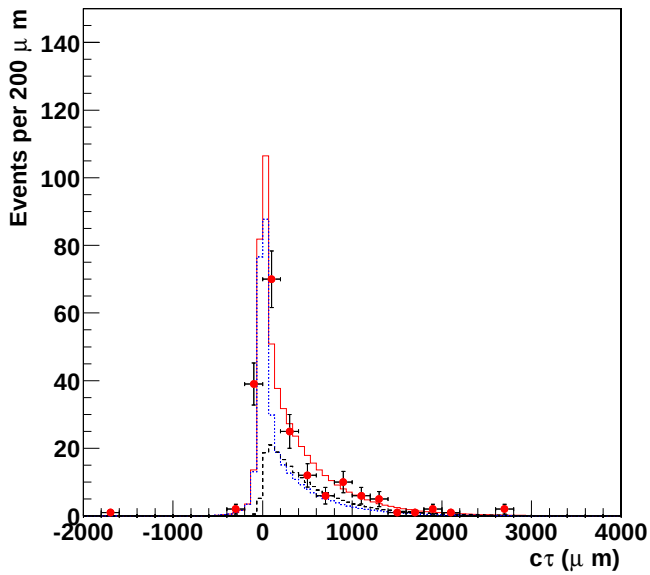

Figure 5.24: $c\tau$ fit result in inclusive 8 GeV muon sample, both TOF and dE/dx are required to identify proton. The red circles with uncertainty bars are data in signal region, the solid line is fit result in the signal region. The blue squares with uncertainty bars are data in sideband region, the blue dot-dash line is the fit result for sideband data. The black dash line is the extracted signal distribution.

Table 5.3: Λ_b background fit results of sideband events, where the subscript 1 on background parameters represents only dE/dx was used for proton identification,the subscript 2 on background parameters represents both TOF and dE/dx were used for proton identification.

$c\tau_{\Lambda_b}(\mu m)$	f_{+1}	$\lambda_{+1}(\mu m)$	$x0_1(\mu m)$
	0.68 ± 0.02	660 ± 28	109 ± 23
s	f_{-1}	$\lambda_{-1}(\mu m)$	$\sigma_{gaus1}(\mu m)$
	0.04 ± 0.015	263 ± 62	170 ± 14
	f_{+2}	$\lambda_{+2}(\mu m)$	$x0_2(\mu m)$
	0.64 ± 0.034	600 ± 33	282 ± 31
	f_{-2}	$\lambda_{-2}(\mu m)$	$\sigma_{gaus2}(\mu m)$
	0.10 ± 0.01	140 ± 13	144 ± 34

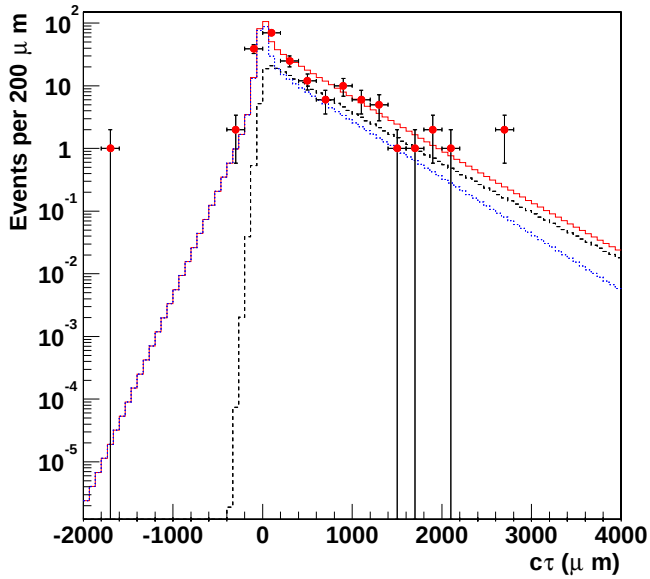

Figure 5.25: $c\tau$ fit result in inclusive 8 GeV muon sample, same as Fig 5.24 but in log scale.

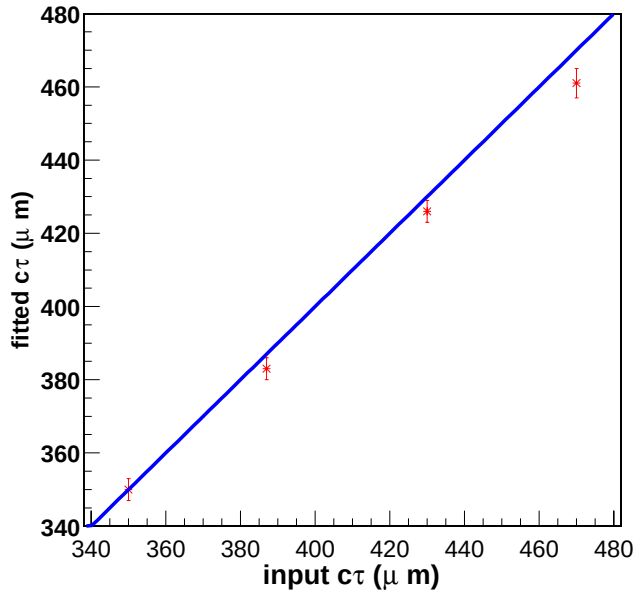

Figure 5.26: Lifetime fit result vs input lifetime from full Monte Carlo check. There is a maxmimum 9 μm shift.

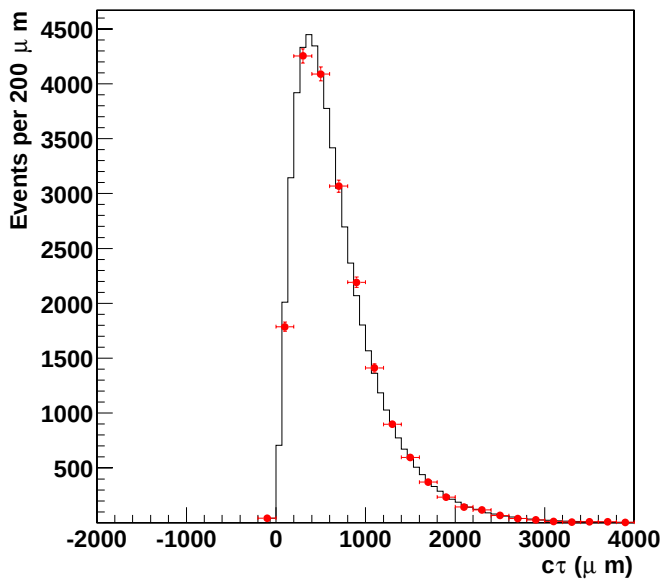

Figure 5.27: A fit to the full Monte Carlo lifetime, input lifetime 430um, fitting result: 426+/-3

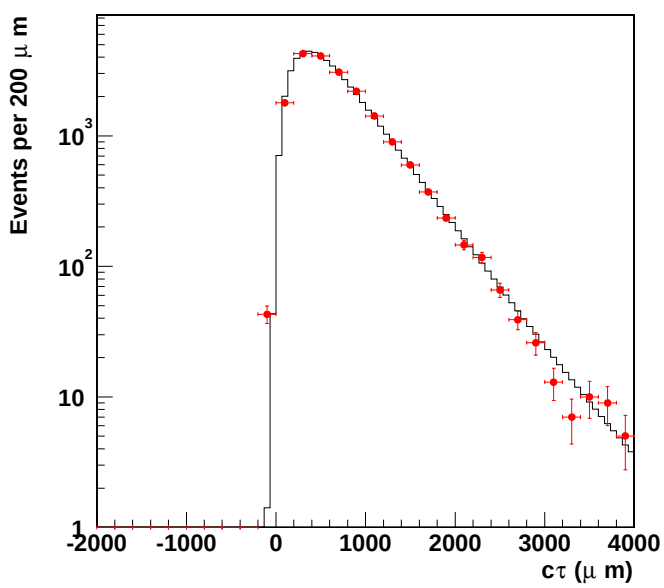

Figure 5.28: A fit to the full Monte Carlo lifetime, log scale

not flat. This can change the proton transverse momentum spectrum and therefore affect the lifetime by changing the K factor. To see the correlation between the proton transverse momentum and the K factor, we show plot $Pt_{\ell+\Lambda_c}$ vs Pt_{proton} in Fig 5.29. It shows that there is no strong correlation between them and we do not expect big effect here. K factors for different proton transverse momentum bins are shown in Fig 5.30. The means are changed from $0.866(1.0GeV/C < P_{Tproton} < 2.0GeV/C)$ to 0.8709 ($7.0\ GeV/C < P_{Tproton} < 9.0\ GeV/C$), and are not much different. We weight the K factor by the proton particle identification efficiency as shown in Fig 5.31, and used the weighted K factor to fit the lifetime and found a lifetime difference of 1 μm. We also weight the events to get the SVT efficiency by proton particle identification efficiency if the proton is a SVT candidate. This is shown in Fig 5.31. The lifetime fitting from this weighted SVT efficiency gives a 2 μm shift. We quote 3 μm as the systematic uncertainty from proton particle identification.

We got the $L_{xy}(\Lambda_b)$ uncertainty scale factor from another sample and used it for the lifetime fitting in the μ+SVT sample, so we vary the $L_{xy}(\Lambda_b)$ uncertainty scale factor by 3 σ. The lifetime change is very small, we quote $2\mu m$ as the $L_{xy}(\Lambda_b)$ uncertainty scale factor systematic uncertainty.

The background fraction is fixed to be the value from the Λ_c mass fit when we fit the lifetime. We change this fraction by one standard deviation and refit the Λ_b lifetime. We find a 3 μm change and quote it as the systematic uncertainty from the background normalization.

Besides the exclusive decay mode of $\Lambda_b \to \Lambda_c \ell \nu$, other semileptonic decays $\Lambda_b \to \Lambda_c \ell \nu X$, such as $\Lambda_b \to \Lambda_c^* \ell \nu$ where $\Lambda_c^* \to \Lambda_c \pi^+ \pi^-$, are possible. The Λ_c momentum from these decays turns out to be softer than for the exclusive decays due to the presence of extra particles, so the high momentum cut on Λ_c suppresses these events. For the same reason, the high invariant mass cut of $\ell + \Lambda_c$ can also suppress these events. We estimate the effect on the K factor by mixing $30\% \Lambda_b \to \Lambda_c^* \ell \nu$ into the Monte Carlo samples and re-fit the lifetime. Fig 5.32 shows the K factor obtained from the mixing. We find a -11 μm lifetime shift. For the $\Lambda_c \to pK\pi$ decay, part of this sample is from resonant states. To estimate this effect, we mix $\Lambda_c \to pK^*$ where $K^* \to K\pi$, at a rate 1 sigma above the measured central value [2] into the

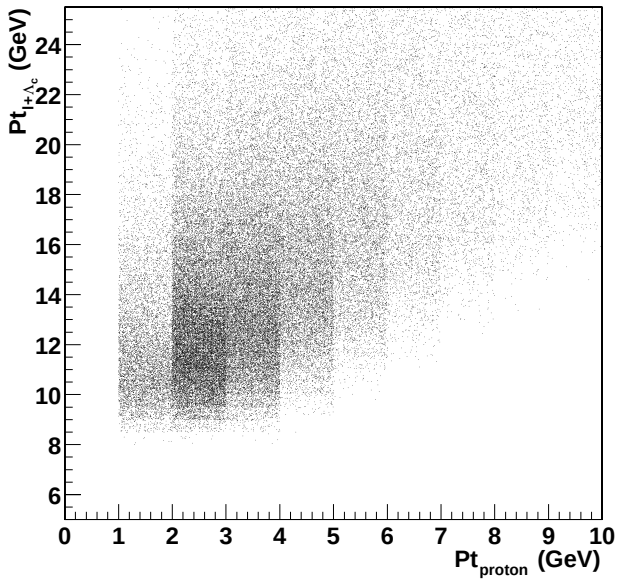

Figure 5.29: A 2d correlation display between proton transverse momentum and $\ell+\Lambda_c$ transverse momentum.

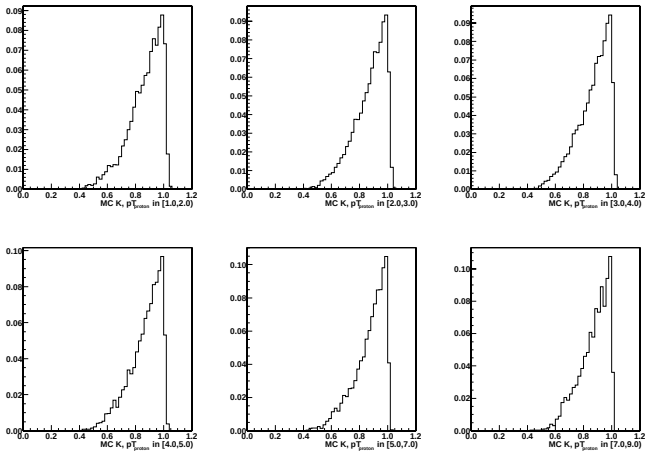

Figure 5.30: The K factor, $K = P_t(\Lambda_c\ell)/P_t(\Lambda_b)$, distributions for different proton momentum regions, the mean value for the six different cases are 0.8666, 0.8681, 0.8662, 0.8668, 0.869, 0.8709 (from left top to right bottom)

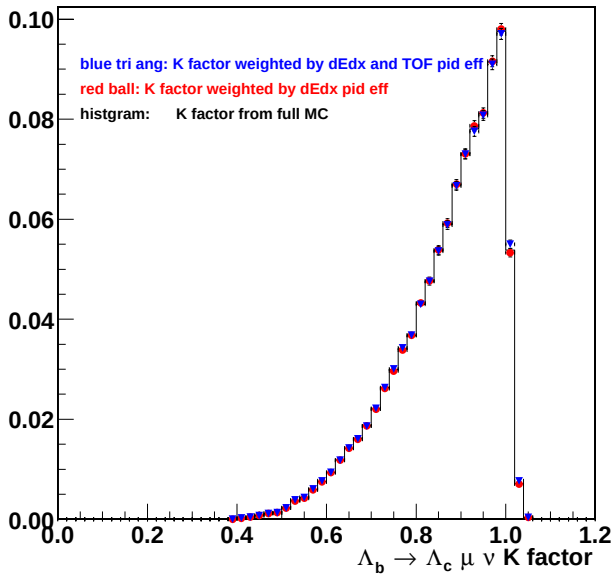

Figure 5.31: Distribution of the K factor in μ+SVT sample, where $K = P_t(\Lambda_c \ell)/P_t(\Lambda_b)$, obtained from full MC sample, where K is weighted by proton identification efficiency. Red (gray in black white) point is weighted by proton identification efficiency which both TOF and dE/dx are used, and blue ball is weighted by proton identification efficiency which only dE/dx is used.

Table 5.4: Summary of systematic uncertainties

Source	$\Delta c\tau_{\Lambda_b}$ (μm)
SVT efficiency bias	15
Event selection cut bias	9
Background normalization	3
Fitting procedure	2
Proton particle identification	3
$L_{xy}(\Lambda_b)$uncertainty scale factor	2
K factor estimation	11
Sum in quadrature	21

Monte Carlo and refit the lifetime. The variation is 1 μm. We quote 11 μm as the systematic uncertainty from the K factor for the above effects.

The summarized systematic uncertainties from different sources are listed in Table 5.4. Adding all the uncertainties in quadrature, the total systematic uncertainty is estimated to be 21 μm.

5.5 Preliminary Results and Discussion

From an unbinned maximum likelihood fit to the proper decay length distribution of 345 ± 34 signal events of $\Lambda_b \to \Lambda_c \ell \nu$, we obtain a preliminary measurement of the Λ_b lifetime of :

$$c\tau_{\Lambda_b} = 399 \pm 38 \pm 21 \mu m$$

$$\tau_{\Lambda_b} = 1.33 \pm 0.13 \pm 0.07 ps$$

The $c\tau$ distribution is corrected for the SVT trigger bias. This result is consistent with the CDF Run I result and LEP result [16] shown in Table 5.5.

Using this result and the average B^0 lifetime, $\tau_{B^0} = 1.54 \pm 0.02\ ps$ [7], we calculate the lifetime ratio $\tau_{\Lambda_b}/\tau_{B^0} = 0.86 \pm 0.08 \pm 0.05$ where the first error is the statistical error from our Λ_b result and the second error is the combination of our systematic error and the error on B^0 lifetime. This is in good agreement with the QCD prediction [17] of $\tau_{\Lambda_b}/\tau_{B^0} = 0.9$. In order to test the HQET theory more accurately, we need to

Table 5.5: Comparison with LEP results obtained using Λ_c-lepton sample and CDF I result.

Source	τ_{Λ_b} (ps)
CDF I	$1.32 \pm 0.15 \pm 0.06$
ALEPH	$1.18^{+0.13}_{-0.12} \pm 0.03$
DELPHI	$1.11^{+0.19}_{-0.18} \pm 0.05$
OPAL	$1.29^{+0.24}_{-0.22} \pm 0.06$
CDF II (this result)	$1.33 \pm 0.13 \pm 0.07$

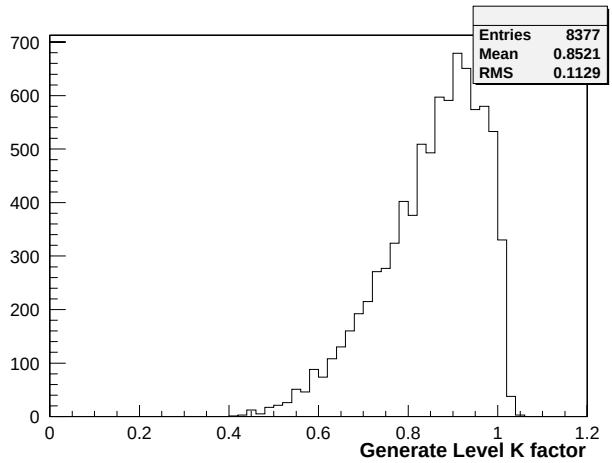

Figure 5.32: K factor for μ+SVT sample obtained in generator level mixing 30 % of Λ_c^*

accumulate more data to reduce the statistical error, and we can combine exclusive channels such as $\Lambda_b \to J/\psi\Lambda$ and $\Lambda_b \to \Lambda_c^+\pi^-$ to reduce the systematic error.

Bibliography

[1] N. Solomey and A.B. Wicklund, CDF 247(1984)

[2] Mike Kirk, Jonathan Lewis, Masashi Tanaka, CDF/DOC/BOTTOM/CDFR/5324

[3] H.-C. Fang, A. Cerri, M.D. Shapiro, M. Tanaka, S. Uozumi, CDF/DOC/BOTTOM/CDFR/6326

[4] S. Uozumi, CDF/ANAL/BOTTOM/CDFR/6321

[5] Alex Cerri, $http://www-cdf.fnal.gov/internal/physics/bottom/control/montecarlo/Full_Simulation.html$

[6] Raymond Culbertson. $http://www-cdf.fnal.gov/internal/upgrades/align/beam.html$

[7] Matthew Herndon, Andreas Korn, Robyn Madrak.

[8] Kevin Burkett, Manfred Paulini, CDF/BOTTOM/ANAL/CDFR/4239.

[9] Gerry Bauer, Mathew Jones, Michael James Mulhearn. $http://www-cdf.fnal.gov/upgrades/TOF/TOF_welcome.html$

[10] Shin-Shan Yu, Joel Heinrich, Nigel Lockyer, Dave Ambrose, Peter Wittich, CDF/DOC/BOTTOM/PUBLIC/6361.

[11] A.B.Wicklund, private communication on dE/dx.

[12] J.Tseng, B. Barnett, J.Skarha and T.Miao, CDF/ANAL/BOTTOM/CDFR/3353.

[13] K. Anikeeve., C. Paus, P. Murat, CDF/DOC/BOTTOM/CDFR/5092 P. Sphicas, CDF/ANAL/BOTTOM/CDFR/2655.

[14] S. Uozumi, CDF B meeting, March 6, 2003.

[15] Particle Data Group, Phys. Rev. **D50** part I, 1 (2002).

[16] D. Buskulic et. al., ALEPH Collaboration, Eur. Phys. J. C2, 197 (1998);
P. Abreu et. al., DELPHI Collaboration, CERN-PPE/99-016;
R. Akers et. al., OPAL Collaboration, Phys. Lett. B426, 161 (1998);
F. Abe et. al., CDF Collaboration, Phys. Rev. Lett. 77, 1439 (1996).

[17] I. I. Bigi, hep-ph/0001003;
I. I. Bigi, hep-ph/9508408.

Chapter 6

Observation of the New State X(3872) at CDF

6.1 Introduction

The discovery of the J/ψ(ground state of bound $c\bar{c}$) meson in 1974 revolutionized our knowledge about the quark theory [1] and the new charm quark(c) was recognized. To date, many excited charmonium states are known, but we are still missing states. The PDG table of the quark model, Figure 6.1, summarizes the low lying states. Recently, the Belle Collaboration announced the observation of a new narrow state in exclusive B decays–$B^+ \to X(3872)K^+$ [3]. They reported that the new state has a mass of 3872.0 $\pm$ 0.6(stat) $\pm$ 0.5(syst) MeV and was observed via its decay to $J/\psi\pi^+\pi^-$. This state is interesting because it may be one of the missing charmonium states, or it may be something totally new. The natural explanation would be one of the missing charmonium states. The first attempt was the $^3D_2$ $J^P = 2^-$ state because the observed X(3872) mass is above the observed $\psi(3770)$ state and this state should have a large branching ratio to decay to $J/\psi\pi^+\pi^-$ because the decay to $D\bar{D}$ ($J^P = 0^-$) is forbidden even though it is above threshold. However, the predicted mass for this state from the potential model was 3815 MeV which is about 60 MeV lower than the observed mass [4]. Furthermore, the favored $^3D_2 \to \gamma\chi_{c2}$ decay which is an E1 radiation was not observed by Belle and they set a limit of

$\Gamma(X(3872) \rightarrow \gamma\chi_{c2})/\Gamma(X(3872) \rightarrow J/\psi\pi^+\pi^-) < 0.89$ at 90% confidence level [5]. Other missing charmonium states have predicted masses which are even further away from the observed $J/\psi\pi^+\pi^-$ mass. For instance, the $^1P_1$ state is predicted to be about 100 MeV above the observed $J/\psi\pi^+\pi^-$ mass. However, in the QCD framework, there are other possibilities [6]. The summed mass of $D^0(1864.5 \pm 0.5$ MeV) and $D^{0*}(2006.7 \pm 0.5$ MeV) is 3871.2±0.7 MeV, and the observed X(3872) is very close to that. This suggests that the X(3872) may be a deuteron-like molecule which is composed of D^0 and $\bar{D}^{0*}$ where a pion is the force mediator. On the other hand, the potential model has a large uncertainty for the predicted mass in this region because it is at the D and $\bar{D}^*$ threshold and the final state interactions, which are not well understood, can shift the mass of the bound state. The X(3872) is very interesting to study whether it is a conventional $c\bar{c}$ state or a new type of matter.

This state was immediately searched for and observed in the existing CDF Run II data sample [7] [8]. Later an independent check was also done and confirmed the observation at CDF [9] [10]. The CDF result is significant because it measures the mass of this new state with comparable errors to Belle, and because it uses inclusive production of this state instead of any exclusive channel so that it may provide additional information about the production mechanism, and the observed large yield at CDF may provide some angular distribution information for this newly observed state. This chapter reports the observation of X(3872) at CDF.

6.2 Event Reconstruction

The dataset used for this work is the $J/\psi \rightarrow \mu\mu$ sample collected between February and August 2003, corresponding to about 220 pb^{-1}. We require all the tracks to have at least 20 axial COT hits and at least 16 stereo COT hit. Tracks are refit to take into account the ionization energy loss appropriate for the particle hypotheses (muon/pion). The silicon hits from intermediate silicon layer, ISL, and the layer 00, L00, are dropped before refitting the track because these subdetectors are not fully aligned. All tracks used for the reconstruction are required to have at least 3 $r\phi$ silicon hits before the refitting.

$N\ ^{2S+1}L_J$	J^{PC}	$u\bar{d}$, $u\bar{u}$, $d\bar{d}$ $I=1$	$u\bar{u}$, $d\bar{d}$, $s\bar{s}$ $I=0$	$c\bar{c}$ $I=0$	$b\bar{b}$ $I=0$	$\bar{s}u$, $\bar{s}d$ $I=1/2$	$c\bar{u}$, $c\bar{d}$ $I=1/2$	$c\bar{s}$ $I=0$	$\bar{b}u$, $\bar{b}d$ $I=1/2$	$\bar{b}s$ $I=0$	$\bar{b}c$ $I=0$
$1\ ^1S_0$	0^{-+}	π	η, η'	$\eta_c(1S)$	$\eta_b(1S)$	K	D	D_s	B	B_s	B_c
$1\ ^3S_1$	1^{--}	ρ	ω, ϕ	$J/\psi(1S)$	$\Upsilon(1S)$	$K^*(892)$	$D^*(2010)$	D_s^*	B^*	B_s^*	
$1\ ^1P_1$	1^{+-}	$b_1(1235)$	$h_1(1170)$, $h_1(1380)$	$h_c(1P)$		$K_{1B}{}^\dagger$	$D_1(2420)$	$D_{s1}(2536)$			
$1\ ^3P_0$	0^{++}	$a_0(1450)^*$	$f_0(1370)^*$, $f_0(1710)^*$	$\chi_{c0}(1P)$	$\chi_{b0}(1P)$	$K_0^*(1430)$					
$1\ ^3P_1$	1^{++}	$a_1(1260)$	$f_1(1285)$, $f_1(1420)$	$\chi_{c1}(1P)$	$\chi_{b1}(1P)$	$K_{1A}{}^\dagger$					
$1\ ^3P_2$	2^{++}	$a_2(1320)$	$f_2(1270)$, $f_2'(1525)$	$\chi_{c2}(1P)$	$\chi_{b2}(1P)$	$K_2^*(1430)$	$D_2^*(2460)$				
$1\ ^1D_2$	2^{-+}	$\pi_2(1670)$	$\eta_2(1645)$, $\eta_2(1870)$			$K_2(1770)$					
$1\ ^3D_1$	1^{--}	$\rho(1700)$	$\omega(1650)$	$\psi(3770)$		$K^*(1680)^\ddagger$					
$1\ ^3D_2$	2^{--}					$K_2(1820)$					
$1\ ^3D_3$	3^{--}	$\rho_3(1690)$	$\omega_3(1670)$, $\phi_3(1850)$			$K_3^*(1780)$					
$1\ ^3F_4$	4^{++}	$a_4(2040)$	$f_4(2050)$, $f_4(2220)$			$K_4^*(2045)$					
$2\ ^1S_0$	0^{-+}	$\pi(1300)$	$\eta(1295)$, $\eta(1440)$	$\eta_c(2S)$		$K(1460)$					
$2\ ^3S_1$	1^{--}	$\rho(1450)$	$\omega(1420)$, $\phi(1680)$	$\psi(2S)$	$\Upsilon(2S)$	$K^*(1410)^\ddagger$					
$2\ ^3P_2$	2^{++}	$a_2(1700)$	$f_2(1950)$, $f_2(2010)$		$\chi_{b2}(2P)$	$K_2^*(1980)$					
$3\ ^1S_0$	0^{-+}	$\pi(1800)$	$\eta(1760)$			$K(1830)$					

Figure 6.1: The PDG table of the quark model.

The J/ψ particle was first reconstructed by requiring two oppositely charged default muons which survived the CTVMFT fitting. To confirm the trigger cuts, a transverse momentum cut of 1.5 GeV/c is applied to the muons. The χ^2 returned from the CTVMFT vertex fit is required to be less than 15. The reconstructed J/ψ mass distribution is shown in Figure 6.2. The J/ψ mass window is set to $|M(\mu\mu) - 3.09687| < 0.06$ GeV. Once a J/ψ candidate is found, then pairs of oppositely charged pions are combined with each J/ψ candidate, and fit again using CTVMFT by assuming they are from the same vertex while the J/ψ mass is constrained to the PDG value. The χ^2 returned from the vertex fit is required to be less than 25. The transverse momentum of a pion candidate is required to be greater than 400 MeV and be inside a $\Delta R = \sqrt{\Delta\phi^2 + \Delta\eta^2}$ cone, where $\Delta\phi$ and $\Delta\eta$ are the azimuthal and pseudorapidity of the pion with respect to the $J/\psi\pi^+\pi^-$ candidate to reduce the combinatorial background. This cone is $\Delta R < 0.7$ for the pion tracks. The transverse momentum of J/ψ is required to be greater than 4 GeV/c to reduce the combinatorial background.

The above cuts are optimized by an iteration procedure in which the significance $rS_\phi/\sqrt{rS_\psi + B_x}$ is maximized as we scan through different values, where S_ψ is the number of $\psi(2s)$ signal, B_x is the number of background candidates in the X(3872) region and r is the ratio of number of $\psi(2s)$ and X(3872) and r is fixed at the beginning of each iteration. We use the scale factor r because a proper optimization depends on the absolute magnitude of the signal, so the $\psi(2s)$ signal should be roughly rescaled to the amount of X(3872) signal. The mass distribution of $J/\psi\pi^+\pi^-$ with the optimized cuts is shown in Figure 6.3.

Since from Belle's announcement, their signal favors high $\pi^+\pi^-$ mass, we also require the mass of $\pi^+\pi^-$ to be greater than 500 MeV/c^2 which still keeps the reference $\psi(2s)$ signal while greatly reducing the background. The mass distribution of $J/\psi\pi^+\pi^-$ with requiring $\pi^+\pi^-$ mass greater than 500 MeV is shown in Figure 6.4. In order to reduce the large combinatorial background due to the large multiplicity of charged tracks in some events, we reject events which have 12 or more candidates with a mass below 4.5 GeV/c^2 [11]. This cut tends to be useful in this hadron collider environment.

As an independent check, a different reconstruction code and different strategy were used to confirm the observation at CDF. The stereo silicon hits attached to track were dropped in that code and it requires better silicon tracks–one of the pion tracks has at least 4 $r\phi$ silicon hits , better vertex constraint–J/ψ vertex χ^2 be less than 10 and $J/\psi\pi^+\pi^-$ vertex χ^2 be less than 15, higher track transverse momentum–$p_T(J/\psi\pi^+\pi^-)$ be greater than 7 GeV and tighter cone size–the ΔR be less than 0.4/0.5 for higher/lower transverse momentum pion track. There is no requirement on the number of candidates for each event. and the mass distribution of $J/\psi\pi^+\pi^-$ for the independent check is shown in Figure 6.5. Later these cuts were loosened relative to the above optimized cuts and the mass distribution of $J/\psi\pi\pi$ is shown in Figure 6.6.

6.3 Mass distribution

The $J/\psi\pi^+\pi^-$ mass distribution of Figure 6.3 is fit to a second order polynomial and two Gaussians. The fit returns 5790$\pm$140 $\psi(2s)$ and 580$\pm$100 X(3872) candidates. After the $\pi\pi$ mass cut, we observed 3530$\pm$100 $\psi(2s)$ and 730$\pm$90 X(3872) candidates (Figure 6.4). The fitted mass and width for $\psi(2s)$ are 3685.65 $\pm$0.09 MeV/c^2, and 3.44 $\pm$ 0.09 MeV/c^2, respectively. The fitted mass for X(3872) is 3871.3 $\pm$0.7 MeV/c^2 and a width of 4.9$\pm$ 0.7 MeV/c^2. This mass is in good agreement with Belle's observation 3872.0 $\pm$ 0.6($stat$) $\pm$ 0.5(sys) MeV/c^2. The CDF X(3872) width is consistent with detector resolution. We use the $J/\psi\pi^+\pi^-$ mass distribution with the $\pi\pi$ mass cut for the mass measurement.

We use the large reference signal $\psi(2s)$ to gauge the systematic uncertainty for X(3872) mass measurement. In the case of the sample with $\pi^+\pi^-$ mass cut, the $\psi(2s)$ mass is measured to be 0.3 MeV/c^2 below the world average mass of 3685.95$\pm$ 0.09 MeV/c^2 [2], a difference significantly larger than the statistical uncertainty of 0.1 MeV/c^2. By varying the selection cuts, it indicates a slightly larger systematic uncertainty of 0.4 MeV/c^2. The fit model and fit range have negligible effect on the mass. A systematic uncertainty of 0.4 MeV/c2 is assigned to the X(3872) mass

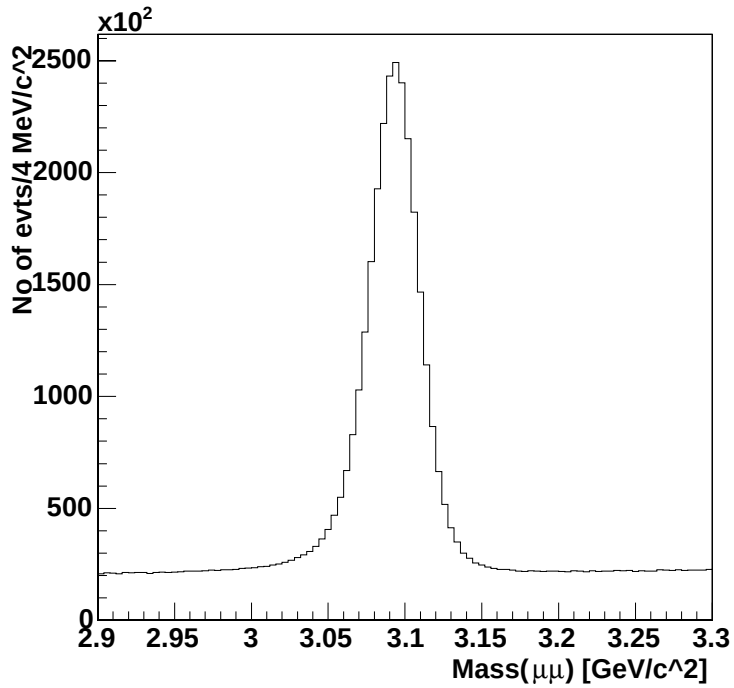

Figure 6.2: Reconstructed $J/\psi \to \mu\mu$ mass distribution.

measurement.

In order to estimate the significance of the signal, we count the number of events in the 3 center bins for X(3872) which is 3893, then by fitting the spectrum, we estimated the background under the 3 bins is 3234, and this gives us a signal of 659 events. By assuming a Gaussian distribution, this corresponds a significance of $659/\sqrt{3234} = 11.6$ standard deviations.

The signal we observed above with the "pseudo-optimization-cuts" did not apply the $\pi\pi$ mass cut (Figure 6.6). It would be interesting to know the $\pi\pi$ mass distribution for $\psi(3872)$ decays, particularly as we have more events than Belle, although it is difficult to do a side band subtraction here because the high mass side band and the low mass side band have different allowed kinematic ranges, which are both different from the $\psi(3872)$ mass window. We scale the $m(\pi\pi)$ in the sideband by the center value of the high/low sideband and the center value of the signal window. The scaling side band subtracted $\pi\pi$ mass for the new $\psi(3872)$ without a $\pi\pi$ mass requirement

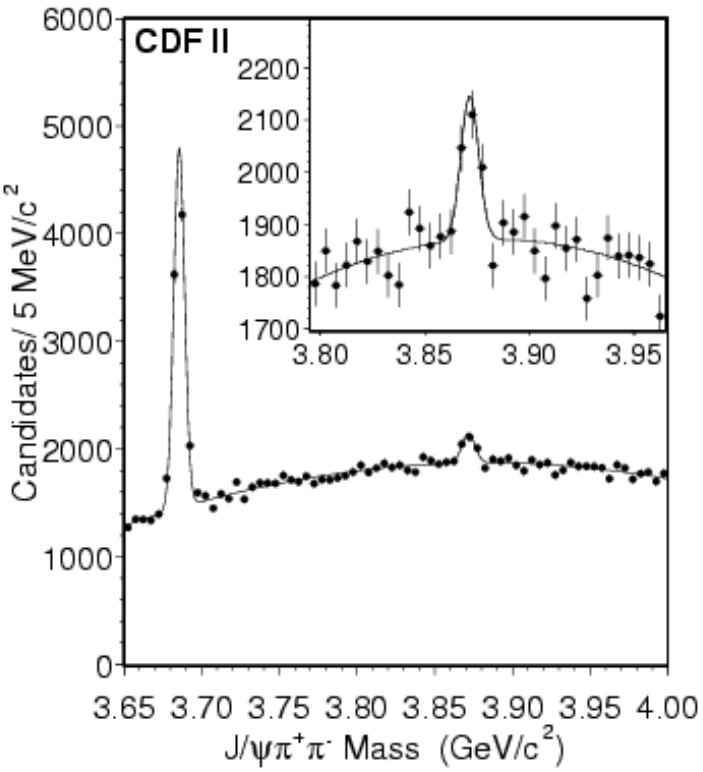

Figure 6.3: $J/\psi\pi\pi$ mass distribution without $\pi\pi$ mass cut.

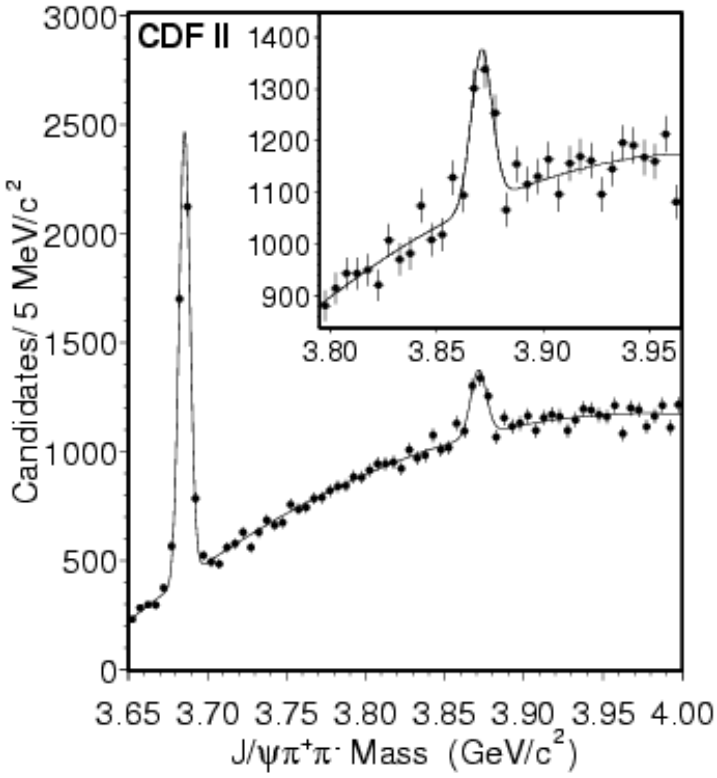

Figure 6.4: $J/\psi\pi\pi$ mass distribution with $\pi\pi$ mass cut.

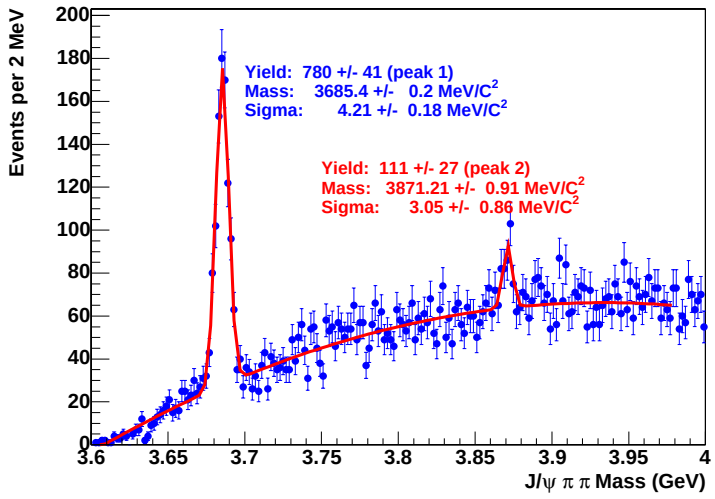

Figure 6.5: $J/\psi\pi\pi$ mass distribution for the tight independent check.

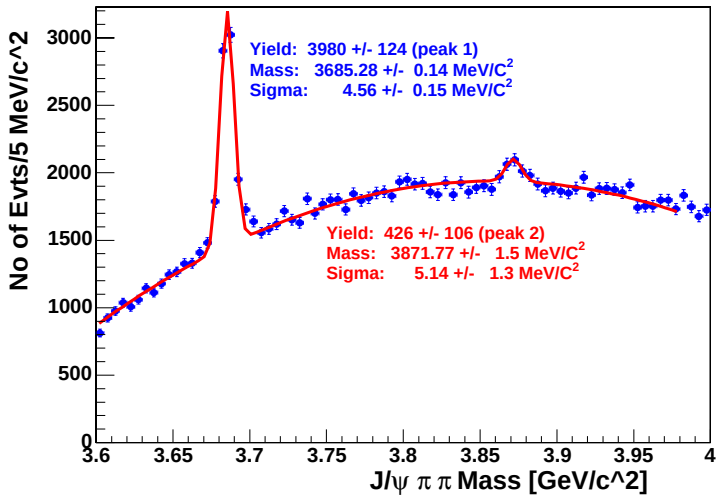

Figure 6.6: $J/\psi\pi\pi$ mass distribution for the loose independent check.

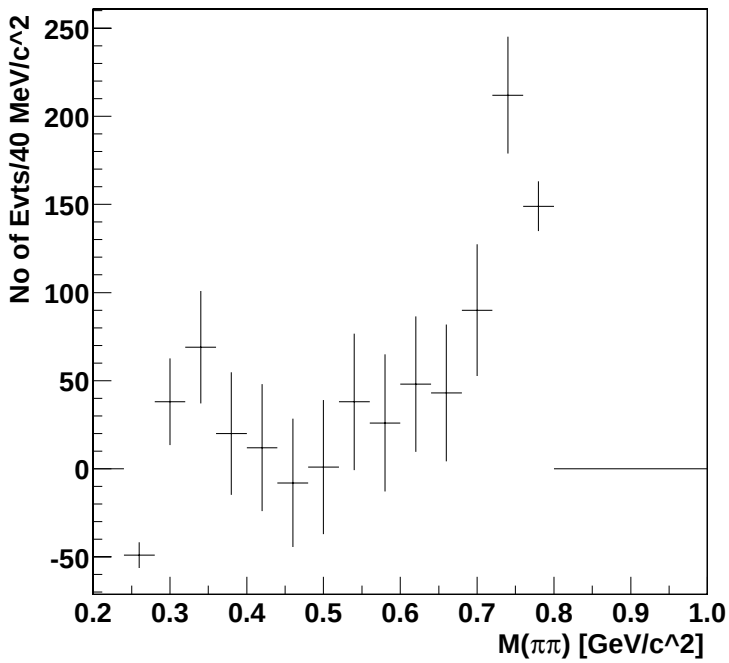

Figure 6.7: The $\pi\pi$ mass distribution from new X(3872) state after preliminary side band subtraction.

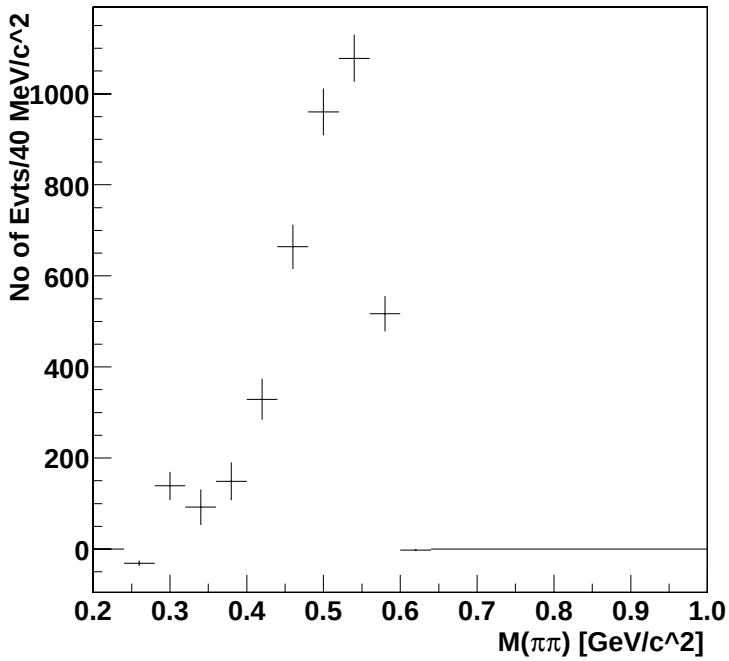

Figure 6.8: The $\pi\pi$ mass distribution from $\psi(2s)$ after preliminary side band subtraction.

is shown in Figure 6.7, and the events are concentrated in the high mass region. For comparison, the scaling side band subtracted $\pi\pi$ mass for $\psi(2s)$ is shown in Figure 6.8. This $\pi\pi$ mass distribution is very interesting because if this is a ρ then the X(3872) can not be a charmonium state because of isospin violation, and would then be suggestive that it may be a molecular structure. However, the $\pi\pi$ mass distribution of $\psi(2s)$ is also peaked in the high mass region, so from the mass distribution itself, it is is hard to draw a conclusion. If we observe a peak at the X position from $J/\psi\pi^0\pi^0$ then it can discard the possibility of ρ decay because ρ can not decay into $\pi^0\pi^0$, then suggesting that X(3872) may be a charmonium state. On the other hand, if we observe a peak from $J/\psi\pi^+\pi^0$, then it indicates that X(3872) is an isospin triplet and it can not be a charmonium state. This will strongly suggest that X may have a molecular structure and open up a whole new area of exploration for hadron spectroscopy. Because of the difficulty in reconstructing π^0, this is difficult to do efficiently in CDF. The B factories(Belle and Babar) may continue the search in the future.

6.4 Conclusion

We have observed an narrow state $X(3872)$ at CDF which confirms Belle's discovery. The mass of the new state is $3871.3 \pm 0.7 \pm 0.4$ MeV/c^2, while the obervered width at CDF is $4.9\pm$ 0.7 MeV/c^2, which is consistent with CDF detector resolution. The preliminary side band subtracted mass distribution shows that the $\pi\pi$ mass distribution for the signal events is concentrated in the high mass region.

Bibliography

[1] J.J. Aubert et al., Phys. Rev. Lett. 33, 1404(1974);
J.E. Augustin et al., Phys. Rev. Lett. 33, 1406(1974).

[2] Particle Data Group, Phys. Rev. **D50** part I, 1 (2002).

[3] S.-K. Choi et al., Observation of a New Narrow Charmonium State in Exclusive $B^{\pm} \to K^{\pm}\pi^{+}\pi^{-}J/\psi$ decays, eprint hep-ex/0309032.

[4] E.Eichten et al., Phys. Rev. D21,203(1980).
E.Eichten, K. Lane, C. Quigg, hep-ph/0206018

[5] Steve Olsen, SLAC experimental seminar, November 11, 2003.

[6] F. E. Close and P. R. Page, hep-ph/0309253.
T. Barnes and S. Godfrey, hep-ph/0311162.

[7] G. Bauer, Ch. Paus, http://www-cdf.fnal.gov/internal/physics/bottom/bmtg_minutes/Aug_21_2003/ bauerpsipipi.ps

[8] G. Bauer, Ch. Paus, K. Sumorok, Observation of the Charmonium State $\psi(3870)$ Decaying to J/psipi+pi- in Run II, CDF Note 6669 (Sept. 2003)

[9] Kai Yi, http://www-cdf.fnal.gov/internal/physics/bottom/bmtg_minutes/Sep_03_2003/ B_mtg_09_04_03.ps

[10] Kai Yi, Barry Blumenfeld, Confirming the Observation of New Charmonium State 3870 at CDF. CDF Note 6679 (Sept. 2003)

[11] CDF collaboration, Observation of the Narrow State $X(3872) \to J/\psi\pi^{+}\pi^{-}$ in $p\bar{p}$ Collisions at $\sqrt{s} = 1.96$ TeV, hep-ex/0312021, submitted to Phys. Rev. Lett.